Numerical investigation of the free energy based lattice Boltzmann method for two-phase flow with large density ratio

Presented by: Jiaming Gong

Supervisor: Prof. Nobuyuki Oshima

JANUARY 2015

Division of Mechanical and Space Engineering

Graduate School of Engineering

Hokkaido University

Contents

Abstract

Two-phase flows, particularly those with large density ratios, occur in numerous important natural and industrial instances, such as petroleum exploitation, underground water recovery, fuel injecting in the internal combustion engine and ink injecting to the surface of paper, water removal from the fuel cell. In order to accurately predict their operation mechanisms and optimize design and operation of such systems, a better understanding of the two-phase flows from numerical simulation is needed, owing to its flexibility compared with experiment analysis.

The complex physics occurring at the interface involves a broad range of time and space scales for the two-phase flow systems. Essentially, the interfacial phenomena arise from the microscopic long-range interactions among the constituent molecules of the phases. The thickness of the interface between the two phases is on the mesoscopic scale. The lattice Boltzmann method (LBM), which based on the mesoscopic kinetic theory, has become a popular tool for appropriately simulating two-phase flows. Because of its kinetic nature, the microscopic intermolecular interactions can be incorporated into the LBM model in a straightforward way. Among the existing LBM models for two-phase flows, the free-energy-based LBM model is becoming increasingly popular, due to its thermodynamic consistency. The early proposed free energy LBM model suffers the Galilean invariance problem for its viscous term and is limited to small density ratios.

Among the recently proposed free energy models for large density ratio, which are free from Galilean-invariance problems, the one proposed by Inamuro is simple and easy to implement; furthermore, it is able to simulate two-phase flows with various density ratios below 1000:1. However, this model has poor computational efficiency, due to the iterative calculation of the approximate pressure Poisson equation. It also contains some heuristic treatments whose effects on the simulation results have not been discussed in the literature.

In this dissertation, the author, starting from the basic LBM model for ideal gas, introduces the fabrication idea of Inamuro's two-phase flow LBM model for large density ratio. And then the author introduces the successive over-relaxation method (SOR)-based formulas and their corresponding staggered grids used to solve the Poisson equation based fractional step method, which were adopted by Tabe et al. (2009) for easier implementation and faster calculation speed. In this process, the thermodynamic meaning of the pressure calculated from the Poisson equation is found to be the hydrodynamic pressure, and the concept of the blending factor is introduced.

Focusing on the shape deformation and volume variation problems of a simulated static droplet in the quiescent gas phase, the author proves that such phenomena occurred in the steady stage originates from the numerical heuristic treatments of the 0- velocity inlet and free-out outlet boundary conditions (which physically corresponds to the pressure-constant boundary). The author proves that such problems can be removed with the adoption of the periodic boundary condition that corresponds to the volume-constant boundary. Numerical analysis shows that the mass exchange at the 0-velocity inlet dominates the mass increasing in the computational domain, compared with the mass exchange at the free-out outlet.

The shape deformation and volume variation mechanisms in the unsteady stage are analyzed with periodic boundary conditions to remove the disturbance from mass exchange with the outside. The spurious velocity from the fractional step method is proven to be the main source of shape deformation; whereas volume variation is proven to come from the diffusion process to form an appropriate interface and the diffusion process to equilibrium the pressure gradient and the interface tension across the interface. Besides, the interaction between the diffusion effect and advection effect is found to be a minor source of shape deformation. With the use of the equilibrium order parameters in the two phases, the droplet volume expansion can be greatly decreased, and the shape deformation caused by the diffusion can also be reduced. Further, with the removal of the advection term from the f_i^{eq} equation, the shape variation tendency with the radii and the blending factor are totally removed; such numerical results prove that for the static equilibrium problem, the LBM model without the advection term may be a better choice.

The numerical error arising from the calculation of the Poisson equation based fractional step method with two types of staggered grids is proven to belong to the category of the anisotropic discretization error, which is one unique origin of the spurious velocity owned by the present model. And the magnitude of the spurious velocity from this type of numerical error can be reduced to half of its original value when the radius length effect is excluded and the velocity components from the two types of staggered grids are equally blended; in this situation, the shape deformation can also be minimized. For the magnitude variations of the spurious velocity with the radius length, a reasonable explanation is given to illustrate how the magnitude of the spurious velocity changes and why large shape deformation with small spurious velocity and small shape deformation with large spurious velocity occurs in the simulation, by combining the initial diffusion process and the spurious velocity component from the calculation of the hydrodynamic pressure. Moreover, the dependences of droplet shape on the blending factor and droplet radius are summarized for the shape optimization.

The spurious velocity, coming from the difference between the density ρ profile and the order parameter ϕ profile which is the main heuristic treatment in the present LBM model, is also investigated. It is found

that the discontinuities of the ρ profile around the cut-off threshold values of the two phases, the difference between the density ρ and the order parameter ϕ profiles in the interface region, and the interface thickness of the ρ can separately induce spurious velocity. The discontinuity of the ρ profile around the cut-off threshold values of the two phases induces the largest magnitude of spurious velocity when the derivatives of the density ρ in the intermolecular force terms directly make use of this profile. And such type of spurious velocity can be reduced by one order in magnitude compared with the original scheme and make the simulation stable, by the adoption of a smooth profile based on the order parameter ϕ profile. The spurious velocity arising from the interface profile difference can be decreased by the adoption of the linear magnification equation instead of the original sine-type of magnification equation. The incompatible discretization error and the anisotropic discretization error are believed to be decreased by the increase of the interface thickness; thus further reducing the magnitude of the spurious velocity.

List of Figures

Nomenclature

c	Characteristic particle speed, m/s
$\boldsymbol{c}_i$	Restricted velocities of particle ensembles, m/s
f_i	Particle velocity distribution functions for the calculation of an order parameter
g_i	Particle velocity distribution functions for the calculation of a predicted velocity
p	Pressure, Pa
t	Time scale, s
F	Intermolecular force, Kg m/s^2
u, u^*	Current velocity and predicted velocity, m/s
Δx	Spacing of the squared lattice, m

Greek letters

μ	Viscosity, Pa·s
ξ	Coordinate perpendicular to the interface, m
ρ	Density, kg/m^3
σ	Interfacial tension, N◎m
ψ	Free energy, J/mol

μ_0 Chemical potential, J/mol

τ_f, τ_g Dimensionless single relaxation time

κ_f, κ_g Constant parameters determining the interface thickness and strength, respectively

ϕ, ϕ_0 Order parameter and reference order parameter

λ Free parameter

Superscript and Subscript

eq Equilibrium state

G Gas

L Liquid

α, β, γ Cartesian coordinates

f Van der Waals fluid with small density ratio

H Hydrodynamic

S Stress form

P Potential form

List of tables

1 Introduction

1.1 Importance of two-phase flow simulation

Two-phase flows, particularly the two-phase flow with large density ratios, occur in numerous important natural and industrial instances, such as petroleum exploitation, underground water recovery, fuel injection in internal combustion engines and ink injection in the printers, water removal from fuel cells. In order to accurately predict their operation mechanisms and optimize design and operation of such systems, a better understanding of two-phase flows from numerical simulation is necessary, owing to its flexibility compared with experimental analysis.

1.2 Typical methods for two-phase flow simulation

The complex physics occurring in the interface involve a broad range of time and space scales for two-phase flow systems. Essentially, the interfacial phenomena arise from the microscopic long-range interactions among the constituent molecules. The thickness of the interface between two phases is on the mesoscopic scale. The interfacial dynamics usually dominate or play an important role in most macroscopic phenomena of two-phase systems, thus determining the performance of whole system. This separation of scales makes it a tough challenge to numerically appropriately model and simulate a relevant two-phase flow.

Numerical methods based on the microscopic physics, like the molecular dynamics, are suitable for capturing the microscopic interactions of the two-phase interface. In fact, there are a lot of applications of the molecular dynamics (MD) to the investigations of two-phase flows. However, because of their expensive nature in computation, they are impractical for simulating the macroscopic two-phase flows of interest to engineers. On the other hand, the macroscopic continuum-method-based two-phase flow simulation techniques, such as the volume of fluid method (VOF), the level-set method (LS), the front tracking (FT) and so on, can simulate the bulk of macroscopic phenomena of the two-phase flow system; however, they have difficulty in capturing the detailed physics that occurring in the interface, and thus are deficient in dealing with dynamic interfacial behaviors.

In recent years, many efforts have been made to establish a mesoscopic numerical method that can consistently connect the microscopic and macroscopic descriptions of two-phase interface phenomena. The lattice Boltzmann method (LBM), which is based on the mesoscopic kinetic theory, has become a popular tool for appropriately simulating two-phase flow phenomena. Because of its kinetic nature, the microscopic intermolecular interactions can be incorporated into the LBM model in a straightforward way.

Typically, when a physically-based intermolecular interaction model is introduced into the LBM model, appropriate two-phase phenomena can be recovered at the macroscopic level.

1.3 LBM models for two-phase simulation

Several different microscopic intermolecular models have been introduced into the basic LBM model, and each of them results in a diffuse interface that separates the two phases. Although the diffuse interface is non-physically large, the diffuse interface methods are easy for implementation, and are able to capture singular interface dynamics such as interface rupture, coalescence and phase separation.

One two-phase LBM model is the color-gradient (C-G) model proposed by Gunstensen et al (1991), which is based on the Rothman-Keller (R-K) lattice gas model. In this model, two distribution functions called the red and blue distribution functions, f_i^r and f_i^b, are used to represent two phases or two components. The intermolecular interactions are modeled by a local color gradient associated with the density difference between the two phases,

$$f_i^r(\mathbf{x}+\mathbf{c}_i\Delta t, t+\Delta t) = f_i^r(\mathbf{x},t) - \frac{1}{\tau^r}\cdot\left(f_i^r(\mathbf{x},t) - f_i^{r(eq)}(\mathbf{x},t)\right) + \left(\mathbf{\Omega}_i^r\right) \qquad 1\text{-}1$$

$$f_i^b(\mathbf{x}+\mathbf{c}_i\Delta t, t+\Delta t) = f_i^b(\mathbf{x},t) - \frac{1}{\tau^r}\cdot\left(f_i^b(\mathbf{x},t) - f_i^{b(eq)}(\mathbf{x},t)\right) + \left(\mathbf{\Omega}_i^b\right) \qquad 1\text{-}2$$

In this model, the local macroscopic variables of each component or phase determine the local equilibrium distribution function. The last part of the collision operator can generate a surface tension in the interface region, but vanishes in the bulk phase regions. Phase separation is realized by a re-coloring step, in which the distribution function is adjusted according to the local color gradient. In the color-gradient model, the mass of each phase and the total momentum are conserved at each node during the collision step. The advantage of this model is that the interface tension and the ratios of the densities and viscosities can be regulated independently (huang et al, 2011). The disadvantage of this model is that the interface tension is dependent on the trend of the interface, which means it is anisotropic. Because of this, there are some artificial flow phenomena around the interface, and large computation resources are required.

The pseudo-potential model (also known as the Shan-Chen (S-C) model) is another popular LBM model adopted for the two-phase simulation. In this model, an artificial nearest-neighbor potential is used to model the intermolecular interactions, which is similar to the idea adopted in the lattice gas automata. The interaction between different phases is mimicked by a long-range interaction force in the collision

operator of the distribution function. The interaction potential for the intermolecular interactions can be written as:

$$V(\mathrm{x},\mathrm{x}') = G(\mathrm{x},\mathrm{x}')\psi(\mathrm{x})\psi(\mathrm{x}') \qquad 1\text{-}3$$

where G represents a Green's function and $\psi(\mathrm{x})$ represents the "effective mass". The interaction force among the constituent molecules can be written as:

$$F = -G(|\boldsymbol{c}_i|)\psi(\mathrm{x})\sum_i \psi(\mathrm{x}+\boldsymbol{c}_i)\boldsymbol{c}_i \qquad 1\text{-}4$$

In the original model, on a hexagonal lattice, the interaction range is extended only to nearest lattice point with the following relation:

$$G(|\boldsymbol{c}_i|) = \begin{cases} G, & \text{if } |\boldsymbol{c}_i| = dx \\ 0, & \text{if } |\boldsymbol{c}_i| > dx \end{cases} \qquad 1\text{-}5$$

where, the dx is the lattice spacing. The advantage of the S-C model is that it is able to track the movement of the phase interface and segregate the two phases automatically, which is an improvement over the color-gradient (C-G) model. Besides, this model works well with high density ratios. There also are some disadvantages for this pseudo-potential model. Although the total momentum in the model is conserved if there is no momentum exchange at the boundaries, the local momentum does not satisfy the conservation law. This leads to some non-physical phenomena around the interface region, such as a large magnitude of the spurious velocity. Neither, the interface tension nor the ratios of densities and viscosities can be adjusted independently. And some parameters have to be decided by numerical test.

The intermolecular interactions in the color-gradient and pseudo-potential LBM models are constructed artificially and heuristically without a firm thermodynamic basis. The phase separations are realized either by a phenomenological rewriting of the collision rules or by the introduction of an effective microscopic interaction. A common drawback shared by the two models is that the two-phase system relaxes to an equilibrium state which cannot be described thermodynamically.

The third type of two-phase flow LBM model is the free-energy-approach-based model. The intermolecular interaction is introduced into the LBM model by adding an equilibrium pressure tensor for a non-ideal fluid to the collision operator (Swift et al., 1995). The resulting phase transition is pressure-driven in a liquid-vapor system with an equilibrium temperature below the critical point; and the two-phase fluid can reach the correct thermodynamic equilibrium as described by the equation of state and a

Maxwell construction. According to the Cahn-Hilliard equation that is derived from the phase field theory, for a van der Waals fluid in the thermodynamic equilibrium at a fixed temperature, the free energy functional can be written as

$$\Psi = \int \left[\psi(\rho) + \frac{\kappa}{2} |\nabla \rho|^2 \right] dV \qquad 1\text{-}6$$

The first term on the right hand side of Eq. (1-6) is the bulk free energy density, the second term describes the contribution from the interface and the κ is a constant relating to the strength of the interface tension. The pressure tensor for the non-ideal gas takes the following form:

$$P_{\alpha\beta} = \left(p_0 - \kappa \rho \nabla^2 \rho - \frac{\kappa}{2} |\nabla \rho|^2 \right) \delta_{\alpha\beta} + \kappa \frac{\partial \rho}{\partial x_\alpha} \frac{\partial \rho}{\partial x_\beta} \qquad 1\text{-}7$$

Where, the p_0 is the thermodynamic pressure.

As mentioned above, the most important advantage of the free energy based LBM model is that it satisfies thermodynamic consistency. Besides, mass and momentum of the system are conserved both locally and globally; and the parameters in the model can be adjusted independently. However, this model suffers from lacking the Galilean invariance for the viscosity terms. Inamuro et al. (2000) added a correction term to the equilibrium distribution function of the free energy model to accommodate the Galilean invariance. Kalarakis et al. (2002) removed the Galilean invariance problem by moving the non-Galilean-invariant part in the viscous stress tensor to the pressure tensor part in the equilibrium distribution function. A similar but different approach proposed by He et al. (1999), wherein the free-energy-theory-based appropriate intermolecular interaction force is incorporated into the discrete Boltzmann equation for non-ideal gas, can also get rid of the Galilean invariance problem.

1.4 Free-energy-based LBM models for large density

The early free-energy-based LBM models (Swift et al., 1995; Inamuro et al., 2000; Kalarakis et al.,2002; He et al., 1999) can only simulate the two-phase flows with small density ratio (usually less than 10), as the simulation becomes more numerical unstable as the density ratio increases. In fact, the two-phase flows existing in the engineering process usually have large density ratios, like the liquid water/gas two phase flow at 20^0C that has density ratio of 847. To simulate the two-phase flows with large density ratio io around 1000:1, modifications to the early free-energy-based LBM model are necessary. At present, mainly, there are three improved models that can deal with two-phase flows with large density ratios while strictly keeping the Galilean invariance and the conservation laws.

The first model was proposed by Inamuro et al. (2004) by using the projection method at the interface region to satisfy the continuity equation after every collision-stream step. In this method, two distribution functions are used: one is for the prediction of the order parameter that distinguishes two phases, the other one is used for the prediction of the predicted velocity of the two phases without a pressure gradient. The order parameter predicting distribution function can only predict the interface dynamics of a two-phase flow with small density ratios. The large density ratio is realized by a cut-off-/-magnification function for the order parameter. This artificial treatment makes the model a kind of heuristic; furthermore, such a treatment may also bring some disturbances to the simulation. The effect of the pressure gradient on the velocity field is supplemented by using the relation between the velocity and the pressure correction which is determined through solving an approximate Poisson equation. Solving the iterative pressure Poisson equation would reduce the efficiency of this model, particularly in the case of simulating two-phase flows in the porous media. Moreover, since the interface tension coefficient in this model cannot be analytically given, an extra trial calculation is needed to fix this parameter; and this would further worsen the computational efficiency. Although poor in computational efficiency, this model is simple and easy to implement, and can simulate two-phase flows with various density ratios below 1000:1. This dissertation will analyze the numerical problems in this model, detailed descriptions about this model and its numerical schemes will be provided in the next chapter.

The second free energy based LBM model for two-phase flow with large density ratio was developed by Lee and Lin (2005) based on the approach proposed by He et al. (1999). In this model, the lattice Boltzmann equation is discretized by a collection of consistent discretization strategies including the low Mach number approximation, the use of stress and potential forms of the surface tension force, the incompressible transformation, and the different discretization schemes of the intermolecular forcing terms. Similar to the Inamuro's model, there are two distribution functions adopted here, one is used for the prediction of the order parameter which is also the density of the one component two-phase system; the other one is used to get the pressure and the velocity of the two-phase flow.

$$f_i(\mathbf{x}+\mathbf{c}_i\Delta t, t+\Delta t) = f_i(\mathbf{x},t) - \left.\frac{f_i - f_i^{eq}}{2\tau}\right|_{\mathbf{x},t} - \left.\frac{f_i - f_i^{eq}}{2\tau}\right|_{\mathbf{x}+\mathbf{c}_i\Delta t, t+\Delta t} + \left.\frac{\Delta t}{2}\frac{(c_{i\alpha}-u_\alpha)A}{c_s^2}\cdot\Gamma_i(\boldsymbol{u})\right|_{\mathbf{x},t} + \left.\frac{\Delta t}{2}\frac{(c_{i\alpha}-u_\alpha)A}{c_s^2}\cdot\Gamma_i(\boldsymbol{u})\right|_{\mathbf{x}+\mathbf{c}_i\Delta t, t+\Delta t} \quad \text{1-8}$$

$$
\begin{aligned}
g_i(\mathbf{x}+\mathbf{c}_i\Delta t, t+\Delta t) = g_i\left(\mathbf{x},t\right) &- \left.\frac{g_i - g_i^{eq}}{2\tau}\right|_{\mathbf{x},t} - \left.\frac{g_i - g_i^{eq}}{2\tau}\right|_{\mathbf{x}+\mathbf{c}_i\Delta t, t+\Delta t} \\
&+ \left.\frac{\Delta t}{2}\frac{\left(c_{i\alpha}-u_\alpha\right)\dfrac{\partial \rho c_s^2}{\partial x_\alpha}}{c_s^2}\cdot\left[\Gamma_i(\boldsymbol{u})-\Gamma_i(0)\right]\right|_{\mathbf{x},t} \\
&+ \left.\frac{\Delta t}{2}\frac{\left(c_{i\alpha}-u_\alpha\right)\dfrac{\partial \rho c_s^2}{\partial x_\alpha}}{c_s^2}\cdot\left[\Gamma_i(\boldsymbol{u})-\Gamma_i(0)\right]\right|_{\mathbf{x}+\mathbf{c}_i\Delta t, t+\Delta t} \\
&+ \left.\frac{\Delta t}{2}\frac{\left(c_{i\alpha}-u_\alpha\right)\dfrac{\partial \rho c_s^2}{\partial x_\alpha}B}{c_s^2}\Gamma_i(\boldsymbol{u})\right|_{\mathbf{x},t} + \left.\frac{\Delta t}{2}\frac{\left(c_{i\alpha}-u_\alpha\right)\dfrac{\partial \rho c_s^2}{\partial x_\alpha}B}{c_s^2}\Gamma_i(\boldsymbol{u})\right|_{\mathbf{x}+\mathbf{c}_i\Delta t, t+\Delta t}
\end{aligned}
\tag{1-9}
$$

where

$$
\Gamma_i\left(\boldsymbol{u}\right) = E_i\left[1+\frac{c_{i\alpha}u_\alpha}{c_s^2}+\frac{\left(c_{i\alpha}c_{i\beta}-c_s^2\delta_{\alpha\beta}\right)u_\alpha u_\beta}{2c_s^4}\right] \tag{1-10}
$$

$$
A = \frac{\partial \rho c_s^2}{\partial x_\alpha} - \rho\frac{\partial\left(\mu_0 - \kappa\dfrac{\partial^2\rho}{\partial x_\beta^2}\right)}{\partial x_\alpha} \tag{1-11}
$$

$$
B = \kappa\frac{\partial\left(\dfrac{\partial\rho}{\partial x_\gamma}\dfrac{\partial\rho}{\partial x_\gamma}\right)}{\partial x_\alpha} - \kappa\frac{\partial\left(\dfrac{\partial\rho}{\partial x_\alpha}\dfrac{\partial\rho}{\partial x_\beta}\right)}{\partial x_\alpha} \tag{1-12}
$$

and the equilibrium distribution functions f_i^{eq} and g_i^{eq} are given in the following equations:

$$
f_i^{eq} = E_i\rho\left[1+\frac{c_{i\alpha}u_\alpha}{c_s^2}+\frac{(c_{i\alpha}c_{i\beta}-c_s^2\delta_{\alpha\beta})u_\alpha u_\beta}{2c_s^4}\right] \tag{1-13}
$$

$$
g_i^{eq} = E_i\left[\frac{p_H}{c_s^2}+\rho\left(\frac{c_{i\alpha}u_\alpha}{c_s^2}+\frac{(c_{i\alpha}c_{i\beta}-c_s^2\delta_{\alpha\beta})u_\alpha u_\beta}{2c_s^4}\right)\right] \tag{1-14}
$$

The above lattice Boltzmann equations are solved in three steps: 1) the pre-streaming collision step, 2) the Streaming step, and 3) the post-streaming collision step. In each step, the distribution equations evolve in the following way:

Pre-streaming collision step:

$$\overline{f}_i(\mathbf{x},t) = f_i(\mathbf{x},t) - \left.\frac{f_i - f_i^{eq}}{2\tau}\right|_{\mathbf{x},t} + \left.\frac{\Delta t}{2}\frac{(c_{i\alpha} - u_\alpha)A}{c_s^2}\cdot\Gamma_i(\boldsymbol{u})\right|_{\mathbf{x},t} \tag{1-15}$$

$$\overline{g}_i(\mathbf{x},t) = g_i(\mathbf{x},t) - \left.\frac{g_i - g_i^{eq}}{2\tau}\right|_{\mathbf{x},t} + \left.\frac{\Delta t}{2}\frac{(c_{i\alpha} - u_\alpha)\partial\rho c_s^2 / \partial x_\alpha}{c_s^2}\cdot\left[\Gamma_i(\boldsymbol{u}) - \Gamma_i(0)\right]\right|_{\mathbf{x},t} \tag{1-16}$$

$$\left. + \frac{\Delta t}{2}\frac{(c_{i\alpha} - u_\alpha)\partial\rho c_s^2 / \partial x_\alpha \; B}{c_s^2}\Gamma_i(\boldsymbol{u})\right|_{\mathbf{x},t}$$

Streaming step:

$$\overline{f}_i(\mathbf{x} + \mathbf{c}_i\Delta t, t + \Delta t) = \overline{f}_i(\mathbf{x},t) \tag{1-17}$$

$$\overline{g}_i(\mathbf{x} + \mathbf{c}_i\Delta t, t + \Delta t) = \overline{g}_i(\mathbf{x},t) \tag{1-18}$$

Post-streaming collision step:

$$f_i(\mathbf{x} + \mathbf{c}_i\Delta t, t + \Delta t) = \overline{f}_i(\mathbf{x} + \mathbf{c}_i\Delta t, t + \Delta t) - \left.\frac{\overline{f}_i - f_i^{eq}}{2\tau + 1}\right|_{\mathbf{x}+\mathbf{c}_i\Delta t, t+\Delta t} + \left.\frac{2\tau}{2\tau+1}\frac{\Delta t}{2}\frac{(c_{i\alpha} - u_\alpha)A}{c_s^2}\cdot\Gamma_i(\boldsymbol{u})\right|_{\mathbf{x}+\mathbf{c}_i\Delta t, t+\Delta t} \tag{1-19}$$

$$g_i(\mathbf{x}+\mathbf{c}_i\Delta t,t+\Delta t)=\bar{g}_i(\mathbf{x}+\mathbf{c}_i\Delta t,t+\Delta t)$$
$$-\left.\frac{\bar{g}_i-g_i^{eq}}{2\tau+1}\right|_{\mathbf{x}+\mathbf{c}_i\Delta t,t+\Delta t}+\frac{2\tau}{2\tau+1}\frac{\Delta t}{2}\left.\frac{(c_{i\alpha}-u_\alpha)\frac{\partial\rho c_s^2}{\partial x_\alpha}}{c_s^2}\cdot\left[\Gamma_i(\boldsymbol{u})-\Gamma_i(0)\right]\right|_{\mathbf{x}+\mathbf{c}_i\Delta t,t+\Delta t} \quad 1\text{-}20$$
$$+\frac{2\tau}{2\tau+1}\frac{\Delta t}{2}\left.\frac{(c_{i\alpha}-u_\alpha)\frac{\partial\rho c_s^2}{\partial x_\alpha}B}{c_s^2}\Gamma_i(\boldsymbol{u})\right|_{\mathbf{x}+\mathbf{c}_i\Delta t,t+\Delta t}$$

The density, the velocity, and the hydrodynamic pressure are calculated after the streaming step by the following equations:

$$\rho=\sum_i\bar{f}_i \quad 1\text{-}21$$

$$\rho u_\alpha=\sum_i c_i\bar{g}_i+\frac{\Delta t}{2}\kappa\left[\frac{\partial}{\partial x_\alpha}\left(\frac{\partial\rho}{\partial x_\gamma}\frac{\partial\rho}{\partial x_\gamma}\right)-\frac{\partial}{\partial x_\beta}\left(\frac{\partial\rho}{\partial x_\alpha}\frac{\partial\rho}{\partial x_\beta}\right)\right] \quad 1\text{-}22$$

$$p_H=\sum_i\bar{g}_i+\frac{\Delta t}{2}u_\alpha\frac{\partial\rho c_s^2}{\partial x_\alpha} \quad 1\text{-}23$$

In a plane interface at equilibrium, the density profile across the interface at equilibrium can be obtained as:

$$\rho(\xi)=\frac{\rho_L^{sat}+\rho_G^{sat}}{2}+\frac{\rho_L^{sat}-\rho_G^{sat}}{2}\tanh\left(\frac{2\xi}{D}\right) \quad 1\text{-}24$$

where D is the thickness of interface and it can be derived by:

$$D=\frac{4}{\rho_L^{sat}-\rho_G^{sat}}\sqrt{\frac{\kappa}{2\beta}} \quad 1\text{-}25$$

and β is a constant, named compressibility factor which is related to the free energy density with,

$$\Psi(\rho)\approx\beta\left(\rho-\rho_G^{sat}\right)^2\left(\rho-\rho_L^{sat}\right)^2 \quad 1\text{-}26$$

The interface tension is:

$$\sigma = \frac{\left(\rho_L^{sat} - \rho_G^{sat}\right)^3}{6}\sqrt{2\kappa\beta} \tag{1-27}$$

This model maintains thermodynamic consistency and it is able to simulate two-phase flows with density ratios of up to 1000:1; also, the interface tension coefficient and the thickness of the interface can be analytically obtained. However, as shown above, the algorithm in this model is too complicated; moreover, the discretization schemes for the intermolecular force terms vary in different sub-steps, which further worsens its efficiency in application.

The third free energy based two-phase flow LBM model that can deal with large density ratio is the one proposed by Zheng et al. (2006). In this model, the interface capturing equation (also called Cahn-Hilliard equation) is recovered more accurately as compared with the models introduced above. Also the required discrete velocity directions in this model are smaller than those in the other two models; and the interface tension coefficient and the thickness of the interface can be analytically acquired. There are two distribution functions and two order parameters used in this model:

$$f_i(\mathbf{x}+\mathbf{c}_i\Delta t, t+\Delta t) = f_i\left(\mathbf{x},t\right)+\Omega_i^f \tag{1-28}$$

$$g_i(\mathbf{x}+\mathbf{c}_i\Delta t, t+\Delta t) = g_i\left(\mathbf{x},t\right)-(1-q)\cdot\left(g_i(\mathbf{x}+\mathbf{c}_i\Delta t,t)-g_i\left(\mathbf{x},t\right)\right)+\Omega_i^g \tag{1-29}$$

Where

$$\begin{aligned}\Omega_i^f &= \frac{f_i^{eq}(\boldsymbol{x},t)-f_i(\boldsymbol{x},t)}{\tau_n} \\ &+\left(1-\frac{1}{2\tau}\right)\frac{E_i}{c_s^2}\left[\left(c_{i\alpha}-u_\alpha\right)+\frac{c_{i\alpha}u_\alpha}{c_s^2}c_{i\alpha}\right]\left(\mu_0\nabla\phi+F_b\right)\Delta t\end{aligned} \tag{1-30}$$

$$\Omega_i^g = \frac{g_i^{eq}(\boldsymbol{x},t)-g_i(\boldsymbol{x},t)}{\tau_\phi} \tag{1-31}$$

$$n = \frac{\rho_L+\rho_G}{2}, \qquad \phi = \frac{\rho_L-\rho_G}{2} \tag{1-32}$$

where, ϕ is used to distinguish two phases, n is used to track the total density in the continuity equation and the momentum conservation equation. The equilibrium distribution functions f_i^{eq} and g_i^{eq} are defined as:

$$f_i^{eq} = E_i D_i + E_i n\left(3c_{i\alpha}u_\alpha - \frac{3}{2}u^2 + \frac{9}{2}u_\alpha u_\beta c_{i\alpha}c_{i\beta} \right) \quad 1\text{-}33$$

$$g_i^{eq} = A_i + B_i\phi + C_i\phi c_{i\alpha}u_\alpha \quad 1\text{-}34$$

For f_i and g_i, the 2DQ9 and 2DQ5 discrete velocity models are used, respectively; and A_i, B_i, C_i and D_i are the corresponding coefficients. The free energy functional adopted in this model is different from the other two models in which the van der Waals free energy functional are used, the bulk free energy density adopted in this model is:

$$\psi(\phi) = A\left(\phi - \phi^*\right)^2 \quad 1\text{-}35$$

The interface tension coefficient and the thickness of the interface can be given in a similar way, as given in the Lee and Lin's model. The total density *n*, the velocity $\boldsymbol{u}$, the order parameter ϕ, and the pressure can be calculated by the following equations:

$$n = \sum_i f_i^{eq} \quad 1\text{-}36$$

$$\boldsymbol{u} = \left(\sum_i f_i^{eq} c_i + \frac{1}{2}\left(\mu_0 \nabla\phi + F_b \right) \right) / n \quad 1\text{-}37$$

$$\phi = \sum_i g_i \quad 1\text{-}38$$

$$p = A(3\phi^4 - 2\phi^{*2}\phi^2 - \phi^{*4}) - \kappa\phi\nabla^2\phi + \frac{(\nabla\phi)^2}{2} + \frac{n}{3} \quad 1\text{-}39$$

Obviously, this model also satisfies the thermodynamic consistency, and compared to the other two models, it is the simplest. However, as pointed out by Fakhari and Rahimian (2010), this model seems only suitable for a density-matched binary fluid, thus limiting its applications in the simulation of two-phase flows with random density ratios.

1.5 Motivations and objectives

The free-energy-approach based two-phase flow LBM for large density ratio developed by Inamuro et al. (2004) is easy to implement and also is capable of simulating two-phase flows with an arbitrary density ratio less than 1000:1, though it contains some heuristic treatments and is poor in computational efficiency. It is still a good choice to use this model to simulate the two-phase flow phenomena with a large density ratio. Several researches have been implemented with the help of the Inamuro's model. Yan

and Zu (2006) successfully simulated the dynamics of liquid droplets on uniform and heterogeneous wetting walls; Moriyama and Inamuro (2011), and Tabe et al (2009, 2012) quantitatively simulated the two-phase flow of liquid water and gas in the polymer electrolyte fuel cell (PEFC). Li and Morozumi (2012) investigated the evaporation behavior and solute deposition of a sessile droplet on homogenous and patterned substrates. All these investigations prove that this model is applicable to simulations of two-phase flows with density ratios around 1000:1, but no one has ever considered its reliability.

As mentioned above, the major drawback of Inamuro's model is its low efficiency, which mainly arises from the iterative calculation of the approximate pressure Poisson equation. In order to improve the efficiency and facilitate implementation, Tabe et al. (2006, 2007, 2009, and 2012) used the successive over-relaxation iteration method (SOR) with the staggered grids instead of the original LBM scheme with the co-location grid to solve Poisson equation. However, they did not yet have a clear idea of the proportions of the two types of staggered grids blended in the solving process of the Poisson equation.

Moreover, the heuristic magnification and cut-off equation adopted in this model, which is similar to the level set (L-S) method, may have some effect on the simulation results, such as the effects of the variation of the cut-off threshold value, and the choice of a magnification equation. Information from the literature about the effects of this heuristic treatment is still lacking. Beyond this, since the interface tension coefficient cannot be analytically determined, the effect of initial conditions on the inlet/outlet boundaries has not been discussed before.

On the one hand, droplet is an important form of two-phase flows; researches related to the droplet dynamics have attracted much attention, due to its theoretical and technical importance. Hirayama (2009) investigated the liquid fuel droplet dynamics during the spraying process. Ben Salah et al. (2012), Han et al. (2012 a, b), Hao and Cheng (2009 a), and Zhu et al. (2008) researched the liquid water droplet removal mechanism in the gas channel of the PEFC. Van der Graaf et al. (2006, 2008) studied the droplet formation mechanism in a T-shaped micro-channel. Varnik et al. (2007, 2009 and 2011) investigated the stability and dynamics of droplets on wetting and roughness patterned substrates. On the other hand, it is easy to obtain the theoretical solutions of a stationary water droplet for comparison with the simulated results. For the purposes of studying the reliability of the free energy based two-phase flow LBM for large density ratio, based on the schemes, formulations, boundary conditions and parameters adopted by Tabe et al (2009), a 2D static water droplet in a gas channel was simulated.

In the simulation, some non-physical numerical phenomena occurred, which decreased the reliability of this model. It was found that the shape of the droplet was deformed to different degrees while different blending factors of the two types of staggered grids adopted in the calculation of the approximate pressure

Poisson equation or with different radii. Fig. 1 shows the predicted density distribution of a water droplet with the same radius but different blending factors. Figs. 2, 3, and 4 show the predicted density distribution of a water droplet with the same blending factors but different radii. Also, the spurious velocity field around the droplet interface had strange distributions, particularly when the radius of the droplet was large. Usually, large shape deformation means large force imbalance in the interface region, thus large spurious velocity. However, as shown in Fig. 5, when the water droplet radius was 20, the blending factor α=0.0 case had a smaller degree of deformation compared with the case α=1.0; the spurious velocity around the interface in the case of α=0.0 was 3 times as large as in the case of α=1.0. Besides, the mass conservation broke even when the simulation arrived at the steady stage, when the 0-velcoity inlet and free-out outlet boundary conditions were used in the simulation. Fig. 6 shows the volumes of the droplet at different time steps when the radius was 12 *dx* and the blending factor α is 1.0; Fig. 7 shows the mass evolution histories of the droplet with the radius of 12 *dx* and typical blending factors. Actually, in cases simulated with the boundary conditions and parameters adopted by Tabe et al. (2009), at all the radius length cases and all the blending factor values cases, the mass of the droplet continuously increasing even when the simulation reached the steady stage.

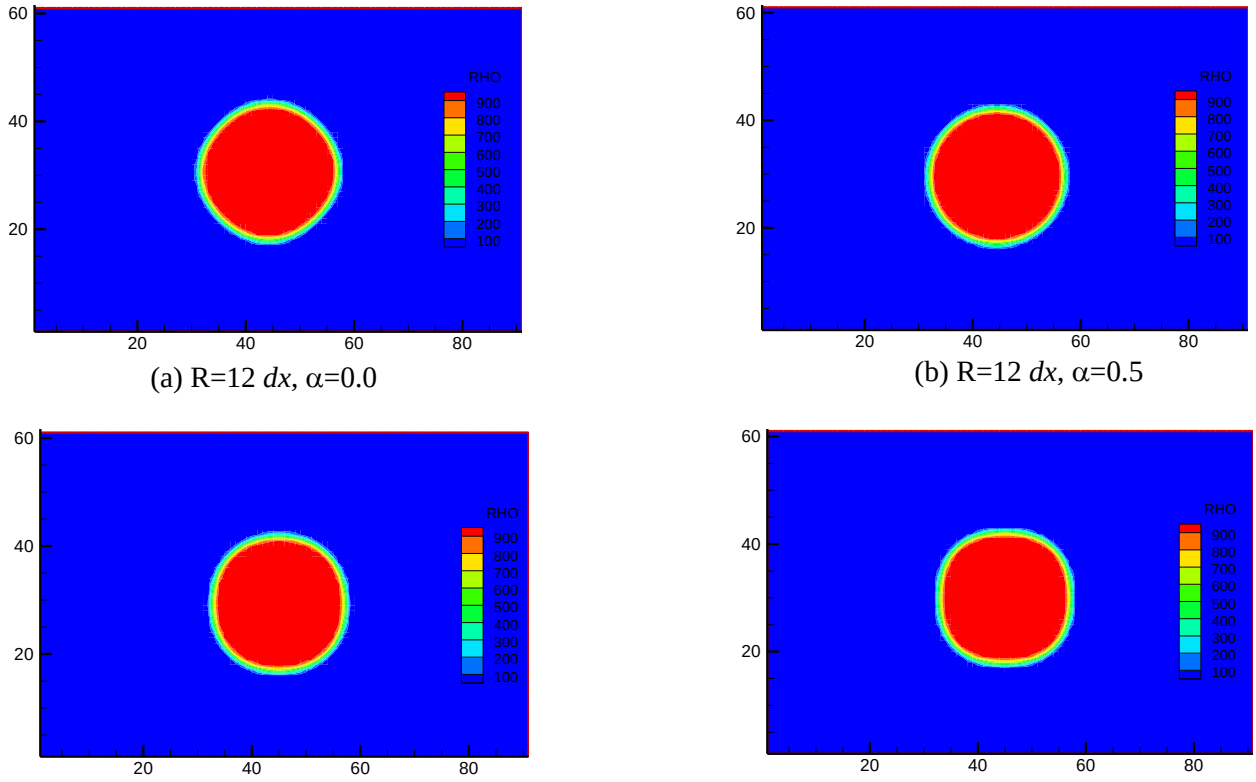

(a) R=12 *dx*, α=0.0 (b) R=12 *dx*, α=0.5

(c) R=12 *dx*, α=0.7 (d) R=12 *dx*, α=1.0

Fig. 1-1 Density distribution of a water droplet with typical blending factor α

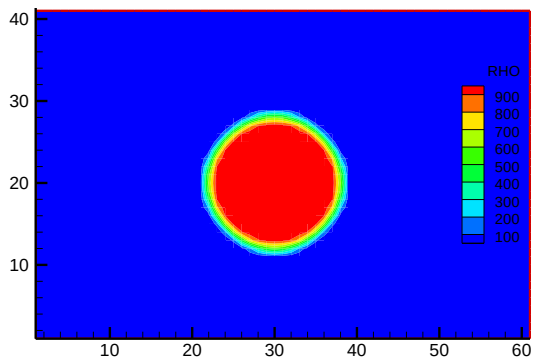

(a) R=8 *dx*, α=0.0

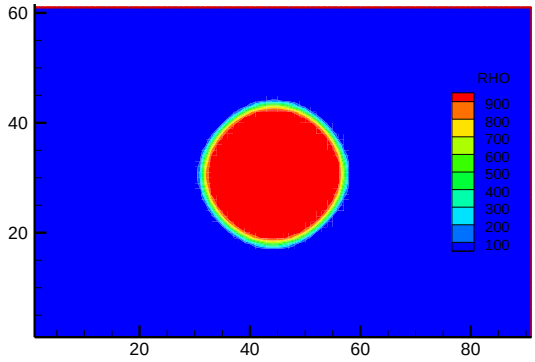

(b) R=12 *dx*, α=0.0

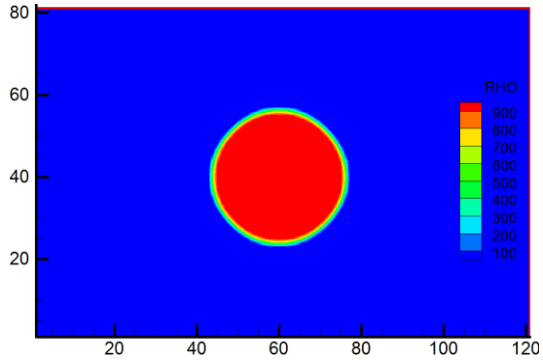

(c) R=16 *dx*, α=0.0

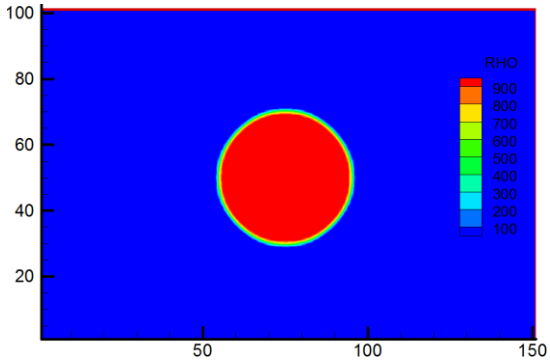

(d) R=20 *dx*, α=0.0

Fig. 1-2 Density distribution of a water droplet with α = 0.0 but different radii

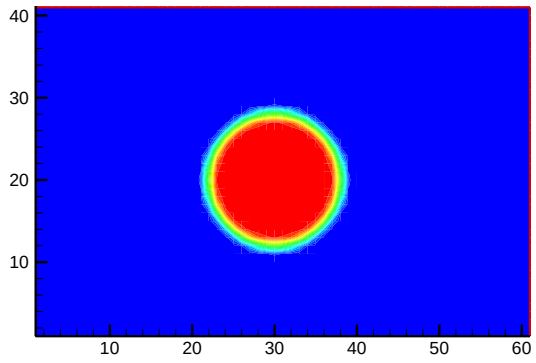

(a) R=8 *dx*, α=0.5

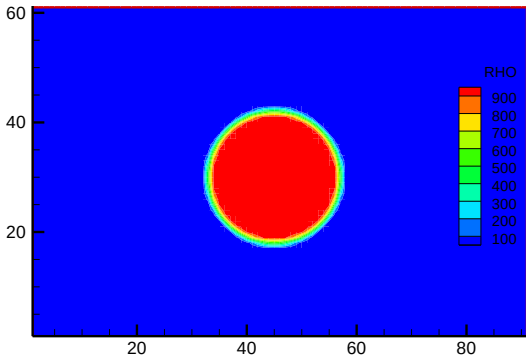

(b) R=12 *dx*, α=0.5

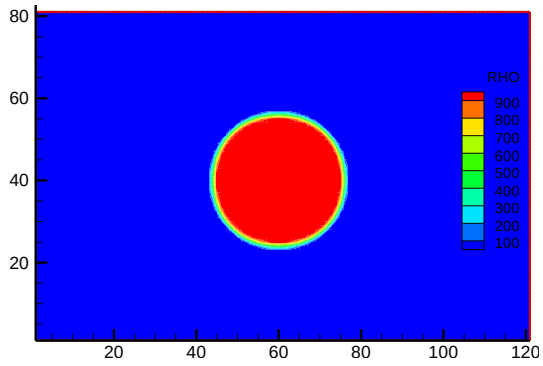

(c) R=16 *dx*, α=0.5

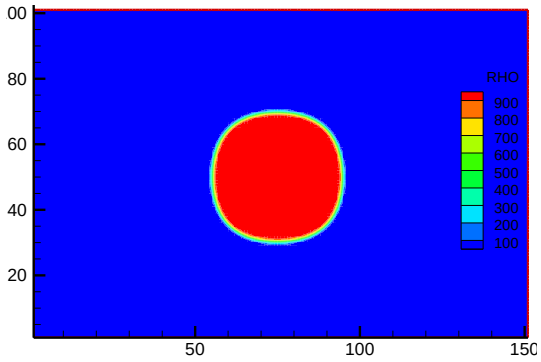

(d) R=20 *dx*, α=0.5

Fig. 1-3 Density distribution of a water droplet with α = 0.5 but different radii

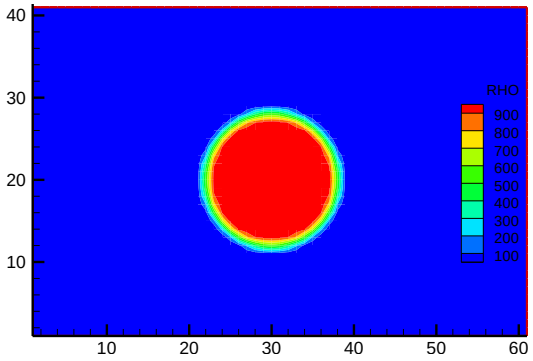

(a) R=8 *dx*, α=1.0

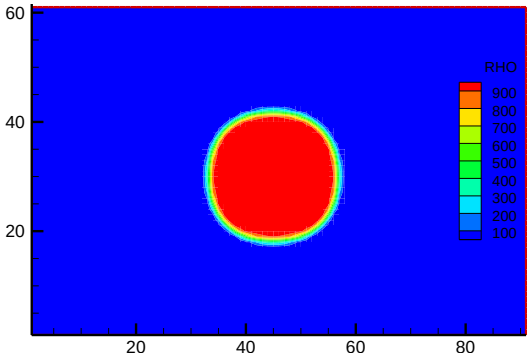

(b) R=12 *dx*, α=1.0

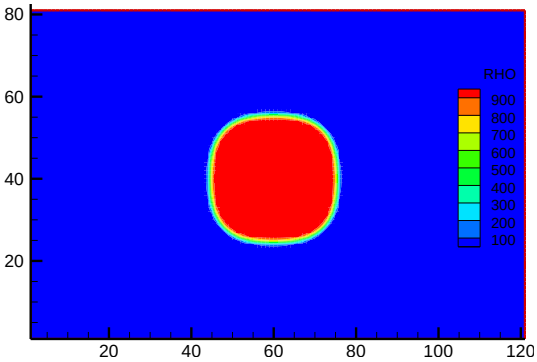

(c) R=16 *dx*, α=1.0

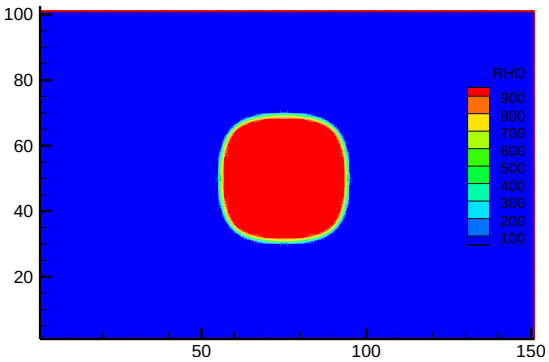

(d) R=20 *dx*, α=1.0

Fig. 1-4 Density distribution of a water droplet with α = 1.0 but different radii

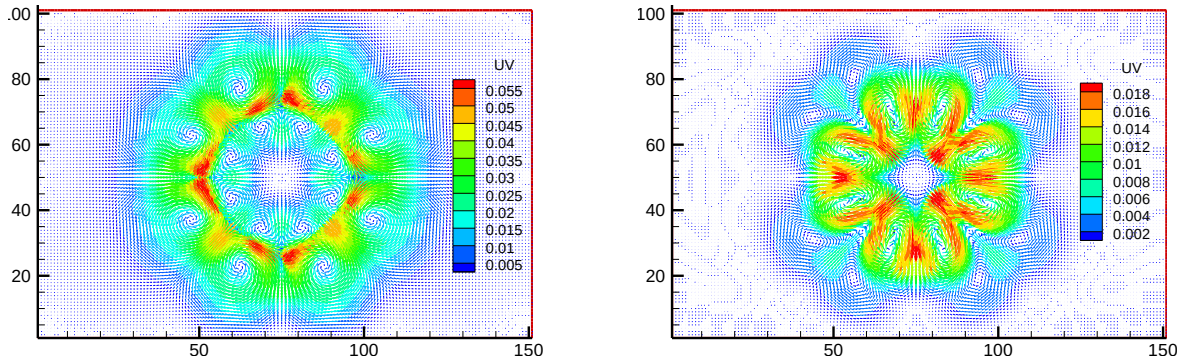

(a) R=20 *dx*, α=0.0 (b) R=20 *dx*, α=1.0

Fig. 1-5 Spurious velocity field of a water droplet with different blending factor α

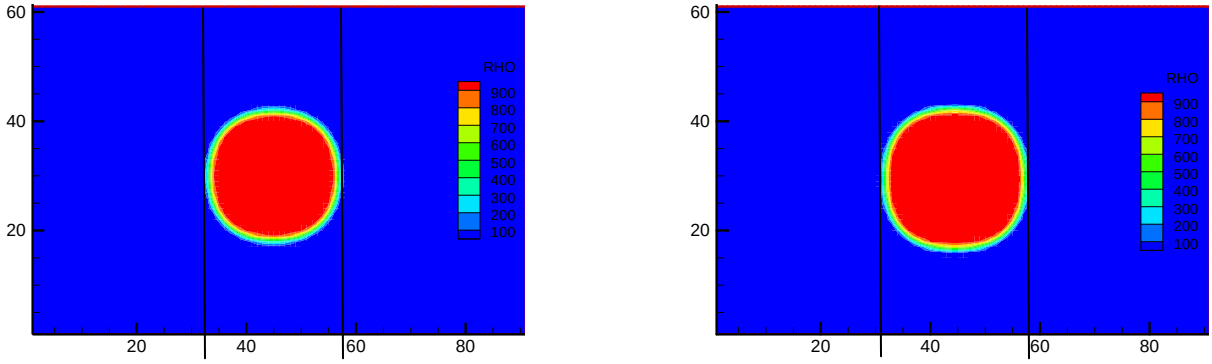

(a) Time step=10000 (b) Time step=10 million

Fig. 1-6 Volume of a water droplet at different time steps when R=12 *dx*, α = 1.0

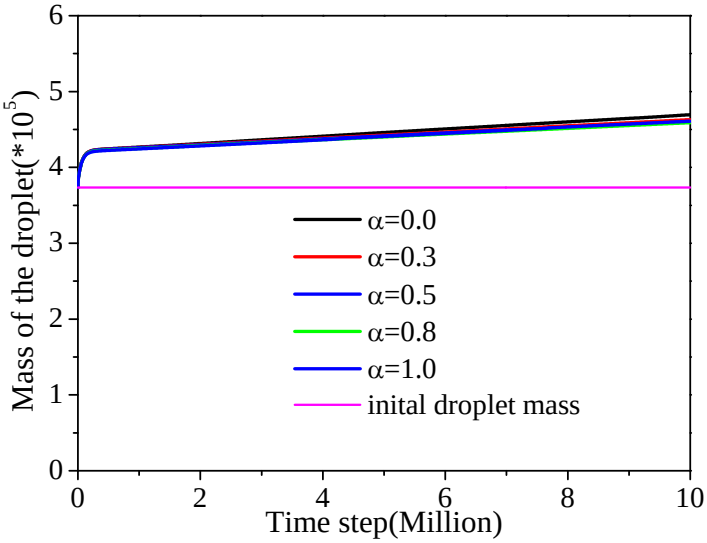

Fig. 1-7 Mass evolution history of a water droplet when R=12 dx, and typical α

Naturally, we want to know how these non-physical phenomena occurred in the simulation, how can we remove these abnormal phenomena and make these simulation results reliable, and what is the relationship between these phenomena and the heuristic treatments mentioned in the beginning of this section? To answer these questions, numerical analysis of the free energy based two-phase flow LBM model for large density ratio developed by Inamuro et al. (2004) was implemented in this dissertation, and several chapters listed below will be used to cover the topics discussed above.

Chapter 2, briefly introduces the models, parameters, schemes, and algorithms adopted in the free-energy-based LBM model for two-phase flow with large density ratios proposed by Inamuro et al. (2004), as well as the improvements made by Tabe et al. (2009).

Chapter 3, describes treatments of the boundary conditions adopted in the simulation, and explains how the 0-velocity inlet and free-out outlet boundary conditions make the volume and mass of droplet increase in the steady state by comparison with the simulation results from the periodic boundary conditions.

Chapter 4, explains and confirms the volume expansion and shape deformation mechanism in the unsteady stage.

Chapter 5, presents the appropriate blending factor of the two types of staggered grids adopted in the calculation of the approximate pressure Poisson equation for different radii based on the simulation results of the pressure distribution and the degree of shape deformation.

Chapter 6, describes how to reduce the spurious velocity by decreasing the profile difference between the order parameter and the density distribution which arises from the magnification and cut-off equation.

Chapter 7, provides a summary of the dissertation and general conclusions, and proposes future researches following the present work.

2 Free-energy-based LBM model for large density ratio

2.1 The basic LBM model for ideal gas

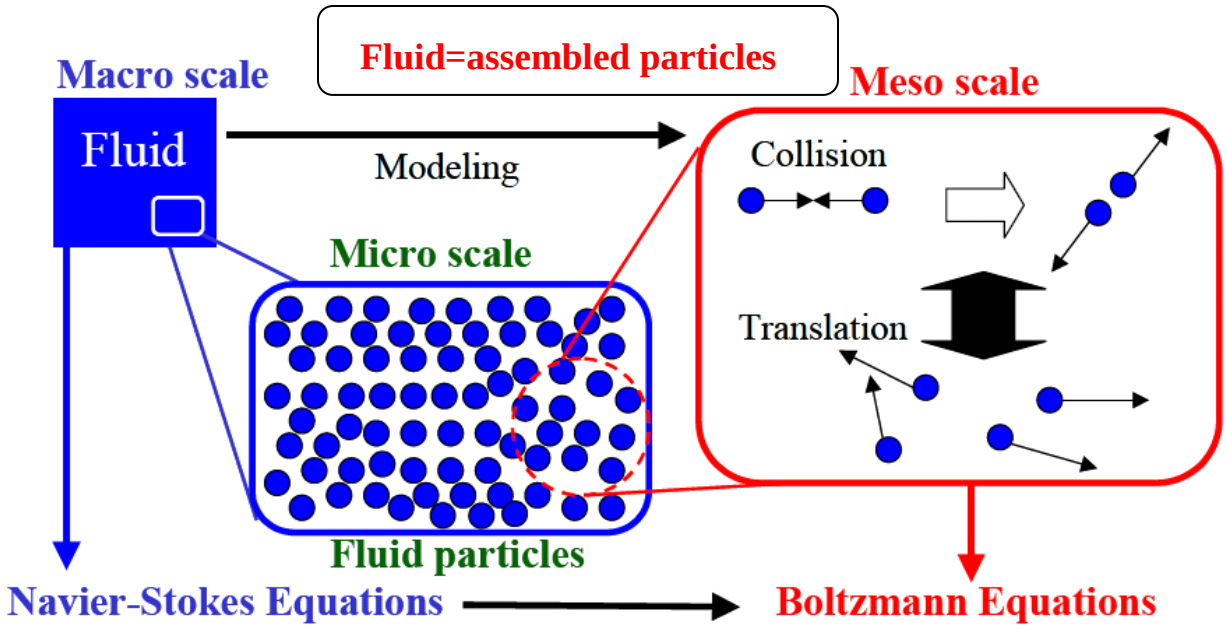

Fig. 2-1 Schematic diagram of the basic LBM concept

The basic lattice Boltzmann method (LBM) discretizes the macroscopic continuous fluid flow in time and space to the mesoscopic scale, and assumes the discretized particle groups in each lattice point satisfy the Maxwell equilibrium distribution. Unlike the atoms and the molecules that are totally discontinuously exists in space, the discretized fluid groups in the LBM are viewed as continuous particle assemblies, which exchange mass and momentum with the surrounding fluid groups by translation and collision process. In this method, the particle distribution function $f\left(\mathrm{x},t\right)$ is used to represent the particle numbers of the fluid particle group at the node (*x*, *t*). The lattice Boltzmann equation which describes the fluid flow can be written in the following form:

$$f_i(\mathbf{x}+\mathbf{c}_i\Delta t,t+\Delta t)=f_i\left(\mathbf{x},t\right)+\mathbf{\Omega}\left(f_i\left(\mathbf{x},t\right)\right), \qquad \textbf{2-1}$$

where, the subscript *i* represents the *i*-th direction that the particles in the fluid group are moving; $f_i\left(\mathrm{x},t\right)$ is the particle distribution function or the particle numbers moving along the *i*-th direction; and $\mathbf{\Omega}\left(f_i\left(\mathbf{x},t\right)\right)$ is the collision operator. Taking the BGK (Bhatnagar, Gross and Krook, 1954) approximation to $\mathbf{\Omega}\left(f_i\left(\mathbf{x},t\right)\right)$, the basic LBM equation (2-1) can be rewritten as:

$$f_i(\mathbf{x}+\mathbf{c}_i\Delta t, t+\Delta t) = f_i(\mathbf{x},t) - \frac{1}{\tau}\left[f_i(\mathbf{x},t) - f_i^{eq}(\mathbf{x},t)\right], \qquad 2\text{-}2$$

where, $f_i^{eq}(\mathbf{x},t)$ is the equilibrium distribution function.

The time evolution in the LBM is divided into two steps, the translation (streaming) and the collision steps. Taking the 2DV9 model (2 dimensions and 9 velocities, shown in Fig. 2-1) as an example, the lattice velocity vector is presented in Eq. (2-3). As shown in Fig. 2-2, in the streaming process, the particles $f_i(\mathrm{x},t)$ flow from their original lattice point along the *i*-th direction with the constant lattice speed c_i to the nearest lattice point; in the collision process, at the lattice point (x,t), the particle groups from the surrounding lattice points collide to exchange mass and momentum according to mass, momentum and the energy conservation laws and the assigned collision regulations. The collision process occurs in an instant, after that the transporting velocity of the fluid group at (x,t) changes.

$$\left[c_1,c_2,c_3,c_4,c_5,c_6,c_7,c_8,c_9\right] = \begin{bmatrix} 0 & 1 & 0 & -1 & 0 & 1 & -1 & -1 & 1 \\ 0 & 0 & 1 & 0 & -1 & 1 & 1 & -1 & -1 \end{bmatrix}, \qquad 2\text{-}3$$

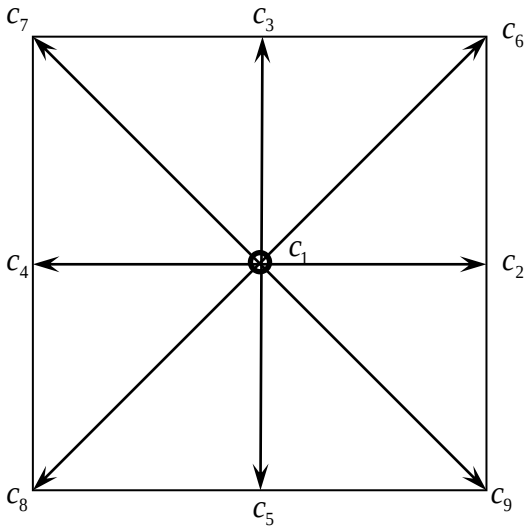

Fig. 2-2 The 2DV9 model

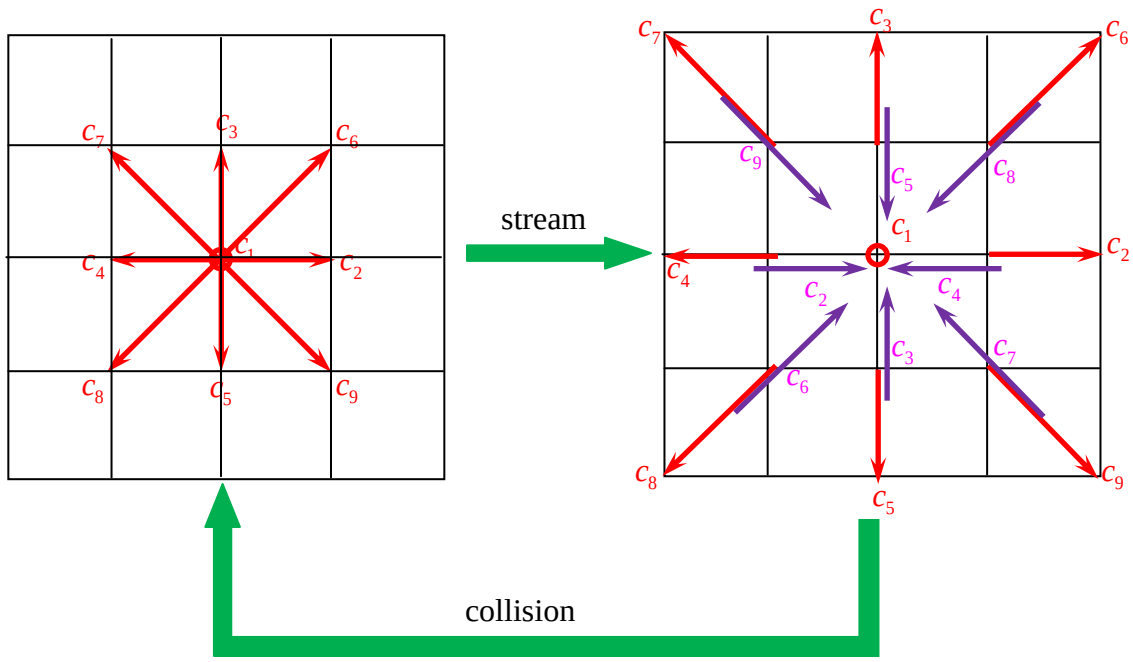

c_1

Fig. 2-3 Evolution history of the distribution function in one time step

Consistent with the descriptions above, the calculation of the LBM equation can be divided into two steps or processes in per time step: the collision step:

$$f_i^*(\mathbf{x},t) = f_i(\mathbf{x},t) - \frac{1}{\tau}\left[f_i(\mathbf{x},t) - f_i^{eq}(\mathbf{x},t)\right], \quad 2\text{-}4$$

And the stream step:

$$f_i(\mathbf{x}+\mathbf{c}_i\Delta t, t+\Delta t) = f_i^*(\mathbf{x},t), \quad 2\text{-}5$$

The macroscopic density, velocity and pressure can be acquired by:

$$\rho = \sum_{i=1}^{9} f_i, \quad 2\text{-}6$$

$$\rho\boldsymbol{u} = \sum_{i=1}^{9} f_i\mathbf{c}_i, \quad 2\text{-}7$$

$$p_0 = c_s^2\rho, \quad 2\text{-}8$$

The equilibrium distribution function in a DdQv (D dimensions and q discrete velocities) model can be expressed as:

$$f_i^{eq} = E_i \rho \left[1 + \frac{\boldsymbol{c}_i \cdot \boldsymbol{u}}{c_s^2} + \frac{\left(\boldsymbol{c}_i \cdot \boldsymbol{u}\right)^2}{2c_s^4} - \frac{\boldsymbol{u}^2}{2c_s^2} \right] \qquad 2\text{-}9$$

For the 2D9V model, $c_s = 1/\sqrt{3}$, and the constant weighting coefficients are $E_1 = 4/9$, $E_{2\sim5} = 1/9$, and $E_{6\sim9} = 1/36$.

By performing the Chapman-Enskog expansion or the so-called scale analysis on the Eq. (2-2), the macroscopic mass and momentum equations of the ideal gas can be recovered with the second order accuracy, as:

$$\frac{\partial \rho}{\partial t} + \frac{\partial \left(\rho u_\alpha\right)}{\partial x_\alpha} = 0, \qquad 2\text{-}10$$

$$\frac{\partial \left(\rho u_\alpha\right)}{\partial t} + \frac{\partial \left(\rho u_\alpha u_\beta\right)}{\partial x_\alpha} = \frac{\partial \sigma_{\alpha\beta}^{ideal\ gas}}{\partial x_\alpha}, \qquad 2\text{-}11$$

where, the ideal gas stress $\sigma_{\alpha\beta}^{ideal\ gas}$ can be described as:

$$\sigma_{\alpha\beta}^{ideal\ gas} = \rho c_s^2 \delta_{\alpha\beta} + \mu \left(\frac{\partial u_\alpha}{\partial x_\beta} + \frac{\partial u_\beta}{\partial x_\alpha} \right) \qquad 2\text{-}12$$

with $\delta_{\alpha\beta}$ being the Kronecker δ and μ the molecular viscosity.

2.2 The intermolecular interaction forces for non-ideal gas

In order to simulate the one-component-two-phase flow, intermolecular interaction forces should be included in the basic LBM model. Consider the momentum equation for the non-ideal gases,

$$\frac{\partial \left(\rho u_\alpha\right)}{\partial t} + \frac{\partial \left(\rho u_\alpha u_\beta\right)}{\partial x_\alpha} = \frac{\partial \sigma_{\alpha\beta}}{\partial x_\alpha} \qquad 2\text{-}13$$

.

The stresses, $\sigma_{\alpha\beta}$, in the force part of the Eq. (2-13), can be decomposed into three parts:

$$\sigma_{\alpha\beta} = p_0 - \sigma^{v}_{\alpha\beta} - \sigma^{l}_{\alpha\beta} . \qquad 2\text{-}14$$

Here, p_0^{non} is the thermodynamic pressure for the non-ideal isothermal fluid and $\sigma^{v}_{\alpha\beta}$ is the viscous stress tensor:

$$\sigma^{v}_{\alpha\beta} = \mu\left(\frac{\partial u_\alpha}{\partial x_\beta} + \frac{\partial u_\beta}{\partial x_\alpha}\right) - \frac{2}{3}\mu\frac{\partial u_\gamma}{\partial x_\gamma}\delta_{\alpha\beta} . \qquad 2\text{-}15$$

The second term on the right hand side of Eq. (2-15) is the bulk viscosity term, which is removed in the incompressible fluid. The stress, $\sigma^{l}_{\alpha\beta}$, is defined as the stress coming from the interface effect, and according to the Cahn-Hilliard free energy theory, it takes the following form:

$$\sigma^{l}_{\alpha\beta} = \kappa\left[\left(\frac{1}{2}\frac{\partial\rho}{\partial x_\gamma}\frac{\partial\rho}{\partial x_\gamma} + \rho\frac{\partial^2\rho}{\partial x_\gamma\partial x_\gamma}\right)\delta_{\alpha\beta} - \frac{\partial\rho}{\partial x_\alpha}\frac{\partial\rho}{\partial x_\beta}\right], \qquad 2\text{-}16$$

where, the parameter κ is a constant and is related to the magnitude of the interface tension.

Comparing the detailed forms on the right hand sides of Eqs. (2-11) and Eq. (2-13), it indicates that intermolecular stress, $\sigma_{\alpha\beta}$, can be written as:

$$\sigma_{\alpha\beta} = p_0^{non} - \kappa\left[\left(\frac{1}{2}\frac{\partial\rho}{\partial x_\gamma}\frac{\partial\rho}{\partial x_\gamma} + \rho\frac{\partial^2\rho}{\partial x_\gamma\partial x_\gamma}\right)\delta_{\alpha\beta} - \frac{\partial\rho}{\partial x_\alpha}\frac{\partial\rho}{\partial x_\beta}\right] \qquad 2\text{-}17$$

and, Eq. (2-17) is also called the thermodynamic tensor and can be expressed as:

$$P_{\alpha\beta} = \left(p_0^{non} - \rho\kappa\frac{\partial^2\rho}{\partial x_\gamma\partial x_\gamma} - \frac{1}{2}\kappa\frac{\partial\rho}{\partial x_\gamma}\frac{\partial\rho}{\partial x_\gamma}\right)\delta_{\alpha\beta} + \kappa\frac{\partial\rho}{\partial x_\alpha}\frac{\partial\rho}{\partial x_\beta} \qquad 2\text{-}18$$

The resulting intermolecular force can be written as

$$F_\alpha = \frac{\partial}{\partial x_\beta}\left(p_0^{non} - \rho\kappa\frac{\partial^2\rho}{\partial x_\gamma\partial x_\gamma} - \frac{1}{2}\kappa\frac{\partial\rho}{\partial x_\gamma}\frac{\partial\rho}{\partial x_\gamma}\right)\delta_{\alpha\beta} + \kappa\frac{\partial}{\partial x_\beta}\left(\frac{\partial\rho}{\partial x_\alpha}\frac{\partial\rho}{\partial x_\beta}\right) \qquad 2\text{-}19$$

The thermodynamic pressure , p_0^{non} , can be determined from the equation of state (EOS) for non-ideal gas, such as the van der Waals EOS, the Redlich-Kwong (R-K) EOS, the Redlich-Kwong Soave (RKS)

EOS, the Peng-Robinson (P-R) EOS, and the Carnahan-Starling (C-S) EOS (Yuan and Schaefer, 2006). The van der Waals EOS is the most common EOS adopted in the free energy based LBM model, and it can be expressed as:

$$p_0^{non} = \rho T \frac{1}{1-b\rho} - a\rho^2 \qquad 2\text{-}20$$

Here, T is the temperature of the van der Waals fluid, a is the attraction parameter and b is the repulsion parameter. The a, b, and T values can be adjusted to determine the maximum and minimum values of ρ for the modeled fluid. Fig. 2-4 shows a diagram of distribution of $p_0^{non} - \rho$; there are three regions, A, B and C, which correspond to the unstable region, the meta-stable region, and the stable region, respectively. The states with $\rho < \rho_\alpha$ are viewed as the vapor state and the states where $\rho > \rho_\beta$ are viewed as the liquid phase. The region *A*, where $\rho_\alpha < \rho < \rho_\beta$, is the mechanically unstable region with negative $\partial_\rho p_0^{non}$, which separates the liquid and vapor phases of the fluid. In the later parts of this dissertation, which mainly discusses the two-phase flow model in which only the non-ideal gas model is adopted, the superscript 'non' in the thermodynamic pressure p_0^{non} is removed for simplicity.

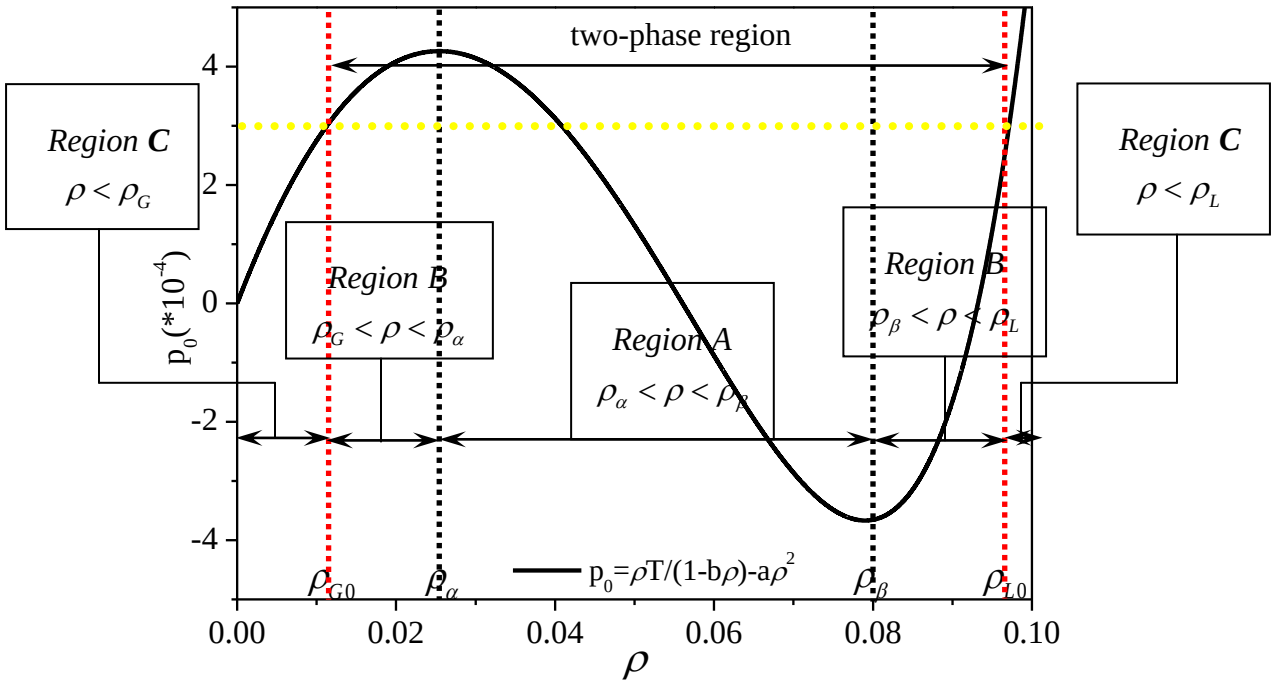

Fig. 2-4 $p_0^{non} - \rho$ isotherm diagram at a = 1, b = 6.7 and T = 0.035

The interfacial tension force in the intermolecular forcing terms of Eq. (2-19) can be recast in either the stress forms or the potential forms with the help of vector identities. Consequently, the total intermolecular force F_α can be expressed in the stress forms and the potential forms. The stress forms of the interfacial tension force are the best forms if momentum conservation is important, while the potential forms are more suitable when phase separation is important (Jacmin, 1996; Lee and Lin, 2005). Because of different definitions and arrangements between the pressure and the interfacial tension components of Eq. (2-18), one stress form of the intermolecular force can be written as,

$$F_\alpha^{S1} = \frac{\partial}{\partial x_\alpha}(p_0 - \kappa\rho\frac{\partial^2\rho}{\partial x_\alpha^2})\delta_{\alpha\beta} - \kappa\frac{\partial}{\partial x_\alpha}\left(\frac{1}{2}\left(\frac{\partial\rho}{\partial x_\alpha}\right)^2\delta_{\alpha\beta} - \frac{\partial\rho}{\partial x_\alpha}\frac{\partial\rho}{\partial x_\beta}\right) \qquad 2\text{-}21$$

The superscript $S1$ in F_α^{S1} represents the first stress form; and the first and second terms on the right hand side of Eq. (2-21) are the corresponding forms of the pressure gradient force and the interfacial tension force. This stress form of the intermolecular force is adopted by Swift et al. (1995, 1996), and Inamuro et al. (2000), and in the works following their approaches (Seta and Okui, 2007; Pooley and Furtado, 2008). As pointed out by Inamuro et al. (2000), and Yang and Fleming (1976), the hydrodynamic pressure, p_H, works as the pressure in the interface and it was defined as the following,

$$p_H = p_0 - \kappa\rho\frac{\partial^2\rho}{\partial x_\alpha^2} + \frac{\kappa}{2}\left(\frac{\partial\rho}{\partial x_\alpha}\right)^2. \qquad 2\text{-}22$$

The intermolecular force shown in Eq. (2-19) can be rewritten as,

$$F_\alpha^{S2} = \frac{\partial}{\partial x_\alpha}(p_0 - \kappa\rho\frac{\partial^2\rho}{\partial x_\alpha^2} + \frac{\kappa}{2}\left(\frac{\partial\rho}{\partial x_\alpha}\right)^2)\delta_{\alpha\beta} - \kappa\frac{\partial}{\partial x_\alpha}(\frac{1}{2}\left(\frac{\partial\rho}{\partial x_\alpha}\right)^2)\delta_{\alpha\beta} - \kappa\frac{\partial}{\partial x_\alpha}\left(\frac{1}{2}\left(\frac{\partial\rho}{\partial x_\alpha}\right)^2\delta_{\alpha\beta} - \frac{\partial\rho}{\partial x_\alpha}\frac{\partial\rho}{\partial x_\beta}\right). \qquad 2\text{-}23$$

Where, the superscript $S2$ in the F_α^{S2} represents the second stress form of the intermolecular force; and such form was adopted by Inamuro et al (2004) with a special treatment in the distribution function g_i to get the velocity, which was followed by Tabe et al (2009, 2012) and this paper. Following the definition of hydrodynamic pressure p_H, Lee and Lin (2005) adopted another stress form of interfacial tension force and recast Eq. (2-19) into the third stress form of the intermolecular force,

$$F_\alpha^{S3} = \frac{\partial}{\partial x_\alpha}(p_0 - \kappa\rho\frac{\partial^2\rho}{\partial x_\alpha^2} + \frac{\kappa}{2}\left(\frac{\partial\rho}{\partial x_\alpha}\right)^2)\delta_{\alpha\beta} - \kappa\frac{\partial}{\partial x_\alpha}\left[\left(\frac{\partial\rho}{\partial x_\alpha}\right)^2\delta_{\alpha\beta} - \frac{\partial\rho}{\partial x_\alpha}\frac{\partial\rho}{\partial x_\beta}\right]. \quad \text{2-24}$$

Here, the superscript $S3$ in the F_α^{S3} represents the third stress form. Comparing Eqs. (2-23) and (2-24), it is found that the second term on the right hand side of Eq. (2-23) is absorbed into the interfacial tension force term in Eq. (2-24), which is the second term on the right hand side of Eq. (2-24). The interfacial tension force term in Eq. (2-24) is different from that in Eqs. (2-21) and (2-23), due to the different definition; however, both the two stress forms of the interfacial tension force in the three equations keep the divergence-free condition. The principle axes of the interfacial tension force in the two forms are directed in and perpendicular to the tangent plane of the interface; the normal stress perpendicular to the plane is zero and the two tangent normal stresses are equal (Jacmin, 1996; Lee and Lin, 2005).

With some algebraic manipulation, the intermolecular force in the stress forms can be rewritten in a potential form,

$$F_\alpha^{P1} = \frac{\partial}{\partial x_\alpha}(p_0)\delta_{\alpha\beta} - \kappa\rho\frac{\partial}{\partial x_\alpha}\left[\left(\frac{\partial^2\rho}{\partial x_\alpha^2}\right)\right] \quad \text{2-25}$$

where, the superscript $P1$ in the F_α^{P1} represents the first potential form. In Eq. (2-25), both the pressure component and the interface tension component are treated as scalar. This form of the intermolecular force is adopted in the one distribution function model of Lee (Lee and Fischer, 2006; Connington and Lee, 2012). According to the thermodynamics of the free energy model, there is a relation between the thermodynamic pressure, p_0, and the chemical potential, μ_0 (Lee and Lin, 2005; Lee and Fischer, 2006; Connington and Lee, 2012), as shown in Eq. (2-26);

$$\frac{\partial p_0}{\partial x_\alpha} = \rho\frac{\partial\mu_0}{\partial x_\alpha}. \quad \text{2-26}$$

With this relation, Eq. (2-25) can be further recast as;

$$F_\alpha^{P2} = \frac{\partial}{\partial x_\alpha}(\mu_0 - \kappa\frac{\partial^2\rho}{\partial x_\alpha^2}), \quad \text{2-27}$$

where, the superscript $P2$ in F_α^{P2} represents the second potential form, and the term inside the gradient operator on the right hand is treated as a scalar. Such a form is adopted by Wagner (2003), Lee and Lin (2005), Zheng et al. (2006) and Lee and Fischer (2006) for the calculation of velocity.

2.3 Free-energy-based two-phase flow LBM with large density ratio

In the free-energy-based two-phase flow LBM model for large density ratio, which was proposed by Inamuro et al. (2004) and developed by Tabe et al. (2009), two particle velocity distribution functions are used, namely the f_i and g_i. The first particle velocity distribution function, f_i, is used in the calculation of an order parameter, ϕ, that distinguishes two phases; $\phi < \phi_G$ corresponds to the gas phase, $\phi_G \le \phi \le \phi_L$ corresponds to the interface, and $\phi > \phi_L$ corresponds to the liquid phase. The function g_i is used to calculate the predicted velocity of the two-phase fluid, in the absence of a pressure gradient. The evolution functions of the two-particle velocity distribution functions f_i and g_i are described by Eqs. (2-28) and (2-29):

$$f_i(\mathbf{x}+\mathbf{c}_i\Delta t, t+\Delta t) = f_i(\mathbf{x},t) - \frac{1}{\tau_f}\cdot\left(f_i(\mathbf{x},t) - f_i^{eq}(\mathbf{x},t)\right), \tag{2-28}$$

$$g_i(\mathbf{x}+\mathbf{c}_i\Delta t, t+\Delta t) = g_i(\mathbf{x},t) - \frac{1}{\tau g}\left(g_i(\mathbf{x},t) - g_i^{eq}(\mathbf{x},t)\right) + \frac{3E_i c_{i\alpha}}{\rho}\left[\frac{\partial}{\partial x_\beta}\left\{\mu\left(\frac{\partial u_\beta}{\partial x_\alpha}+\frac{\partial u_\alpha}{\partial x_\beta}\right)\right\}\right]\Delta x. \tag{2-29}$$

Here, f_i^{eq} and g_i^{eq} are the equilibrium distribution functions, τ_f and τ_g are the dimensionless single relaxation times, E_i are the associated weight coefficients, Δx is the spacing of the squared lattice, Δt is the time step during which the particles travel across the distance of a lattice spacing, ρ is the density, μ is the viscosity and $\boldsymbol{u}$ is the current velocity. The subscripts α and β represent Cartesian coordinates, and the Einstein summation convention is used. The last terms on the right side of Eq. (2-29) represents the effects related to viscous stress, and in this dissertation the gravitation term was not considered. The two-dimensional (2D), 9-velocities model (the 2D9V model) is used in the LBM model, and the lattice velocity directions are shown in Fig. 2-2.

The order parameter, ϕ, distinguishing the two phases, and the predicted velocity, $\boldsymbol{u}^*$, of the multi-phase fluid are defined in terms of the two-particle velocity distribution functions, as shown below:

$$\phi = \sum_{i=1}^{9} f_i \quad , \tag{2-30}$$

$$\boldsymbol{u}^* = \sum_{i=1}^{9} \boldsymbol{c}_i g_i \quad . \tag{2-31}$$

The equilibrium distribution functions, f_i^{eq} and g_i^{eq}, in Eqs. (2-28) and (2-29), are given by the following equations:

$$f_i^{eq} = H_i\phi + F_i\left[p_0 - \kappa_f\phi\frac{\partial^2\phi}{\partial x_\alpha^2} - \frac{\kappa_f}{6}\left(\frac{\partial\phi}{\partial x_\alpha}\right)^2\right] + 3E_i\phi c_{i\alpha}u_\alpha + E_i\kappa_f G_{\alpha\beta}(\phi)c_{i\alpha}c_{i\beta} \quad , \tag{2-32}$$

$$g_i^{eq} = E_i\left[1 + 3c_{i\alpha}u_\alpha - \frac{3}{2}u_\alpha u_\alpha + \frac{9}{2}c_{i\alpha}c_{i\beta}u_\alpha u_\beta + \frac{3}{2}\left(\tau g - \frac{1}{2}\right)\times\Delta x\left(\frac{\partial u_\beta}{\partial x_\alpha} + \frac{\partial u_\alpha}{\partial x_\beta}\right)c_{i\alpha}c_{i\beta}\right] + E_i\frac{\kappa_g}{\hat{\rho}}G_{\alpha\beta}(\rho)c_{i\alpha}c_{i\beta} - \frac{1}{2}F_i\frac{\kappa_g}{\rho}|\nabla\rho|^2 \quad , \tag{2-33}$$

with,

$$G_{\alpha\beta}(\lambda) = \frac{9}{2}\frac{\partial\lambda}{\partial x_\alpha}\frac{\partial\lambda}{\partial x_\beta} - \frac{9}{4}\frac{\partial\lambda}{\partial x_\gamma}\frac{\partial\lambda}{\partial x_\gamma}\delta_{\alpha\beta} \quad , \tag{2-34}$$

$$\begin{aligned} &E_1 = \frac{4}{9}, E_2 = \cdots E_5 = \frac{1}{9}, E_6 = \cdots E_9 = \frac{1}{36} \\ &H_1 = 1, H_2 = \cdots H_9 = 0 \\ &F_1 = -\frac{5}{3}, F_i = 3E_i(2,3,\cdots,9) \end{aligned} \quad , \tag{2-35}$$

where, α,β,γ are the Cartesian coordinates following the summation convection, $\delta_{\alpha\beta}$ is the Kronecker delta, κ_f is a constant parameter that determines the interface width between the two phases, and κ_g is a constant parameter that determines the strength of the interface tension of the liquid water/gas system. Additionally, λ is the free parameter used to represent ϕ and ρ in Eqs. (2-32) and (2-33), respectively. Correspondingly, p_0, is the pressure of the van der Waals fluid described by ϕ, where the equation of state (EOS) is defined by

$$p_0 = \phi\frac{\partial\psi}{\partial\phi} - \psi = \phi T\frac{1}{1-b\phi} - a\phi^2 \quad , \tag{2-36}$$

Here, ψ is the bulk free-energy density, and a, b and T are free parameters determining the maximum and minimum values of the order parameter ϕ. In this dissertation, values of a = 1, b = 6.7, and T = 3.5×10^{-2} were used.

The interface tension is obtained for the liquid water/gas system by

$$\sigma = \kappa_g \int_{-\infty}^{\infty} \left(\frac{\partial \rho}{\partial \xi_\rho} \right)^2 d\xi_\rho, \tag{2-37}$$

where, ξ_ρ is the coordinate perpendicular to the interface between the liquid water and the gas.

The densities of the liquid water and gas can be calculated by the magnification and cut-off equation:

$$\rho = \begin{cases} \rho_G, & \phi \le \phi_G \\ \dfrac{\Delta\rho}{2}\left[\sin\left(\dfrac{\phi - \bar{\phi}}{\Delta\phi}\pi \right) + 1 \right] + \rho_G, & \phi_G < \phi < \phi_L \\ \rho_L, & \phi \ge \phi_L \end{cases}, \tag{2-38}$$

where,

$$\Delta\rho = \rho_L - \rho_G, \Delta\phi = \phi_L - \phi_G, \bar{\phi} = \frac{\phi_L + \phi_G}{2} \tag{2-39}$$

ρ_L and ρ_G are, respectively, the densities of the liquid and gas phases in the two-phase flow system with large density ratio.

The viscosity coefficient can be acquired by

$$\mu = \frac{\rho - \rho_G}{\rho_L - \rho_G}\left(\mu_L - \mu_G \right) + \mu_G \tag{2-40}$$

Since the predicted velocity $\boldsymbol{u}^*$ calculated by Eq. (2-31) does not satisfy the continuity equation ($\nabla \cdot \boldsymbol{u}^* = 0$), a correction to $\boldsymbol{u}^*$ is needed. The current velocity, $\boldsymbol{u}$, that satisfies the continuity equation can be obtained by the fractional step method or the so-called projection method with the following equations:

$$\nabla\cdot\left(\frac{\nabla p}{\rho}\right)=Sh\frac{\nabla\cdot\boldsymbol{u}^{*}}{\Delta t} \tag{2-41}$$

$$Sh\frac{\boldsymbol{u}-\boldsymbol{u}^{*}}{\Delta t}=-\frac{\nabla p}{\rho} \tag{2-42}$$

where, $Sh=U/c$ is the Strouhal number and p is the pressure of the liquid water/gas two-phase system.

The derivatives in the model can be approximated by the following schemes:

$$\frac{\partial\phi}{\partial x_{\alpha}}\approx\frac{1}{6\Delta x}\sum_{i=2}^{9}c_{i\alpha}\phi\left(x+c_{i}\Delta x\right) \tag{2-43}$$

$$\nabla^{2}\phi\approx\frac{1}{3\Delta x}\left[\sum_{i=2}^{9}c_{i\alpha}\phi\left(x+c_{i}\Delta x\right)-8\cdot\phi\left(x\right)\right] \tag{2-44}$$

In order to reduce the magnitude of the spurious velocity which arises in the vicinity of the interface region, Tabe et al. (2009) improved the calculation of the derivative $\frac{\partial\rho}{\partial x_{\alpha}}$ by using the following equation:

$$\frac{\partial\rho}{\partial x_{\alpha}}=\begin{cases}0, & \phi\le\phi_{G}\\ \dfrac{\Delta\rho}{2}\cdot\dfrac{\pi}{\Delta\phi}\cdot\dfrac{\partial\phi}{\partial x_{\alpha}}\cos\left(\dfrac{\phi-\bar{\phi}}{\Delta\phi}\pi\right)+\rho_{G}, & \phi_{G}<\phi<\phi_{L}\\ 0, & \phi\ge\phi_{L}\end{cases} \tag{2-45}$$

The first and the second stress forms of the intermolecular force terms as shown in Eqs. (2-21) and (2-23) are adopted in the f_{i}^{eq} and g_{i}^{eq} equations (as shown in Eqs.(2-32) and (2-33)), respectively, with some necessary modifications and special treatments from Eq. (2-46), as illustrated in the following ways:

For the f_{i}^{eq} equation:

$$F_{\alpha}^{S1}=\frac{\partial}{\partial x_{\alpha}}(p_{0}-\kappa\lambda\frac{\partial^{2}\lambda}{\partial x_{\alpha}^{2}})\delta_{\alpha\beta}-\kappa\frac{\partial}{\partial x_{\alpha}}\left(\frac{1}{2}\left(\frac{\partial\lambda}{\partial x_{\alpha}}\right)^{2}\delta_{\alpha\beta}-\frac{\partial\lambda}{\partial x_{\alpha}}\frac{\partial\lambda}{\partial x_{\beta}}\right), \tag{Re(2-20)}$$

$$f_{i}^{eq}=H_{i}\phi+F_{i}\left[p_{0}-\kappa_{f}\phi\frac{\partial^{2}\phi}{\partial x_{\alpha}^{2}}-\frac{\kappa_{f}}{6}\left(\frac{\partial\phi}{\partial x_{\alpha}}\right)^{2}\right]+3E_{i}\phi c_{i\alpha}u_{\alpha}+E_{i}\kappa_{f}G_{\alpha\beta}\left(\phi\right)c_{i\alpha}c_{i\beta} \tag{Re(2-31)}$$

As shown above, an additional term is added to the pressure part of Eq. (2-32) to reduce the mobility, such that the numerical instability can be reduced. Moreover, the terms in Eq. (2-9) that are not related to mass conservation are removed. Equivalently, Eq. (2-32) is comprised of the terms from the Cahn-Hilliard equation and an advection term. Such treatments make Eq. (2-32) a type of level-set method function. From this equation, it can also be found that the distribution for ϕ (or ρ), or the droplet shape, is determined by the pressure gradient, the interface tension force, and the velocity effect.

For the g_i^{eq} equation,

$$F_\alpha^{S2} = \frac{\partial}{\partial x_\alpha}\left(p_0 - \kappa\lambda\frac{\partial^2\lambda}{\partial x_\alpha^2} + \frac{\kappa}{2}\left(\frac{\partial\lambda}{\partial x_\alpha}\right)^2\right)\delta_{\alpha\beta}$$
$$-\kappa\frac{\partial}{\partial x_\alpha}\left(\frac{1}{2}\left(\frac{\partial\lambda}{\partial x_\alpha}\right)^2\right)\delta_{\alpha\beta} - \kappa\frac{\partial}{\partial x_\alpha}\left(\frac{1}{2}\left(\frac{\partial\lambda}{\partial x_\alpha}\right)^2\delta_{\alpha\beta} - \frac{\partial\lambda}{\partial x_\alpha}\frac{\partial\lambda}{\partial x_\beta}\right) \quad \text{Re(2-22)}$$

$$g_i^{eq} = E_i\left[1 + 3c_{i\alpha}u_\alpha - \frac{3}{2}u_\alpha u_\alpha + \frac{9}{2}c_{i\alpha}c_{i\beta}u_\alpha u_\beta + \frac{3}{2}\left(\tau_g - \frac{1}{2}\right)\times\Delta x\left(\frac{\partial u_\beta}{\partial x_\alpha} + \frac{\partial u_\alpha}{\partial x_\beta}\right)c_{i\alpha}c_{i\beta}\right] \quad \text{Re(2-32)}$$
$$-\frac{1}{2}F_i\frac{\kappa_g}{\rho}|\nabla\rho|^2 + E_i\frac{\kappa_g}{\hat{\rho}}G_{\alpha\beta}(\rho)c_{i\alpha}c_{i\beta}$$

The τ_g related term in Eq. (2-33) represents the viscosity related force term, and the hydrodynamic pressure part of the intermolecular force, as the part underlined in red, is not included. The reason is that, according to the asymptotic analysis, at low Mach numbers the pressure of the two-phase flow can be split into two parts; namely, the thermodynamic pressure that is uniform in space, and the hydrodynamic pressure that is several orders of magnitude smaller than the thermodynamic pressure (Lee and Lin, 2005). Further, the calculation of the hydrodynamic pressure, p_H, in the intermolecular force term increases the numerical instability. In the small density ratio case, the p_H term can be usually omitted. However, in the large density ratio case, the p_H term becomes much larger, and its effect cannot be neglected; otherwise, the continuity equation cannot be satisfied in the interface region. Instead of calculating the hydrodynamic pressure defined by Eq. (2-22) and adding it to Eq. (2-33), the fractional step method based on the Poisson equation (Eqs. (2-41) and (2-42)) is used to extract the p_H value and improve the predicted velocity. Therefore, in this analysis, the pressure in the Poisson equation is the hydrodynamic pressure.

2.4 Iteration methods and grid types used in the fractional step method

In Inamuro's model for two-phase flow with large density ratio, the Poisson equation is solved in the framework of LBM and in this framework the velocity and the pressure are defined at the same grid point, which is called co-location grid, as shown in Fig. 2-5. Namely, the following evolution equation of the velocity distribution function h_i is adopted to calculate the pressure instead of Eq. (2-41):

$$h_i^{n+1}(\boldsymbol{x}+\boldsymbol{c}_i\Delta x)=h_i^n(\boldsymbol{x})-\frac{1}{\tau_h}\left[h_i^n(\boldsymbol{x})-E_i p^n(\hat{\boldsymbol{x}})\right]-\frac{1}{3}E_i\frac{\partial u_\alpha^*}{\partial x_\alpha}\Delta x \quad , \tag{2-47}$$

where, n is the number of iterations and the relaxation time τ_h is given by

$$\tau_h=\frac{1}{\rho}+\frac{1}{2} \quad . \tag{2-48}$$

The pressure is acquired by:

$$p=\sum_{i=1}^{9}h_i \quad , \tag{2-49}$$

where n is the number of iterations and τ_h is the relaxation time. As shown in Eq. (2-47) and Eq. (2-49), in this scheme both the velocities in orthogonal and diagonal directions shown in Fig. 2-2 were taken into account.

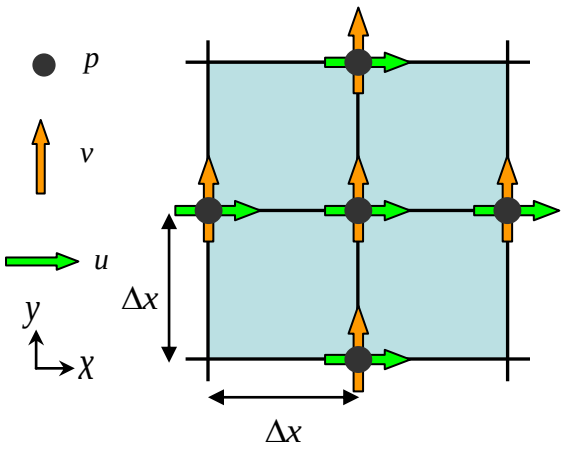

Fig. 2-5 Co-location grid

Tabe et al. (2009) previously solved the Poisson equation by using the SOR method, because of its easier implementation and faster calculation speed compared with the LBM scheme. In the SOR method, the calculation that uses the co-location grid to solve the Poisson equation often induces spatial pressure oscillations, as shown in Fig. 2-6. To prevent such oscillations, pressure–velocity iteration formulations based on two kinds of staggered grids (shown in Fig. 2-7 (a) and (b)) that shift the velocity definition points to the boundaries of the conservation volume units were derived to solve the Poisson equation.

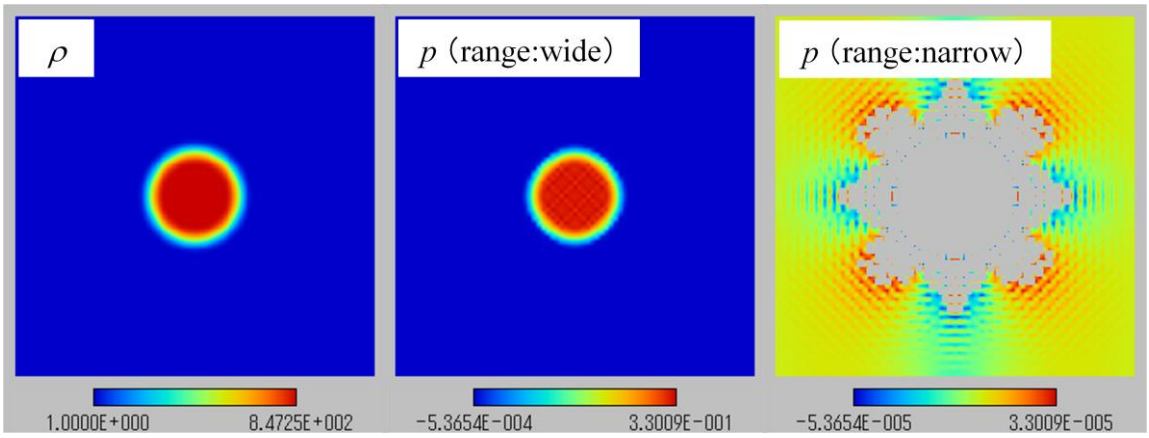

Fig. 2-6 Sketch of the pressure oscillation (Lee, 2009)

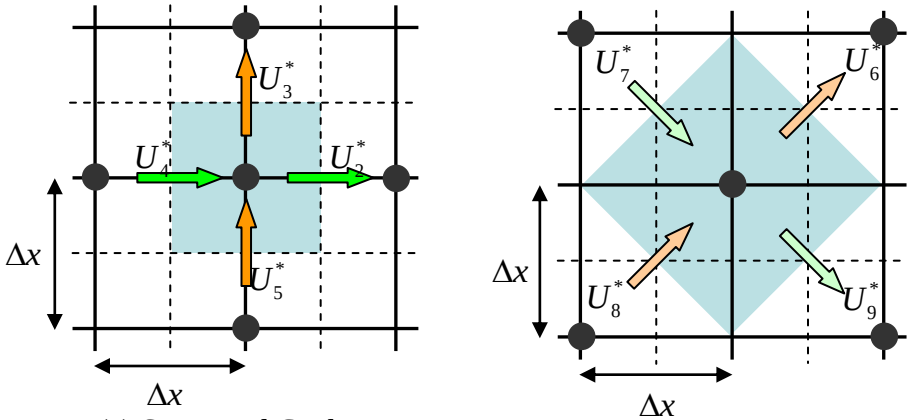

(a) Staggered Grid 1 (b) Staggered Grid 2

Fig. 2-7 Staggered grids adopted in the SOR iteration

For Staggered Grid 1 shown in Fig. 2-7(a), the discrete form of the left-hand part of Eq. (2-41) is:

$$\nabla\cdot\left(\frac{\nabla p}{\rho}\right)\approx\frac{p_{i+1,j}-p_{i,j}}{\rho_{i+\frac{1}{2},j}}-\frac{p_{i,j}-p_{i-1,j}}{\rho_{i-\frac{1}{2},j}}+\frac{p_{i,j+1}-p_{i,j}}{\rho_{i,j+\frac{1}{2}}}-\frac{p_{i,j}-p_{i,j-1}}{\rho_{i,j-\frac{1}{2}}} \tag{2-50}$$

and the discrete form of the right-hand part of Eq. (2-41) is

$$\nabla\cdot\boldsymbol{u}^{*}\approx U^{*}_{2}-U^{*}_{4}+U^{*}_{3}-U^{*}_{5} \tag{2-51}$$

For Staggered Grid 2 shown in Fig. 2-7(b), the discrete form of the left-hand part of Eq. (2-41) is

$$\nabla\cdot\left(\frac{\nabla p}{\rho}\right)\approx\sqrt{2}\left(\frac{p_{i+1,j+1}-p_{i,j}}{\sqrt{2}\rho_{i+\frac{1}{2},j+\frac{1}{2}}}-\frac{p_{i,j}-p_{i-1,j-1}}{\sqrt{2}\rho_{i-\frac{1}{2},j-\frac{1}{2}}}+\frac{p_{i+1,j-1}-p_{i,j}}{\sqrt{2}\rho_{i+\frac{1}{2},j-\frac{1}{2}}}-\frac{p_{i,j}-p_{i-1,j+1}}{\sqrt{2}\rho_{i-\frac{1}{2},j+\frac{1}{2}}}\right) \tag{2-52}$$

and the discrete form of the right-hand part of Eq. (2-41) in this grid is

$$\nabla\cdot\boldsymbol{u}^{*}\approx\sqrt{2}\left(U^{*}_{6}-U^{*}_{8}+U^{*}_{9}-U^{*}_{7}\right) \tag{2-53}$$

Thus, for Staggered Grid 1, the pressure at point (i, j) can be estimated based on the following:

$$p^{A}_{i,\mathrm{j}}=\frac{\sum_{A}\frac{p}{\rho}-\left(U^{*}_{2}-U^{*}_{4}+U^{*}_{3}-U^{*}_{5}\right)}{\frac{1}{\rho_2}+\frac{1}{\rho_4}+\frac{1}{\rho_3}+\frac{1}{\rho_5}} \tag{2-54}$$

For Staggered Grid 2, the pressure at point (i, j) is:

$$p^{B}_{i,j}=\frac{\sum_{B}\frac{p}{\rho}-\sqrt{2}\left(U^{*}_{6}-U^{*}_{8}+U^{*}_{9}-U^{*}_{7}\right)}{\frac{1}{\rho_6}+\frac{1}{\rho_7}+\frac{1}{\rho_8}+\frac{1}{\rho_9}} \tag{2-55}$$

Here,

$$\rho_2 = \frac{\rho_{i+1,j} + \rho_{i,j}}{2}, \rho_4 = \frac{\rho_{i-1,j} + \rho_{i,j}}{2}, \rho_3 = \frac{\rho_{i,j+1} + \rho_{i,j}}{2}, \rho_5 = \frac{\rho_{i,j-1} + \rho_{i,j}}{2} \quad \text{2-56}$$

$$U_2^* = \frac{u_{i,j}^* + u_{i+1,j}^*}{2}, U_3^* = \frac{v_{i,j}^* + v_{i,j+1}^*}{2}, U_4^* = \frac{u_{i-1,j}^* + u_{i,j}^*}{2}, U_5^* = \frac{v_{i,j-1}^* + v_{i,j}^*}{2} \quad \text{2-57}$$

$$\rho_6 = \frac{\rho_{i+1,j+1} + \rho_{i,j}}{2}, \ \rho_7 = \frac{\rho_{i-1,j+1} + \rho_{i,j}}{2},$$
$$\rho_8 = \frac{\rho_{i-1,j-1} + \rho_{i,j}}{2}, \ \rho_9 = \frac{\rho_{i+1,j-1} + \rho_{i,j}}{2} \quad \text{2-58}$$

$$U_6^* = \frac{\frac{u_{i,j}^* + v_{i,j}^*}{\sqrt{2}} + \frac{u_{i+1,j+1}^* + v_{i+1,j+1}^*}{\sqrt{2}}}{2}, U_7^* = \frac{\frac{u_{i,j}^* - v_{i,j}^*}{\sqrt{2}} + \frac{u_{i-1,j+1}^* - v_{i-1,j+1}^*}{\sqrt{2}}}{2},$$
$$U_8^* = \frac{\frac{u_{i,j}^* + v_{i,j}^*}{\sqrt{2}} + \frac{u_{i-1,j-1}^* + v_{i-1,j-1}^*}{\sqrt{2}}}{2}, U_9^* = \frac{\frac{u_{i,j}^* - v_{i,j}^*}{\sqrt{2}} + \frac{u_{i+1,j-1}^* - v_{i+1,j-1}^*}{\sqrt{2}}}{2} \quad \text{2-59}$$

$$\sum_B \frac{p}{\rho} = \frac{p_{i+1,j+1}}{\rho_6} + \frac{p_{i-1,j-1}}{\rho_7} + \frac{p_{i+1,j-1}}{\rho_9} + \frac{p_{i-1,j+1}}{\rho_8},$$
$$\sum_A \frac{p}{\rho} = \frac{p_{i+1,j}}{\rho_2} + \frac{p_{i-1,j}}{\rho_4} + \frac{p_{i,j+1}}{\rho_3} + \frac{p_{i,j-1}}{\rho_5} \quad \text{2-60}$$

The subscripts i and j represent the positions of the lattice points in the x and y directions.

Tabe et al. (2009)'s work proved the reliability and efficiency of Inamuro et al. (2004)'s model for two-phase flows with large density ratios when the associated Poisson equation is solved by the SOR method. Adopting Staggered Grid 1 in the discretization equation of the Poisson equation for the iterative SOR method means that only the velocity components along the orthogonal directions were taken into account. Correspondingly, adopting Staggered Grid 2, means that only the velocity components along the diagonal direction were considered. On the other hand, in the formulations (Eqs. (2-47) and (2-49)) adopted in the LBM scheme for solving the Poisson equation, the velocity components in all directions were considered, both in the diagonal and orthogonal directions. A possible way to increase the isotropy in the calculation process of the hydrodynamic pressure by the SOR method is to combine the velocity components from both of the two types of staggered grids together. The problem that arises, however, relates to the determination of the ratio for each type of staggered grid employed in the discretization equation of the

Poisson equation. As for the Poisson equation solved by the LBM scheme where the co-location grid is used, the weight ratio of velocity components used in the calculation along the diagonal and orthogonal directions was 1/9:1/36. A primary question that arises is whether the same ratio value would be suitable to be used (or not) in the discretization equation of the SOR method for blending velocity components from the two types of staggered grids. To investigate this question, the velocities in all directions are taken into consideration by blending the two kinds of staggered grids together. The variable α in the following equations is defined as the blending factor:

$$\alpha + (1-\alpha) = 1 \tag{2-61}$$

$$\alpha \cdot p_{i,j}^{A} + (1-\alpha) \cdot p_{i,j}^{B} = p_{i,j} \tag{2-62}$$

Combining equations Eq. (2-55) and Eq. (2-56), with some transformations, Eq. (2-62) can be rewritten as

$$p_{i,j} = \frac{\alpha\left(\sum_{A}\frac{p}{\rho} - U_{A}^{*}\right) + (1-\alpha)\left(\sum_{B}\frac{p}{\rho} - U_{B}^{*}\right)}{\alpha(\frac{1}{\rho_2}+\frac{1}{\rho_3}+\frac{1}{\rho_4}+\frac{1}{\rho_5}) + (1-\alpha)(\frac{1}{\rho_6}+\frac{1}{\rho_7}+\frac{1}{\rho_8}+\frac{1}{\rho_9})} \tag{2-63}$$

Here,

$$U_{A}^{*} = U^{*}{}_{2} - U^{*}{}_{4} + U^{*}{}_{3} - U^{*}{}_{5} \tag{2-64}$$

$$U_{B}^{*} = \sqrt{2}\left(U^{*}{}_{6} - U^{*}{}_{8} + U^{*}{}_{9} - U^{*}{}_{7}\right) \tag{2-65}$$

2.5 Initial conditions and parameters

Table 2-1 Two-phase parameters

$\rho_G[kg/m^3]$	1.1763
$\rho_L[kg/m^3]$	996.62
$\mu_G[Pa/s]$	$1.862*10^{-7}$

$\mu_L[Pa/s]$	$8.544*10^{-4}$
$\sigma[N/s]$	$7.288*10^{-2}$

Table 2-2 Model parameters

T	a	b	$\phi_{\max}$
0.035	1.0	6.7	0.09714
$\phi_{\min}$	ϕ_L	ϕ_G	κ_f
0.01134	0.092	0.015	0.5

To answer the questions arising from Chapter 1, a static water droplet in the quiescent gas phase is simulated with the Inamuro's model (Inamuro et al., 2004) with the parameters, schemes and algorithms adopted by Tabe et al. (2009); the parameters for the two-phase simulation are presented in Table 2-1 and Table 2-2. In the simulation, a water droplet is placed in the center of a gas channel, as shown in Fig. 2-8, here, the red region is the liquid water and the blue region is the gas. The left and right side boundaries are set as the inlet and outlet, respectively; the top and bottom of the domain are solid walls. The lattice nodes in the *x*, and *y* directions of the calculation domain and in the diameter direction of the liquid water droplet keep a constant proportion of 2.5:3.75:1, for all the simulations in this paper.

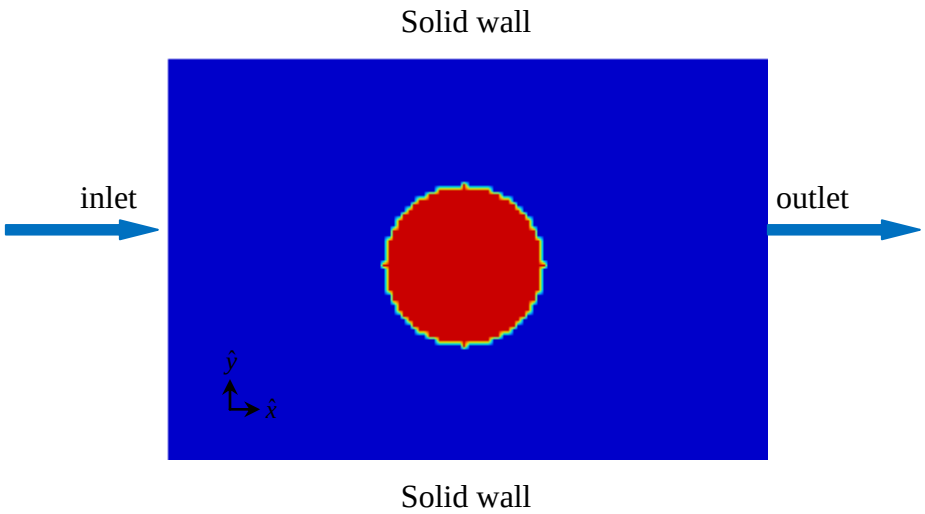

Fig. 2-8 Initial settings of the calculation domain

In the vicinity of the critical point, simplification of EOS can be made for the purpose of controlling the thickness of interface and the interface tension at equilibrium (Rowlinson and Wilom, 1989; Lee and Lin, 2005). The Cahn-Hilliard free energy was originally derived to describe the near-critical behavior of mixtures when the density gradients are small. However, gradually, this description works even when the density ratio

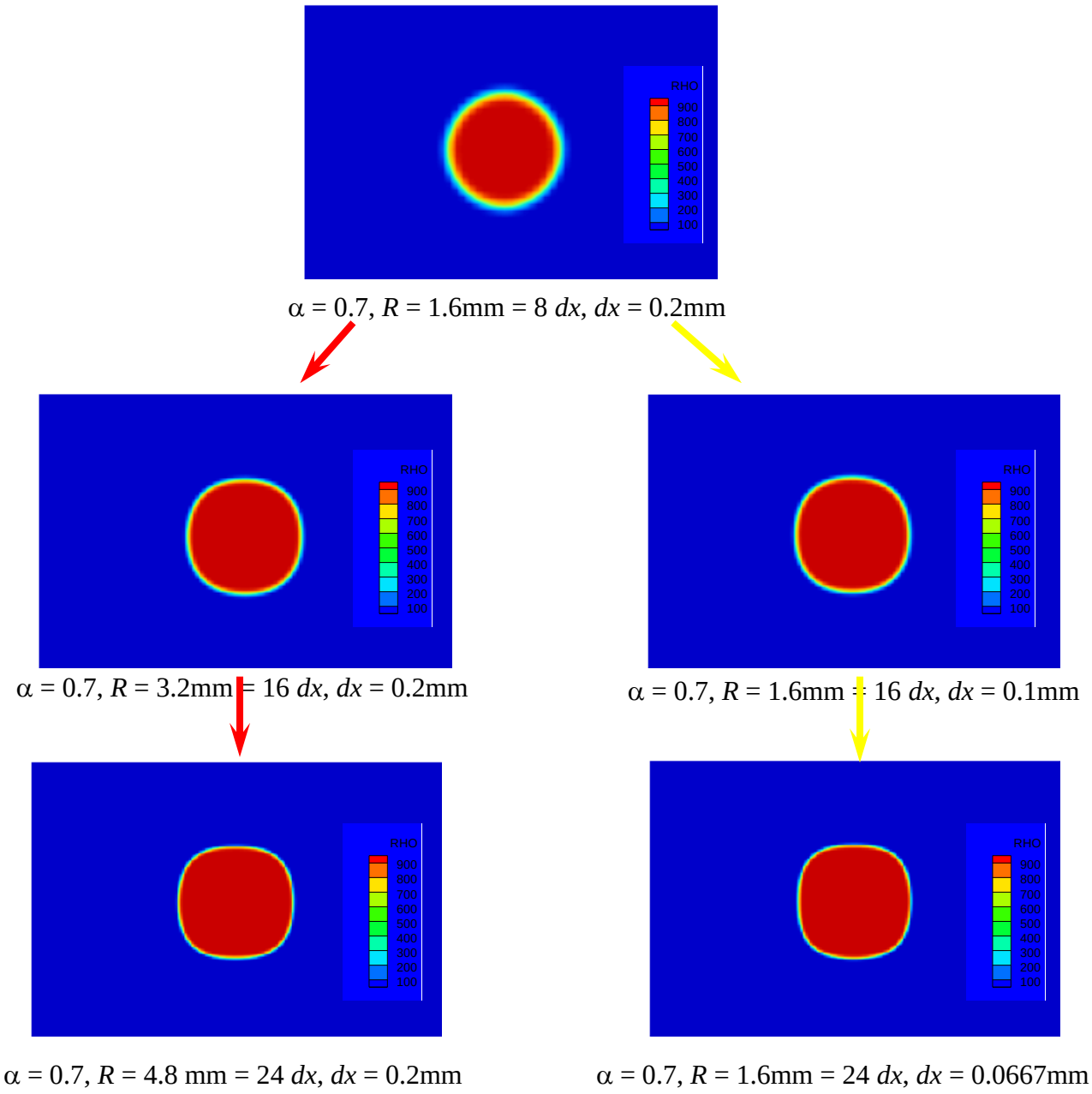

Fig. 2-9 Comparison of shape deformation tendency when maintaining the same grid thickness and physical radius at the same time step

became large (Lowengrub and Truskinovsky, 1998; Lee and Lin, 2005). In a plane interface at equilibrium, from the Eqs. (1-25) and (1-27), the constant parameter κ_g for the liquid water and gas two-phase system can be given by:

$$\kappa_g = \frac{3D}{2} \cdot \frac{\sigma}{\left(\rho_L^{sat} - \rho_G^{sat}\right)^2} \approx \frac{3D}{2} \cdot \frac{\sigma}{\rho_L^2} \qquad 2\text{-}66$$

As the density profile in the present model cannot be analytically given, and meanwhile the constant parameter κ_g which is tightly related to the profile can be analytically determined, neither. The parameter κ_g is given in the present model by adjusting the parameter *Rtig*, defined as:

$$\kappa_g = \approx \frac{3D}{2} \cdot \frac{\sigma}{\rho_L^2} \approx Rtig \cdot \frac{\sigma}{\rho_L^2} \qquad 2\text{-}67$$

The *Rtig* is arbitrarily chosen in the simulation, until the calculated pressure from the Poisson equation satisfies the pressure predicted by the Laplace equation, at which point, the corresponding Rtig is adopted in the simulation for the same density ratio. In this dissertation, following Tabe's group, *Rtig* = 0.33 is used in the present simulations.

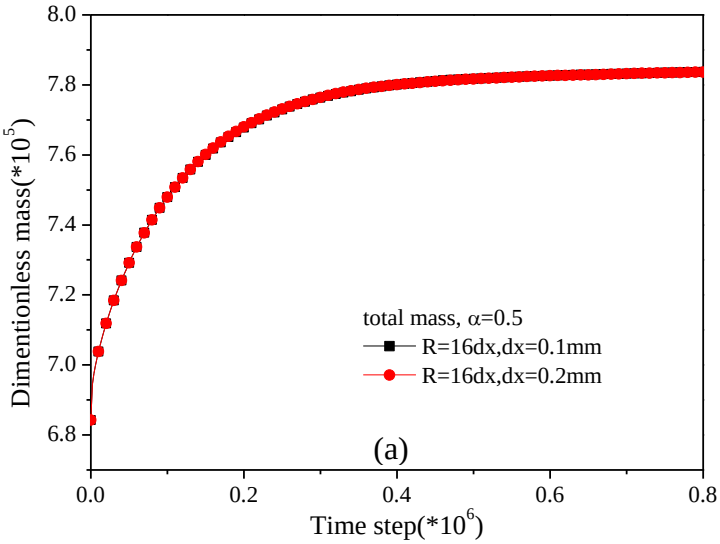

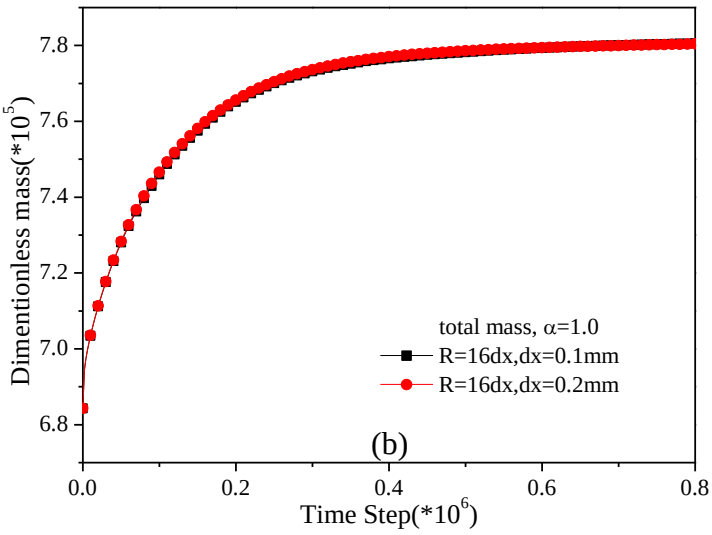

Fig. 2-10 Mass evolution history when different grid thicknesses are used

This dissertation mainly discusses the shape deformation and volume variation related problems of a water droplet in the numerical simulation. It is found that these numerical phenomena are not sensitive to the variations in the grid thickness, but sensitive to the dimensionless radius length, as shown in Fig. 2-9 and Fig. 2-10. Investigations of the simulation results in this dissertation mainly adopt the data from the same physical scale for abbreviation, except for the parts which require emphasis or special explanation. Furthermore, the characteristic particle speed in all the simulation is c = 200 m/s.

2.6 Conclusions

1 The thermodynamic meaning of the pressure calculated by the Poisson equation based fractional step method is the hydrodynamic pressure.

2 The shape deformation and volume variation problems occurred in the simulation are independent on the grid resolution.

3 Effects of the boundary conditions at inlet and outlet

In the LBM model, there are no definitions of the particle distribution functions outside the calculation domain, as illustrated in Fig. 3-1. It is necessary to set up the definitions or the treatments for the particle distribution functions on the lattice point at the boundaries after the streaming step.

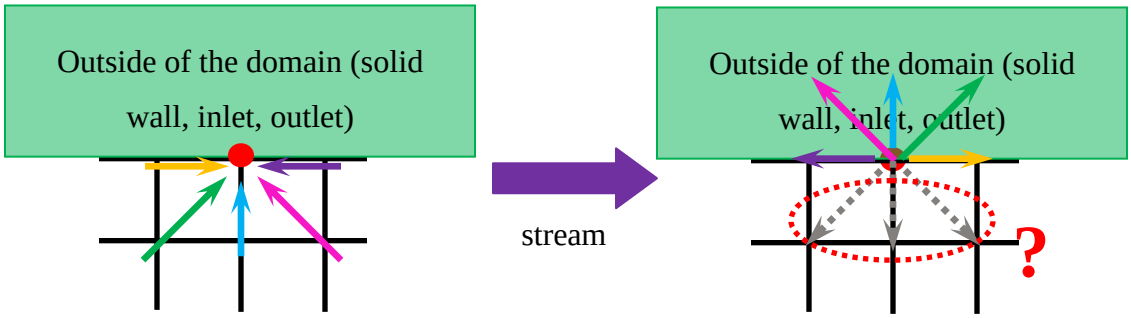

Fig. 3-1 Distribution functions on the boundaries

Unlike the LBM model for single phase flow, there is no direct relationship between the density and pressure of the fluid in the two-phase flow LBM model for large density ratio. Thus, the boundary conditions for density, velocity, and pressure have to be established respectively, at the solid wall, the inlet, and the outlet separately.

3.1 Boundary conditions for the solid wall

There have been several schemes proposed for the treatment of the particle distribution functions of the lattice nodes on the solid wall, including the simple bounce back scheme, and the equilibrium distribution assumption scheme. Following the illustrations described in the thesis of Lee (2009) and Sasaki(2011) , a brief introduction of the two types of boundary conditions for solid wall is made below.

The bounce back scheme is the simplest, which has been widely adopted in the LBM simulation with solid wall boundaries. The particle distribution functions coming to the lattice node at the solid wall from the surrounding fluid lattice nodes in the streaming step are directed assigned to the opposite directions of the lattice node at the solid wall, as illustrated by Fig. 3-2 and the following equations:

$$f_5 = f_3,\ f_8 = f_6,\ f_9 = f_7 \qquad 3\text{-}1$$

$$g_5 = g_3, g_8 = g_6, g_9 = g_7 \qquad 3\text{-}2$$

After the implementation of the bounce-back scheme, the corresponding density and the velocity can be acquired for the lattice node at the solid wall boundary with equations (2-30) and (2-31). With this scheme, although, the calculated velocity component vertical to the solid wall becomes 0, the velocity component parallel to the solid wall cannot do so, and so the non-slip boundary condition at the wall is broken. Moreover, it is difficult to represent the moving boundary with this scheme.

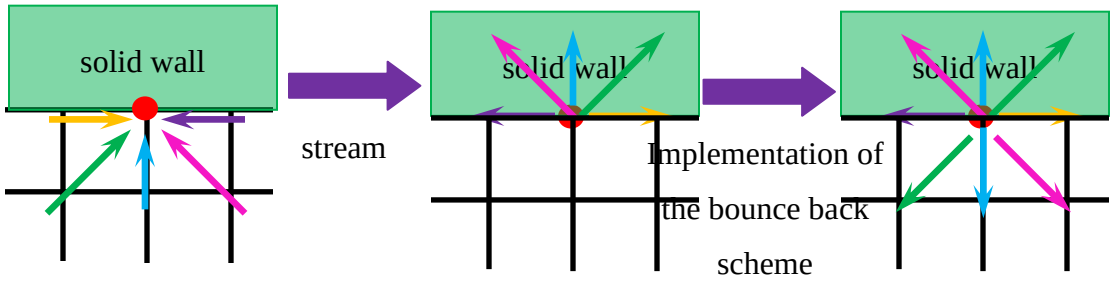

Fig. 3-2 The bounce back scheme

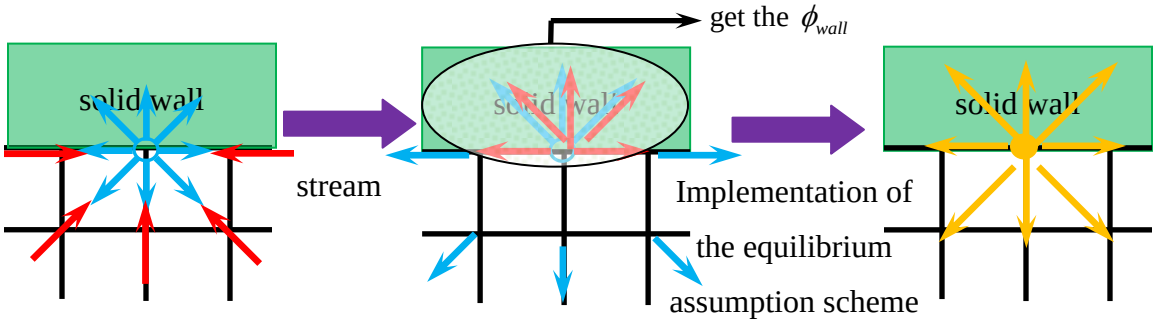

Fig. 3-3 The equilibrium distribution assumption scheme

In the equilibrium distribution assumption scheme, the fluid particles are assumed to reach the equilibrium state locally at the boundary of the solid wall, and such an equilibrium state can be described by Eqs. (2-32) and (2-33). As illustrated in Fig. 3-3, the particle distribution functions flowing outward to the outside of domain from the solid wall of a lattice node (i, j), remain in the same place and the same directions in the streaming process; meanwhile the particle distribution functions from the surrounding lattice nodes stream to boundary lattice node (i,j). The order parameter, ϕ_{wall} , of the lattice node (i, j) at the solid wall boundary can be calculated from the remaining distribution functions and the distribution function coming from the neighboring lattice nodes. With the ϕ_{wall} and the non-slip boundary assumption

at the solid wall boundary that velocity is 0, according the Eq.s (2-32), (2-38), and (2-33), the distribution functions, $f_i(\phi_{wall})$ and $g_i(\rho_{wall}, \boldsymbol{u})$, can be re-assigned. This process can be described by the following equations:

$$\phi_S = f_{s,1}^{*} + f_{s,3}^{*} + f_{s,6}^{*} + f_{s,7}^{*} + f_{s,2}^{t+\Delta t} + f_{s,3}^{t+\Delta t} + f_{s,4}^{t+\Delta t} + f_{s,6}^{t+\Delta t} + f_{s,7}^{t+\Delta t} \quad 3\text{-}3$$

$$f_{s,i} = f_i^{eq}(\phi_s, 0) \quad 3\text{-}4$$

$$g_{s,i} = g_i^{eq}(\rho_{wall}, 0) \quad 3\text{-}5$$

For the investigations addresses in this dissertation, as shown in Fig. 2-8 , the boundary conditions are realized for the macroscopic variables with such treatments as:

$$\begin{cases} \phi_{i,1} = \sum f_i \\ \boldsymbol{u}_{i,1} = 0 \end{cases} \text{ and } \begin{cases} \phi_{i,\mathrm{yd}} = \sum f_i \\ \boldsymbol{u}_{i,\mathrm{yd}} = 0 \end{cases} \quad 3\text{-}6$$

Besides, the pressure boundary condition here is set as 0-gradient boundary condition:

$$\frac{\partial p}{\partial x_\alpha} = 0 \quad 3\text{-}7$$

Unlike in the bounce back scheme, the macroscopic variables $\boldsymbol{u}, \phi, \rho$ are calculated before the implementation of the wall boundary scheme. Also, the application of the equilibrium distribution assumption scheme requires more computational resources than the bounce back scheme. However, with the adoption of this equilibrium scheme, the macroscopic flow field can be appropriately described, and the zero-velocity at the wall can be ensured; furthermore, the moving wall boundary and the step-wise wall boundary can be implemented with this scheme. More importantly, from the evolution history illustrated in Fig. 3-3, no source term is added to the flow field, nor, there is any mass exchange with outside in the simulation with the equilibrium distribution assumption scheme.

3.2 Velocity inlet and free-out outlet boundary condition

The velocity inlet and the free-out outlet boundary conditions are commonly adopted in the numerical simulation, which physically corresponds to the pressure-constant boundary condition. Such inlet and outlet boundary conditions have been adopted by Tabe et al. (2009), Ben Salah et al. (2012), and Moriyama and Inamuro (2010), in their simulations of two-phase flows in the PEFC. For the shape deformation and volume variation problems discussed in this dissertation, this type of boundary condition

is implemented with the inlet velocity set to 0. Following the initial settings introduced in Chapter 2, as illustrated in Fig. 3-4, the boundary conditions of the macroscopic variables at the inlet and outlet are established as the following equations:

For the inlet ,

$$\begin{cases} \phi_{1,j} = \phi_{G0} \\ \boldsymbol{u}_{1,j} = 0.0 \\ \nabla \cdot p_{1,j} = 0, (p_{1,j} = p_{2,j}) \end{cases} \quad 3\text{-}8$$

and for the outlet:

$$\begin{cases} \phi_{xd,j} = \sum f_i \\ \nabla \cdot \boldsymbol{u} = 0, \ (\boldsymbol{u}_{xd,j} = \boldsymbol{u}_{xd-1,j}) \\ p_{xd,j} = 0 \end{cases} \quad 3\text{-}9$$

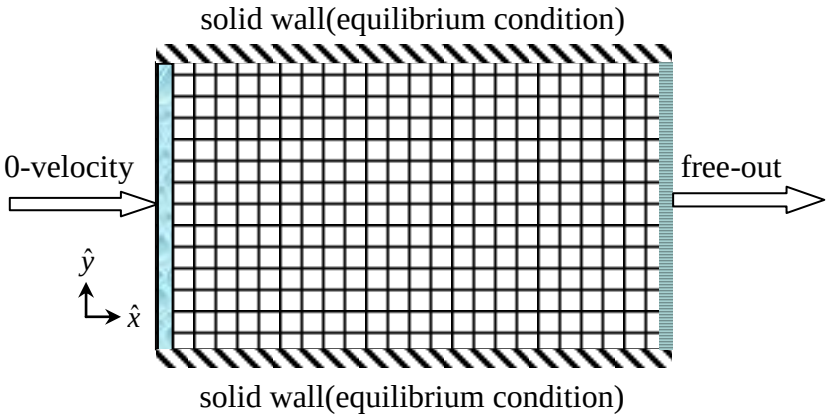

Fig. 3-4 Velocity inlet and free-out outlet boundary conditions in the simulation

For the zero velocity inlet boundary, the treatment of f_i is illustrated in Fig. 3-5. Similar to the solid wall boundary treatment, there is no f_i^* from outside transported to the inlet lattice points, and the $f_{In,i}^*$ along the outside direction at the inlet points keep their values in the transport process:

$$\phi_{In} = f_{in,1}^* + f_{in,4}^* + f_{in,7}^* + f_{in,8}^* + f_{in,3}^{t+\Delta t} + f_{in,4}^{t+\Delta t} + f_{in,5}^{t+\Delta t} + f_{in,7}^{t+\Delta t} + f_{in,8}^{t+\Delta t} \quad 3\text{-}10$$

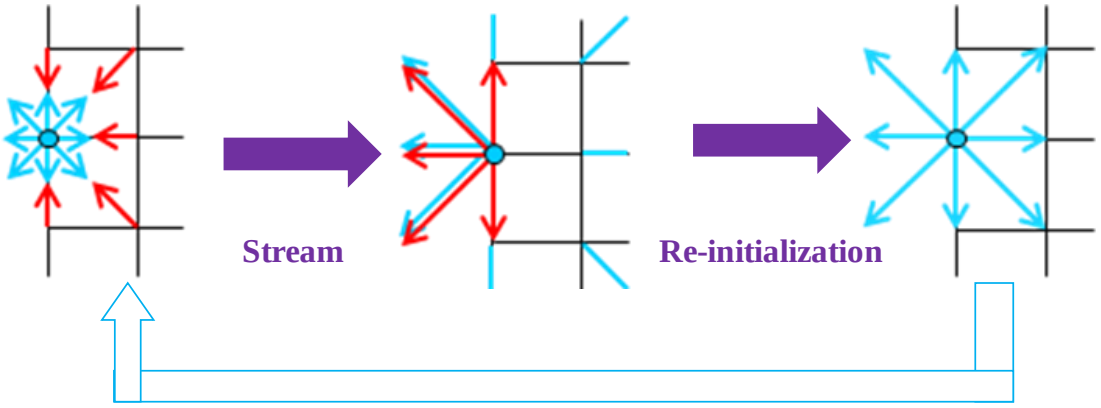

Fig. 3-5 Distribution function treatments in the velocity inlet boundary condition (the re-initialization scheme)

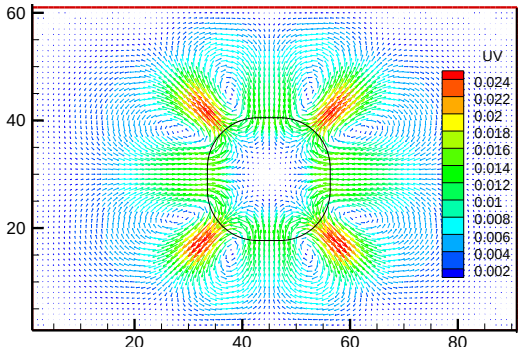

Fig. 3-6 Example of the spurious velocity distribution in the simulation

In the collision process, the constant value of ϕ_{In} is used at the inlet points, as described in Eq. (3-8), thus leading to

$$f_{in,i} = f_i^{eq}(\phi_{G0}, 0) = f_{\text{in},i}^{*} \tag{3-11}$$

and,

$$\sum_{i=1}^{9} f_{in,i} = \sum_{i=1}^{9} f_i^{eq}(\phi_{in}, 0) = \phi_{G0} \tag{3-12}$$

Comparing Eqs. (3-11) and (3-12), it is easy to found that:

$$f_{in,3}^{t+\Delta t} + f_{in,4}^{t+\Delta t} + f_{in,5}^{t+\Delta t} + f_{in,7}^{t+\Delta t} + f_{in,8}^{t+\Delta t} \neq f_{in,3}^{*} + f_{in,4}^{*} + f_{in,5}^{*} + f_{in,7}^{*} + f_{in,8}^{*} \tag{3-13}$$

Because f_i is a function of ϕ and $\boldsymbol{u}$,in the simulation due to the existence of spurious velocity field, as shown in Fig. 3-6, and ϕ is different in the inlet and its surrounding lattice points with fluid, that further leads to:

$$\phi_{G0} - \phi_{in} \neq 0 \qquad 3\text{-}14$$

From Eq. (3-14), it is found that the inlet boundary setting of f_i^* may be a source of the non-conservation of mass in the simulation.

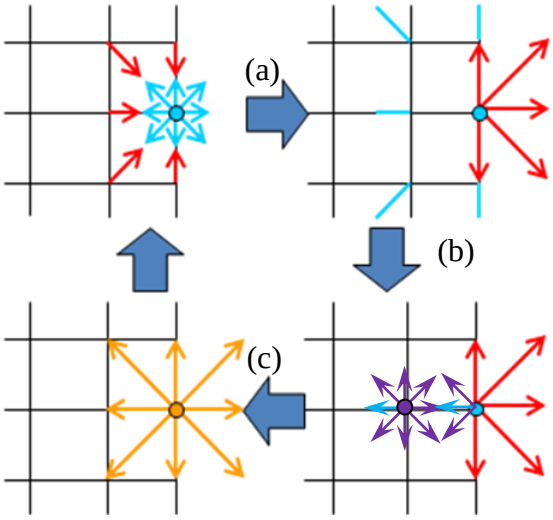

Fig. 3-7 Distribution function treatments in the free-out outlet boundary condition

The treatment of f_i in the free-out outlet boundary condition is illustrated in Fig. 3-7. A modification process was added to the calculation steps of the f_i after the transport process but before the collision process. In the transport process, f_{outlet}^* along the outlet direction transport outside the calculation domain, f_{outlet}^* along the inner side of the outlet transport to the inner fluid point; and meanwhile the $f_{outlet-1}^*$ or f_{xd-1}^* at the inner points along the outlet directions update the $f_{outlet}^{t+\Delta t}$ along the outside direction. As there are no $f_{outlet+1}^*$ or f_{xd+1}^* to update the $f_{outlet}^{t+\Delta t}$ along the inner direction, as shown in the modification process, the $f_{outlet-1}^{t+\Delta t}$ or $f_{xd-1}^{t+\Delta t}$ along the inner direction are used to update the inner direction $f_{outlet}^{t+\Delta t}$. Such treatment may also introduce a source of mass non-conservation. In the transport process, the ϕ loss due to the f_{outlet}^* transport to the outside is given by:

$$\phi_{outlet,loss} = f_{outlet,2}^* + f_{outlet,6}^* + f_{outlet,9}^* \qquad 3\text{-}15$$

and the ϕ supplement from the inner lattice points to the outside direction of the outlet point is:

$$\phi_{outlet,supp} = f_{outlet,2}^{t+\Delta t} + f_{outlet,6}^{t+\Delta t} + f_{outlet,9}^{t+\Delta t} \quad 3\text{-}16$$

Because ϕ and $\boldsymbol{u}$ in the outlet point and the inner point next to the outlet are different, thus

$$f_{outlet,2}^{*} \neq f_{\text{outlet},2}^{t+\Delta t},\ f_{outlet,6}^{*} \neq f_{outlet,6}^{t+\Delta t},\ f_{outlet,9}^{*} \neq f_{outlet,9}^{t+\Delta t} \quad 3\text{-}17$$

and,

$$\phi_{outlet,loss} \neq \phi_{outlet,supp}\ ; \quad 3\text{-}18$$

Furthermore, for all lattice nodes along the outlet,

$$\sum_{outlet} \phi_{outlet,loss} \neq \sum_{outlet} \phi_{outlet,supp}\ ; \quad 3\text{-}19$$

The ϕ at each outlet point moving to the inner points is

$$\phi_{move} = f_{outlet,4}^{*} + f_{outlet,7}^{*} + f_{outlet,8}^{*} = f_{xd\text{-}1,4}^{t+\Delta t} + f_{xd\text{-}1,7}^{t+\Delta t} + f_{xd\text{-}1,8}^{t+\Delta t} \quad 3\text{-}20$$

and its total value is:

$$\sum_{outlet} \phi_{move} = \sum_{outlet} f_{outlet,4}^{*} + \sum_{outlet} f_{outlet,7}^{*} + \sum_{outlet} f_{outlet,8}^{*} = \sum_{xd-1} f_{xd\text{-}1,4}^{t+\Delta t} + \sum_{xd-1} f_{xd\text{-}1,7}^{t+\Delta t} + \sum_{xd-1} f_{xd\text{-}1,8}^{t+\Delta t} \quad 3\text{-}21$$

In the modification process, the same amount of ϕ is supplemented to the outlet points, as the $f_{xd-1}^{t+\Delta t}$ along the inner direction is given to $f_{xd}^{t+\Delta t}$ along the inner direction. In the collision process, with the same treatment as did in the solid wall boundary condition, there is also no source of mass introduced and the total ϕ at the outlet points keep constant.

In a summary, both the velocity inlet and the free-out outlet may induce mass non-conservation problems; for the velocity inlet, the problem may arise from the numerical treatment; and for the free-out outlet, it may comes from the mass exchange with the outside of the computational domain, due to the existence of the spurious velocity field.

3.3 Periodic boundary condition for the inlet and outlet

The periodic boundary condition, which physically corresponds to the volume constant boundary condition, is also commonly adopted in the numerical simulation; particularly, in theoretical analysis, because of its easy implementation. The distribution function f_i flowing outward from the computational domain at the inlet or outlet with the periodic boundary condition will flow into the computational domain from the other side, as illustrated in Fig. 3-8 and Fig. 3-9. It can be found that the periodic boundary conditions can be viewed as a circular belt.

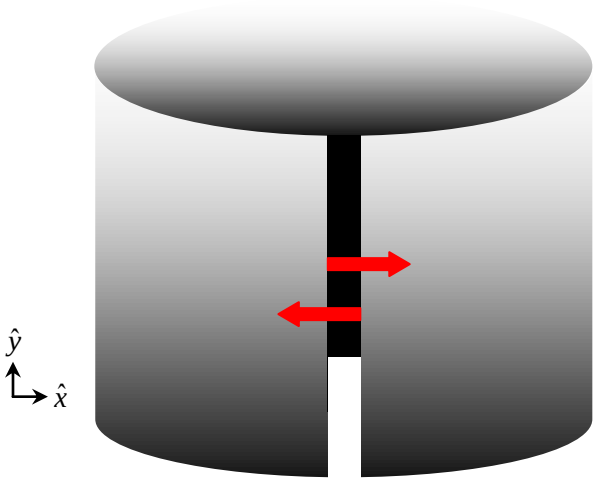

Fig. 3-8 Schematic of the periodic boundary condition along *x* direction

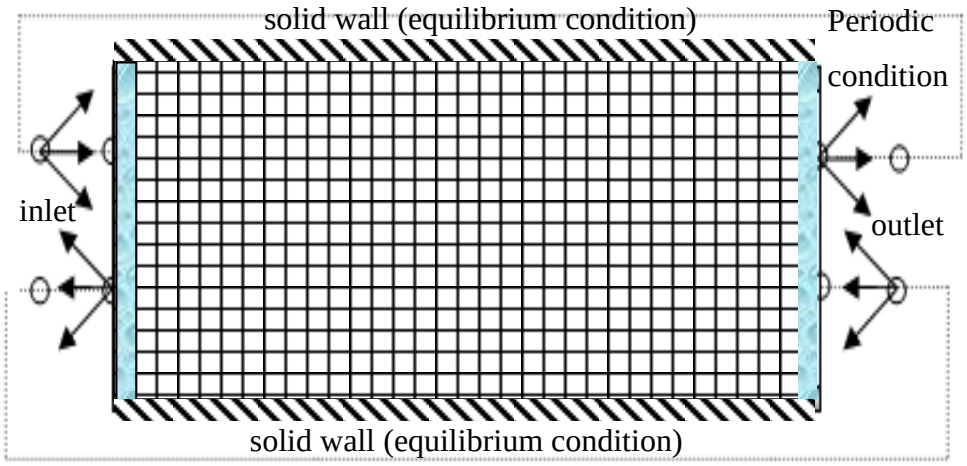

Fig. 3-9 Periodic boundary conditions adopted in the simulation

The detailed treatments of the macroscopic variables are similar to the treatment of the inner fluid points. For the inlet points, they are:

$$\begin{cases} \phi_{1,j} = f^{*}_{inlet,1} + f^{*}_{\text{outlet},2} + f^{*}_{\text{outlet},6} + f^{*}_{\text{outlet},9} \\ \qquad + f^{t+\Delta t}_{\text{inlet},3} + f^{t+\Delta t}_{\text{inlet},4} + f^{t+\Delta t}_{\text{inlet},5} + f^{t+\Delta t}_{\text{inlet},7} + f^{t+\Delta t}_{\text{inlet},8} \\ \boldsymbol{u}_{1,j} = g^{*}_{inlet,1} + g^{*}_{\text{outlet},2} + g^{*}_{\text{outlet},6} + g^{*}_{\text{outlet},9} \\ \qquad + g^{t+\Delta t}_{\text{inlet},3} + g^{t+\Delta t}_{\text{inlet},4} + g^{t+\Delta t}_{\text{inlet},5} + g^{t+\Delta t}_{\text{inlet},7} + g^{t+\Delta t}_{\text{inlet},8} \\ \nabla \cdot p = 0, (p_{1,j} = p_{xd,j}) \end{cases} \tag{3-22}$$

and for the outlet points, they are:

$$\begin{cases} \phi_{\text{outlet},j} = f^{*}_{\text{xd},1} + f^{t+\Delta t}_{\text{xd},2} + f^{t+\Delta t}_{\text{xd},3} + f^{t+\Delta t}_{\text{xd},5} \\ \qquad + f^{*}_{\text{inlet},4} + f^{*}_{\text{inlet},7} + f^{*}_{\text{inlet},8} + f^{t+\Delta t}_{\text{xd},9} \\ \boldsymbol{u}_{\text{outlet},j} = g^{*}_{\text{xd},1} + g^{t+\Delta t}_{\text{xd},2} + g^{t+\Delta t}_{\text{xd},3} + g^{t+\Delta t}_{\text{xd},5} \\ \qquad + g^{*}_{\text{inlet},4} + g^{*}_{\text{inlet},7} + g^{*}_{\text{inlet},8} + g^{t+\Delta t}_{\text{xd},9} \\ \nabla \cdot p = 0, (p_{xd,j} = p_{1,j}) \end{cases} \tag{3-23}$$

Because the periodic boundary condition is a type of volume-constant boundary condition, thus, theoretically speaking, there is no mass exchange with outside of the computational domain.

3.4 Simulation results and discussions

Some non-physical results are observed in the simulation of a static water droplet in the quiescent gas channel under the 0-velocity inlet/free-out outlet boundary conditions, such as mass non-conservation, droplet volume variation, and shape oscillation. Fig. 3-10 shows examples of the order parameter evolution histories of the two-phase system with different droplet radii and different blending factor α. Fig. 3-11 shows the corresponding evolution histories of the mass. From the two figures, it can be seen that the simulation can be divided into two stages: the initial stage, in which both the mass and the order parameters in the gas and liquid phases are changing to form the appropriate interface between the two phases; and the steady stage, wherein the mass or the order parameter in both phases or in one phase keep constant. A more detailed description of the evolution of the interface will be given in the next chapter. The total order parameter and the total mass of the two-phase system are continuously increasing, no matter which radius length nor which blending factor α are adopted in the simulation. The order parameter, ϕ , and the mass in the liquid phase keep increasing all the times, and the increasing speed is

rapid in the very beginning part of time and in the latter remain a constant increasing speed. Conversely, with the exception of the very initial stage, the order parameter ϕ and the mass in the gas phase keep constant. In the same time period, the volumes of the droplets are found to be expanding, Fig. 3-12 shows the volume variations of the droplet with a radius of 6 *dx* under typical blending factors. Besides, during this period, the shapes of the droplets are also observed to be oscillating periodically, Fig. 3-13 shows the shape

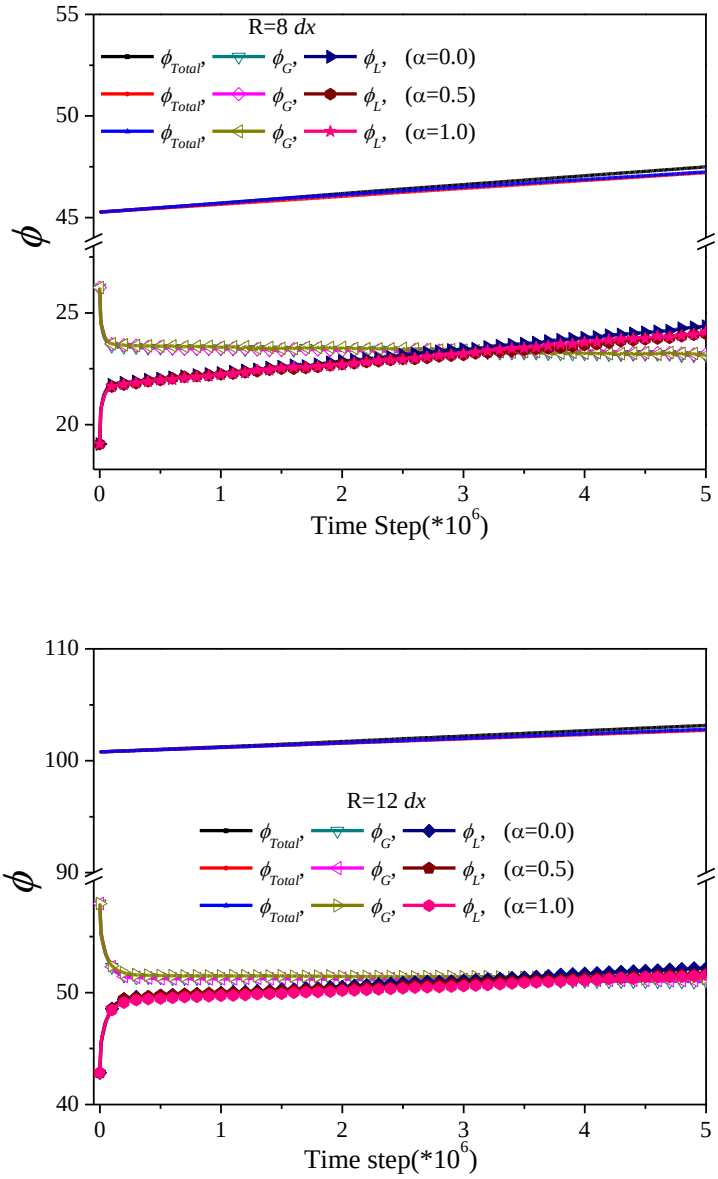

Fig. 3-10 Examples of the order parameter evolution histories

oscillation types of the droplet observed in the simulation when the droplet radius is 12 *dx* and the blending factors are 0.0, 0.5, and 1.0. Such types of shape oscillation are consistent with observations of the natural oscillations of a spherical water droplet (Pruppacher and Klett, 2004), as shown in Fig. 3-15; though the oscillation frequencies have not been captured by the present simulation, which may come from the limited resolutions in space and time. Although shape deformations coming from the oscillation exist, the shape of the simulated water droplet remains almost constant. Fig. 3-15 shows

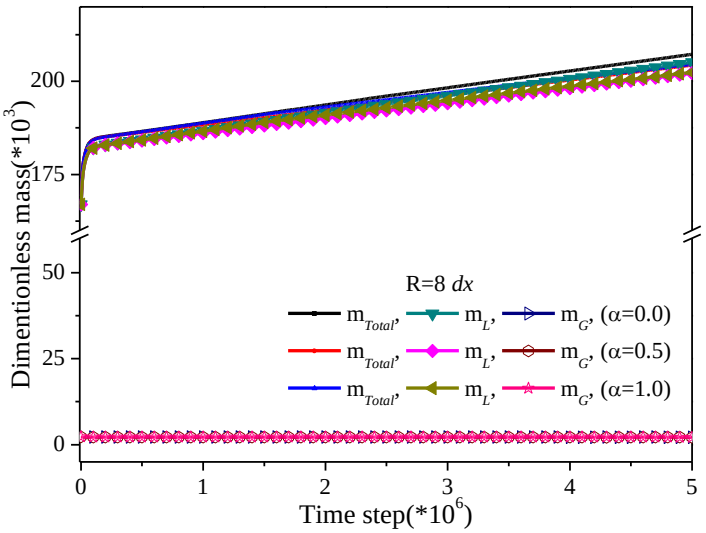

(a) evolution histories of the order parameter when the radius is 8 *dx*

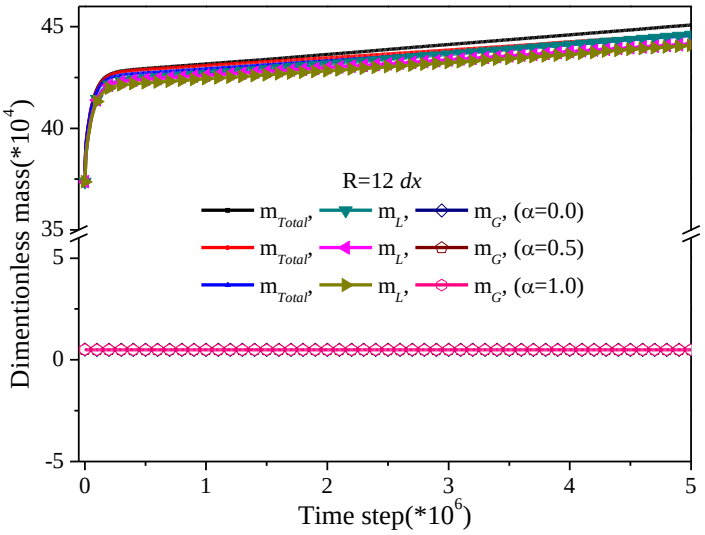

(b) evolution histories of the order parameter when the radius is 12 *dx*

Fig. 3-11 Examples of the mass evolution histories under velocity inlet and free-out outlet boundary conditions

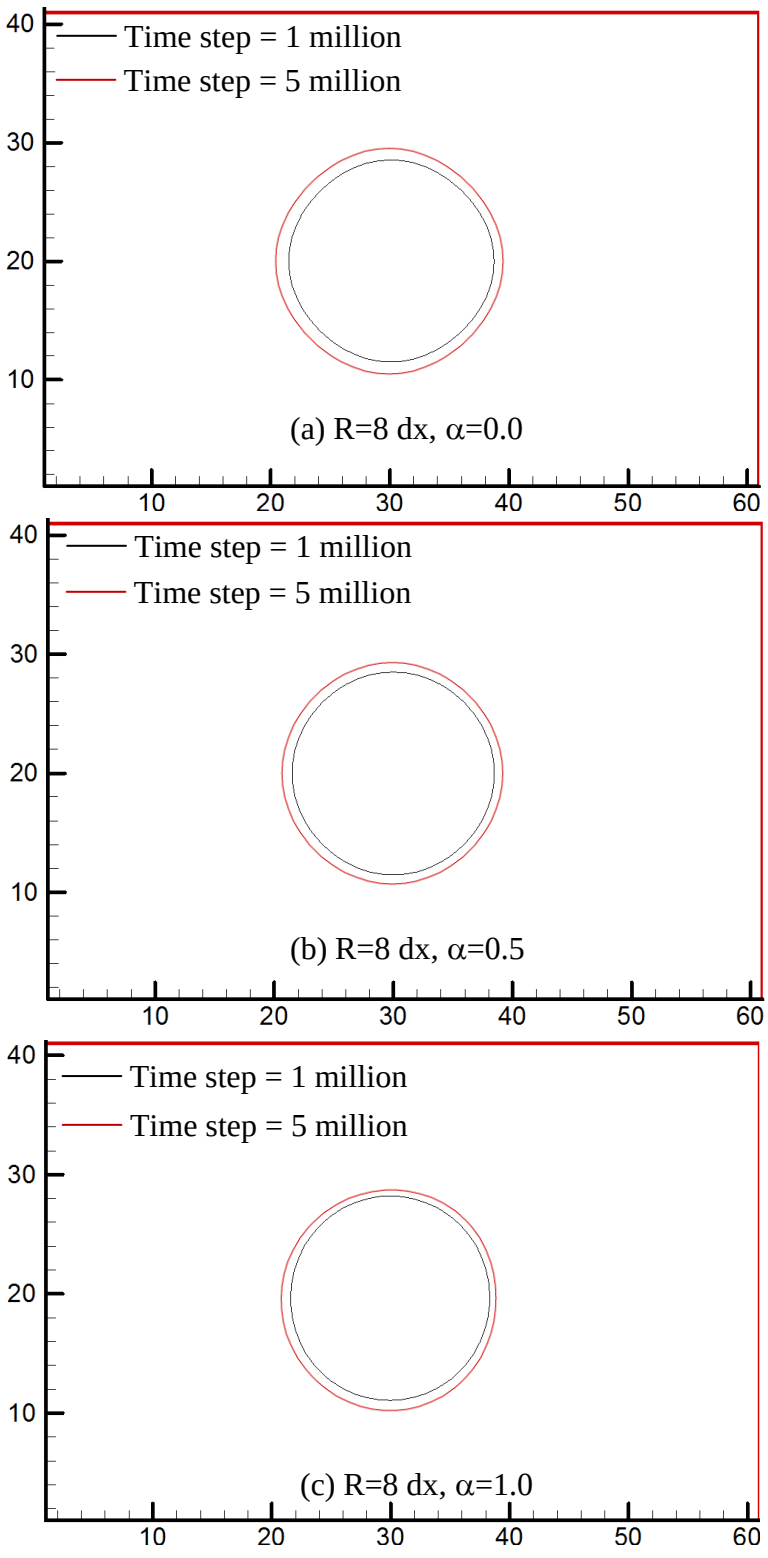

Fig. 3-12 Examples of volume expansion in the steady stage

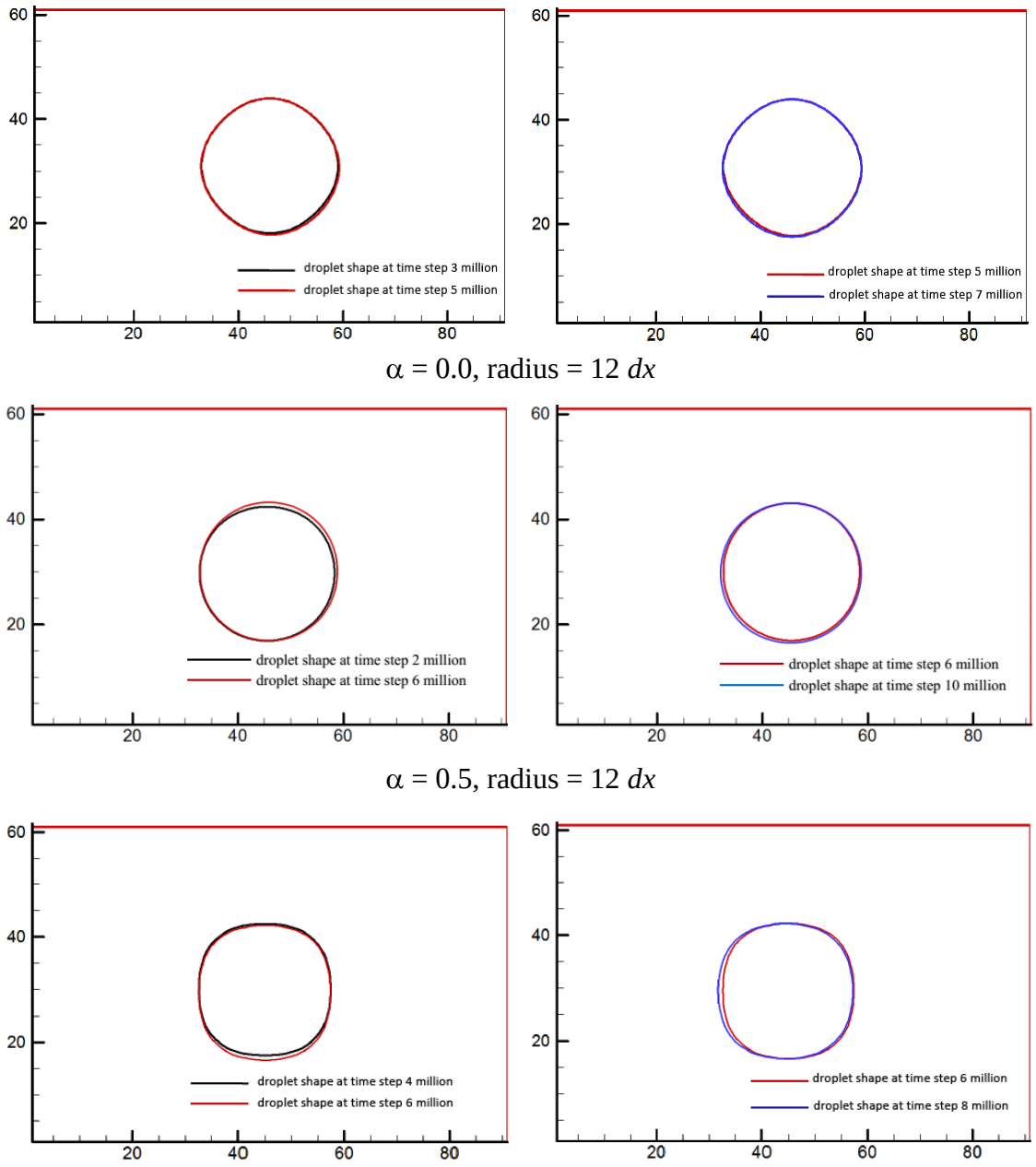

Fig. 3-13 Typical shape oscillation types in the simulation under the 0-velocity inlet and free-out outlet boundary conditions

the contours of the simulated water droplet, corresponding to those in Fig. 3-13, but with more time steps in the smooth mass-increment stage (the stage shown in Fig. 3-14, other than the very initial part) and with their droplet centers artificially aligned at the same point; in these cases, very little difference in the

shape is observed, except for the volume expansion of the water droplet caused by the continuous constant mass increment at the water–air interface.

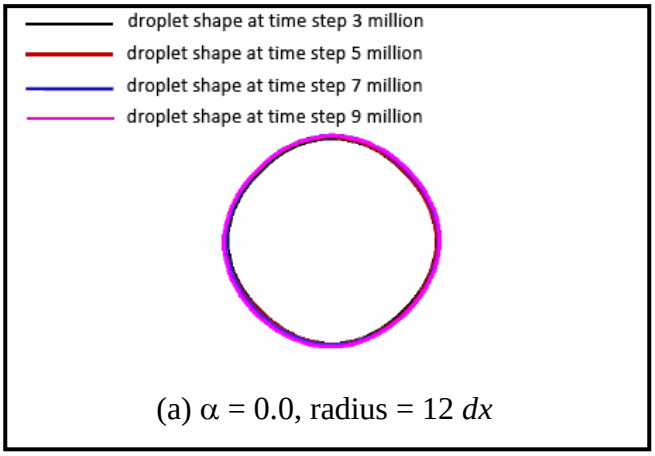

(a) α = 0.0, radius = 12 *dx*

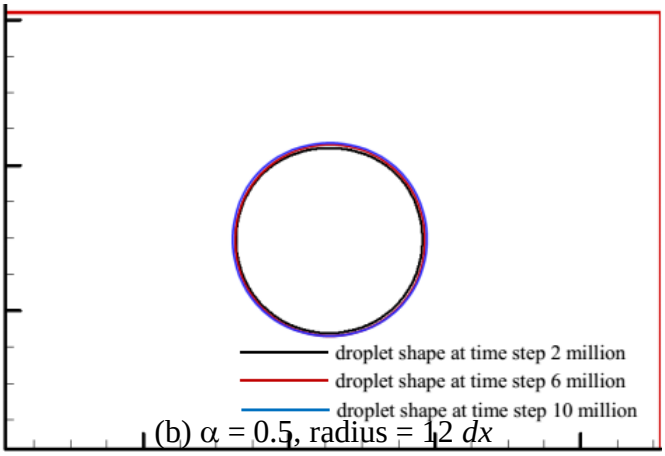

(b) α = 0.5, radius = 12 *dx*

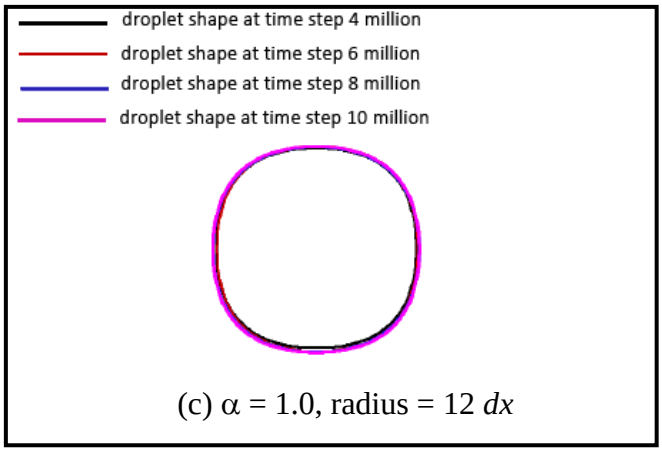

(c) α = 1.0, radius = 12 *dx*

Fig. 3-15 Shapes of droplet with their centers at the same point in the simulation

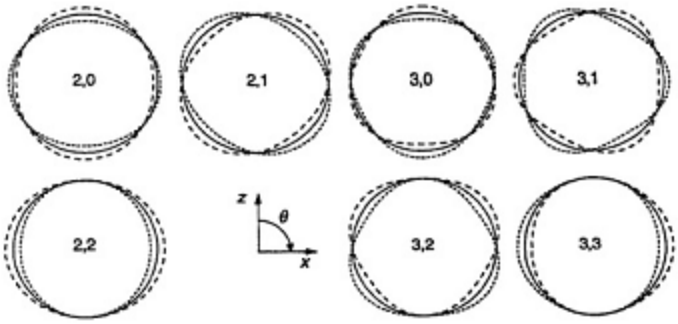

Fig. 3-16 Natural oscillation types of a spherical droplet (Pruppacher and Klett, 2004**)**

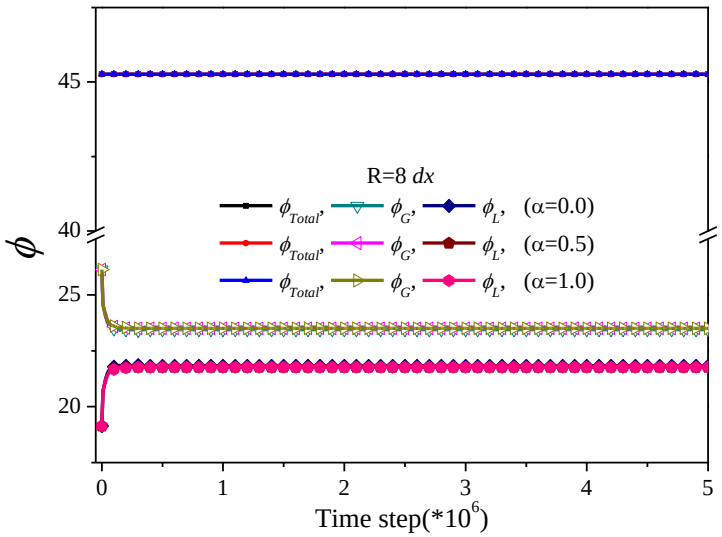

(a) evolution histories of the order parameter when the radius is 8 *dx*

For the simulations with the periodic boundary condition adopted at the inlet and outlet, it is found that there is no increase in the total order parameter for the two-phase flow; nor is there an increase in the liquid phase order parameter after the initial stage as compared with the 0-velocity inlet and free-out outlet boundary conditions. Fig. 3-17shows the order parameter evolution histories in the simulation with typical blending factors of 0.0, 0.5 and 1.0 and with initial droplet radius of 8 dx and 12 dx. Fig. 3-18 is the corresponding mass evolution histories of the two-phase systems. From these figures, we can conclude that the mass non-conservation problem encountered in the simulation under the velocity inlet and free-out outlet boundary conditions comes from the use of such boundary conditions themselves,

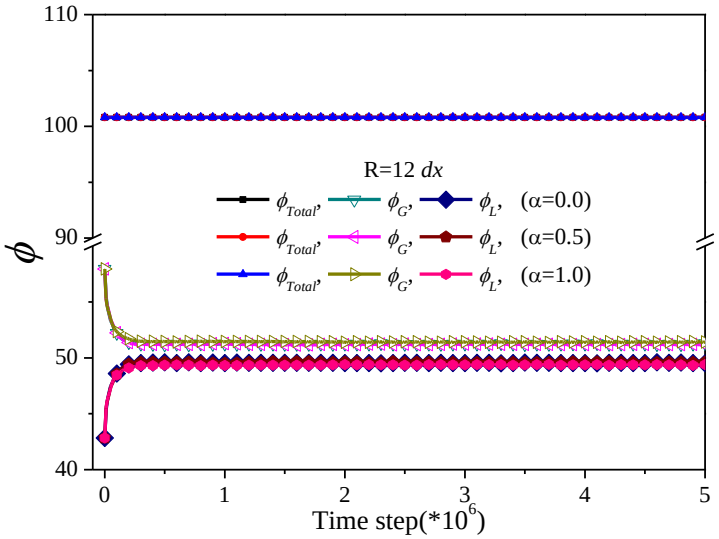

(b) evolution histories of the order parameter when the radius is 12 *dx*

Fig. 3-17 The order parameter evolution histories under periodic boundary condition

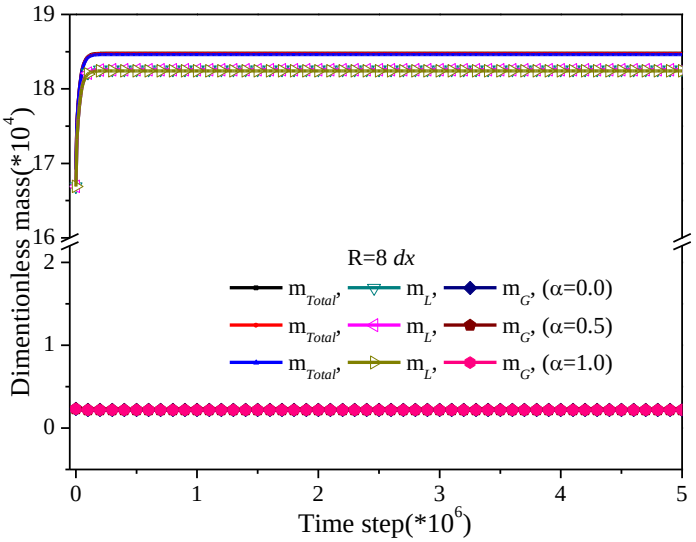

(a) evolution histories of the mass when the radius is 8 *dx*

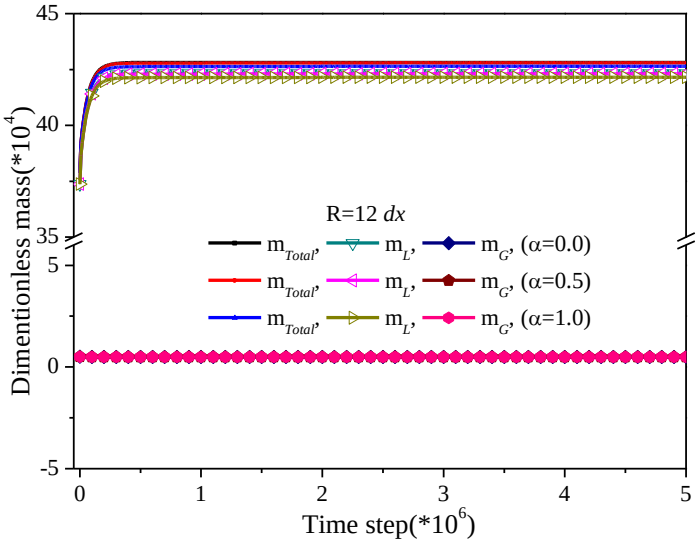

(b) evolution histories of mass when the radius is 12 *dx*

Fig. 3-18 Mass evolution histories under the periodic boundary condition

and that the mass increase in the liquid phase arises from the inlet and outlet boundaries. Such a mass increase can be removed by adopting the periodic boundary condition. These simulation results also prove that the free-energy-based two-phase LBM model for large density ratio adopted in present investigation satisfies the mass conservation law.

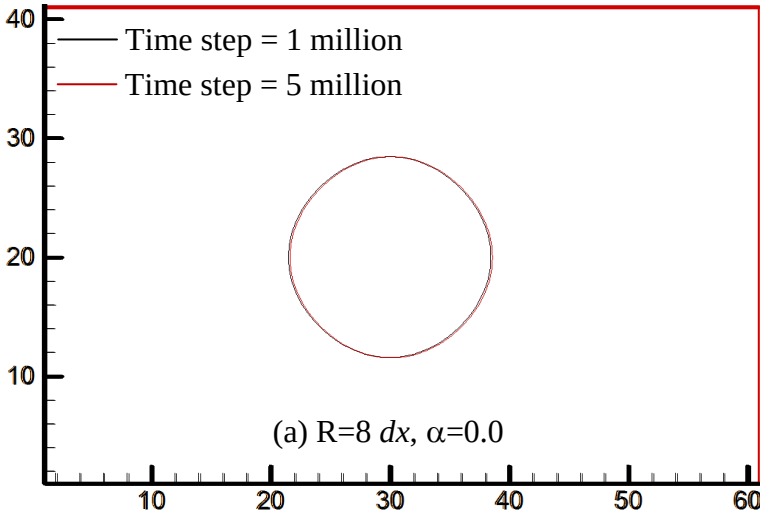

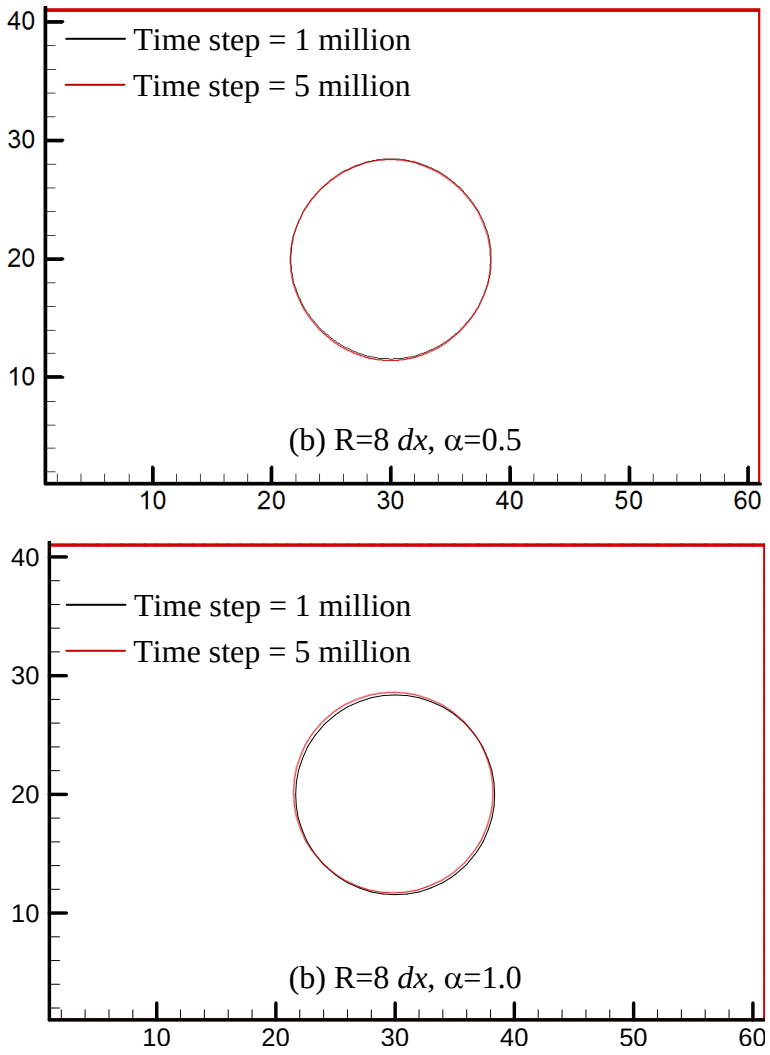

Fig. 3-19 Contours of the droplet under periodic boundary condition with a radius of 8 *dx*

Under the periodic boundary condition, there are also neither volume changes, nor shape oscillations in the simulation after the initial stage. Fig. 3-19, and Fig. 3-20 illustrate the volume and shape variations of the droplet when its radius is 8 *dx* and 12 *dx* (respectively) with the periodic boundary condition at the inlet and outlet in the steady stage, which corresponds to the cases in Figs. 3-13, 3-14 and 3-15 when the 0-velocity inlet and the free-out outlet boundary conditions are adopted. From these figures, it can be proved that the volume expansions and shape oscillations in the steady state under the 0-velocity inlet and free-out outlet boundary conditions come from the application of such boundary conditions themselves. The mass exchange or the so-called order parameter exchange at the inlet and outlet boundary is the source of volume variation and shape oscillation; these numerical phenomena can be removed by the use of the periodic boundary condition.

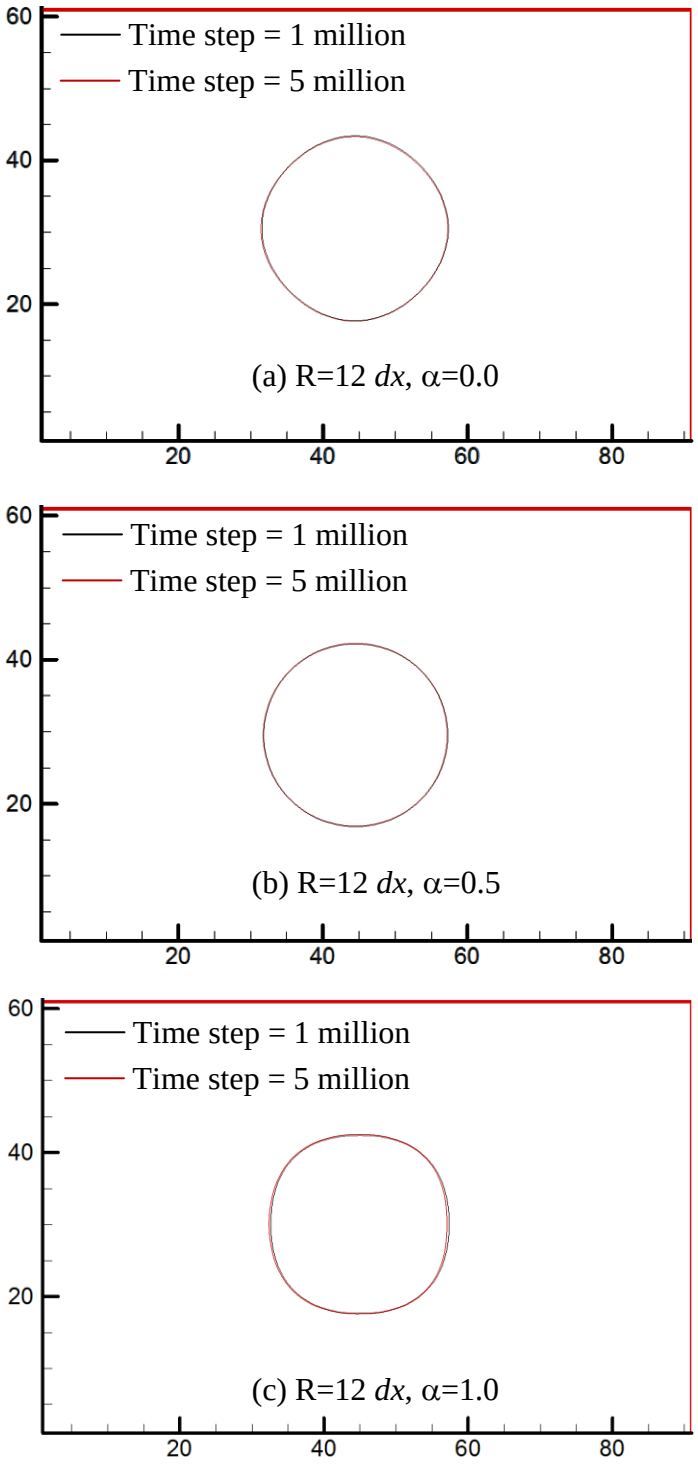

Fig. 3-20 Contours of the droplet under the periodic boundary condition with a radius of 12 *dx*

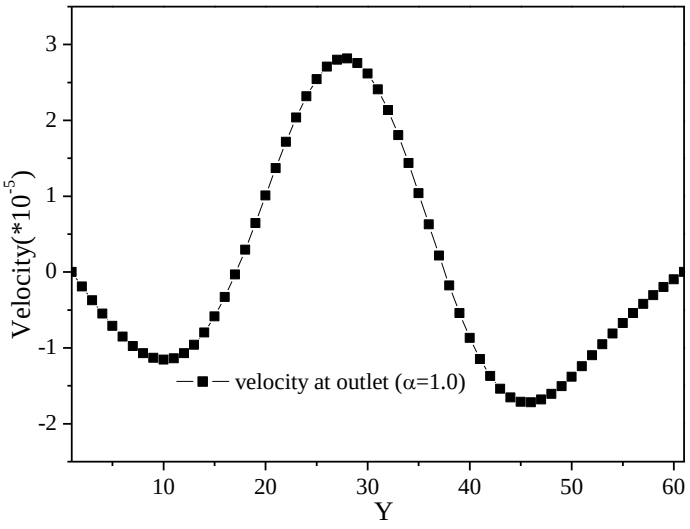

Fig. 3-21 Example of dimensionless velocity distribution at the outlet under the free-out boundary condition

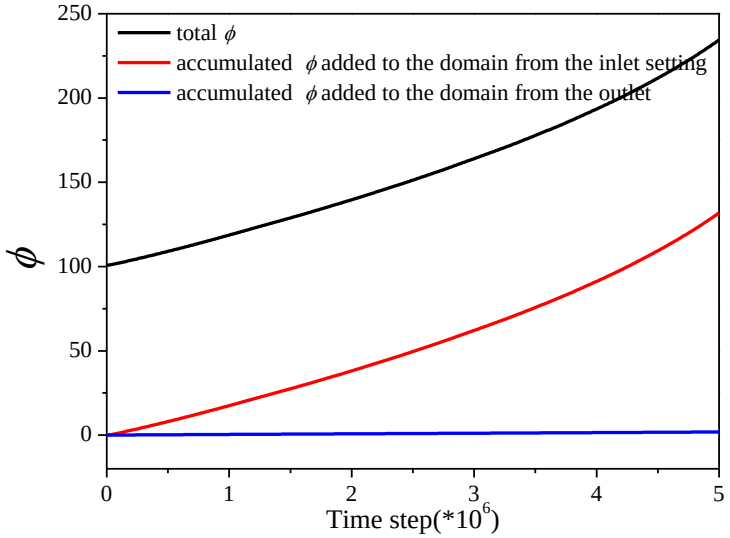

Fig. 3-22 Example of the order parameter evolution histories

As discussed in section 3.2, physically the free-out outlet allows mass to be exchanged with the outside of the computational domain due to the existence of velocity; the numerical treatment at the velocity inlet may also add new mass to the two-phase system. Fig. 3-21 shows the velocity distribution at the outlet

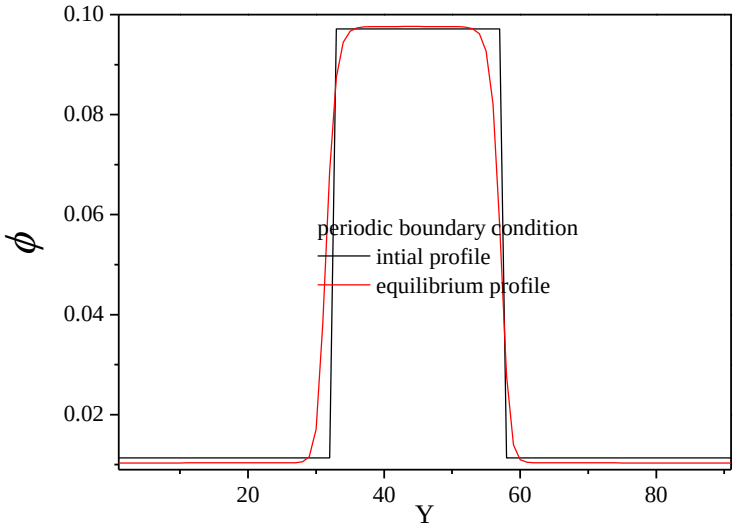

(a) profiles under the periodic boundary condition

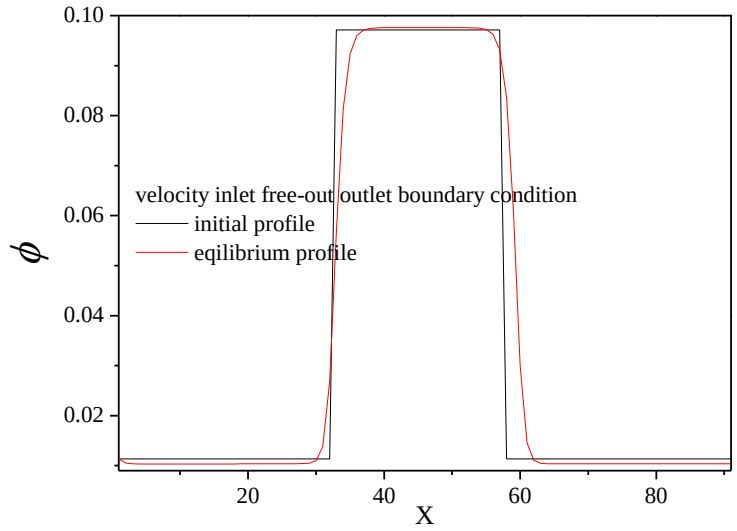

(b) profiles under the 0-velocity inlet and free-out outlet boundary condition

Fig. 3-23 Profiles of the order parameter in initial and equilibrium states

when simulating a droplet with a radius of 12 *dx*, and a blending factor of 1.0 under the 0-velocity inlet and the free-out outlet boundary conditions. Fig. 3-22 is the corresponding evolution histories of the accumulated order parameters added to the computation domain at the inlet and outlet, and the total ϕ in the whole domain. From this figure it can be seen that both the inlet and outlet can be the source of mass non-conservation in the simulation when the velocity inlet and free-out outlet boundary conditions are

implemented, and that the numerical treatment of the 0-velocity inlet creates much more mass to the computation domain than the one created by the advection effect at the outlet.

In fact, the mass increase at the inlet when adopting the velocity inlet boundary condition comes from the initial value setting of the order parameter in the gas and liquid phases. As shown in Fig. 2-4 and Eq. (2-20), the initial values of the liquid and gas phase order parameters , ϕ , are the values at the saturated state for a plane interface without considering the curvature effects. For a droplet with a curved interface, the curvature effect should take effect on the equilibrium and make the ϕ in the two phases reach a new equilibrium state with a different value. Fig. 3-23 illustrates the order parameter profiles at the initial and the equilibrium stages under the periodic boundary condition and the 0-velocity inlet and the free-out outlet, respectively. In the equilibrium stage, the ϕ in both the liquid and gas phases reach a new equilibrium value, due to the curvature effect. However, while the 0-velocity inlet boundary condition is adopted, at the inlet, a constant ϕ is used in the simulation; thus, the difference between the constant initial value and the equilibrium value creates a source of mass that leads to the volume expansion in the liquid phase in the all stages of simulation.

3.5 Conclusions

1 The volume expansion and shape oscillation of the droplet in the steady stage of the simulation comes from the implementation of the 0-velocity inlet and the free-out outlet boundary conditions; such numerical phenomena can be removed by using the periodic boundary condition.

2 Both the velocity inlet and the free-out outlet boundary conditions can be sources of mass non-conservation. The order parameter exchange with the outside at the outlet by the advection effect makes the outlet a source of mass non-conservation; the constant initial value set at the inlet (which is different from the equilibrium value) is another source of mass non-conservation.

3 The numerical treatment of the 0-velocity inlet is the main source of mass non-conservation in the simulation compared with the advection effect at the outlet while adopting the free-out outlet boundary condition.

4 Volume and shape variation mechanism

In the last chapter, the volume expansion and shape oscillation problems in the steady stage were removed by the implementation of the periodic boundary condition. However, the expanded volume and deformed shape remain constant in the steady state. Since accurately capturing the shape and maintaining a constant volume are very important in the simulation, so a deep understanding of the volume and shape variation mechanism in the unsteady stage is desired.

4.1 Volume and shape evolution history

Following the parameters, initial conditions, and schemes described in Chapter 2; as well as the periodic boundary condition described in Chapter 3; and using typical blending factor α values of 0.0, 0.5, and 1.0; water droplets with different radii placed in the center of the calculation domain are simulated to investigate the volume and shape variation mechanism in the unsteady stage. For simplicity, the explanation is mainly based on the simulation results of a droplet with a radius of 12 *dx*.

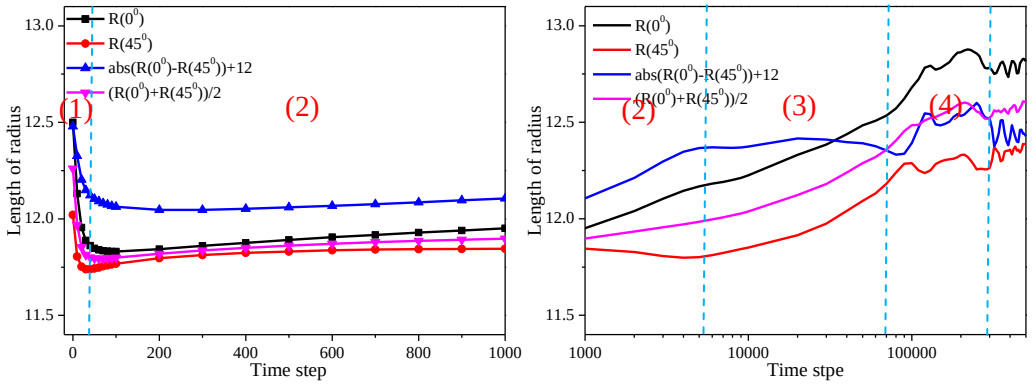

(a) R=12dx, a=0.0

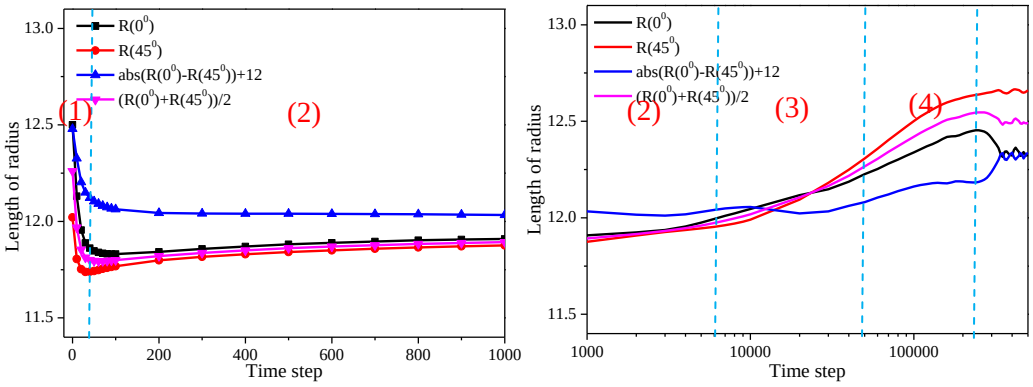

(b) R=12dx, a=0.5

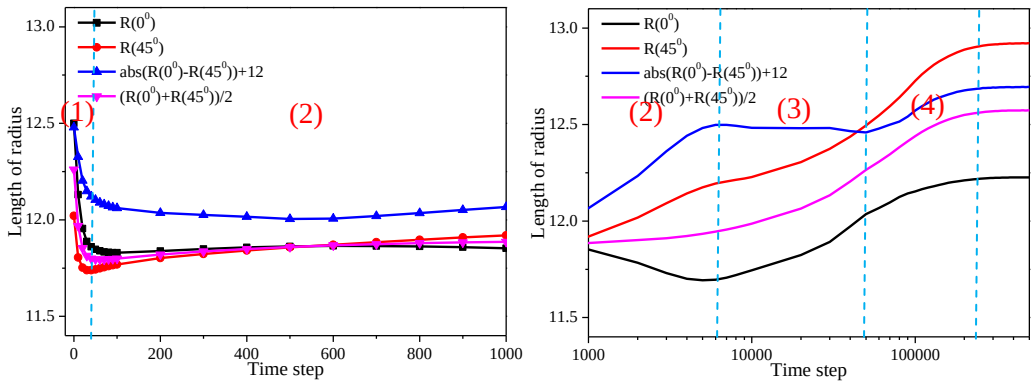

(c) R=12dx, a=1.0

Fig. 4-1 Examples of evolution histories of droplet radius, volume, and deformation degree

As shown from Figs. 1-1 and 1-4, the simulated droplet deforms symmetrically, so that the evolution histories of the droplet radii in two neighboring directions (in this dissertation, 0^0 and 45^0) can be used to determine the degrees of shape deformation and volume expansion. The volume variation degree of the simulated water droplet can be measured by comparing the averaged radius lengths along the two directions with the initial radius length; and the shape deformation degree can be measured by the difference between them. Fig. 4-1 shows the radius length; droplet volume, and shape deformation evolution histories of a water droplet with an initial radius of 12 *dx*. In this figure, the black line represents the radius length along the 0^0 direction; the red line represents the radius length along the 45^0 direction; the blue line shows the shape deformation degree and the pink line shows the volume expansion degree. Furthermore, to show the four lines in the same figure, the value of the blue line is increased by 12, which is the length of initial radius.

As shown in Fig. 4-1, the volume variation of the water droplet can be divided into two stages: the shrinking stage and the expansion stage. Meanwhile, combined with Fig. 4-2, the shape variation process can be divided into 4 stages, namely: (1) the initial shape removal stage, (2) the quick deformation stage, (3) the deformation stagnation stage, and (4) the slight deformation stage. Fig. 4-2 shows the corresponding typical shapes of the droplet in the 4 stages of the unsteady stage.

In Fig. 4-1 and Fig. 4-2, the shapes of the water droplet and the radius end are represented by the iso-surface where $\bar{\rho} = (\rho_G + \rho_L)/2$, or $\bar{\phi} = (\phi_G + \phi_L)/2$. Because the shape deformation, and volume variation only occur during the unsteady stage, the time step range in Fig. 4-1 and the figures below are limited to 500 thousand time steps. As the logarithmic coordinate (showing the time scale) used in the figures on the right hand of Fig. 4-1 cannot truly show the deformation history at the beginning of the

unsteady stage, the figures on the left hand of Fig. 4-1 with linear coordinates are adopted for supplementation; the numbers in the brackets of this figure represent the deformation stages in the unsteady stage. Similar treatments are followed by the other figures in this chapter.

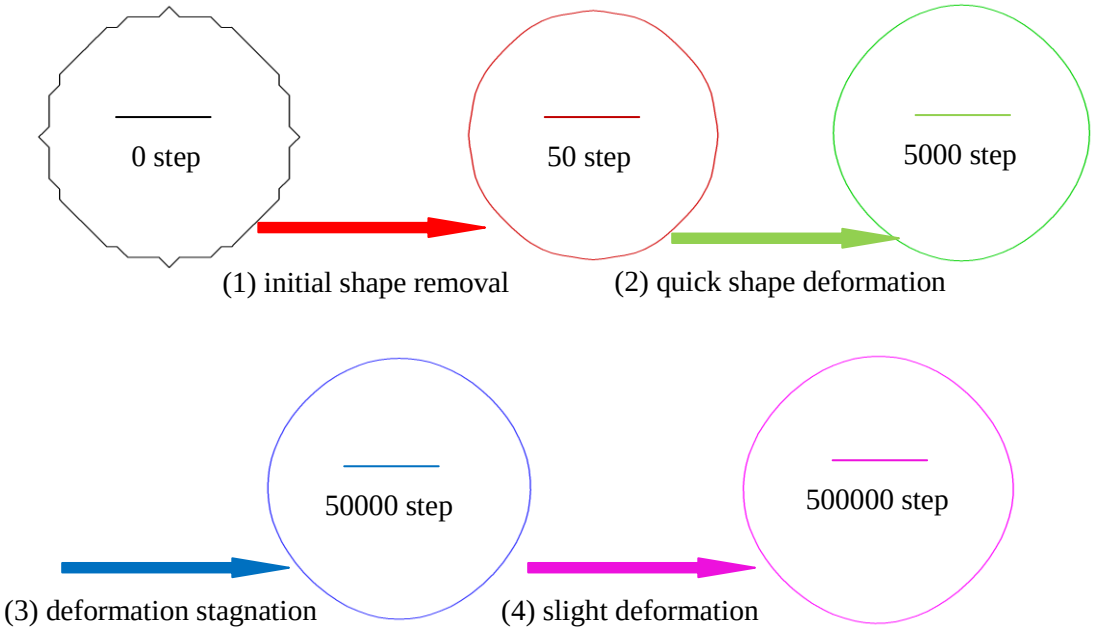

(a) R=12dx, a=0.0

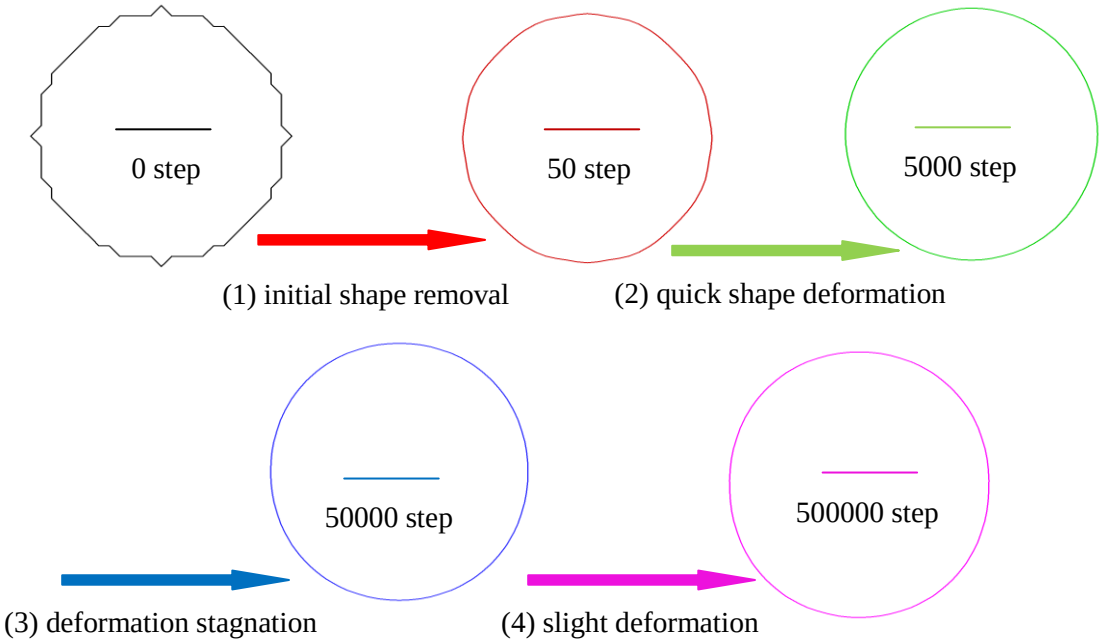

(b) R=12dx, a=0.5

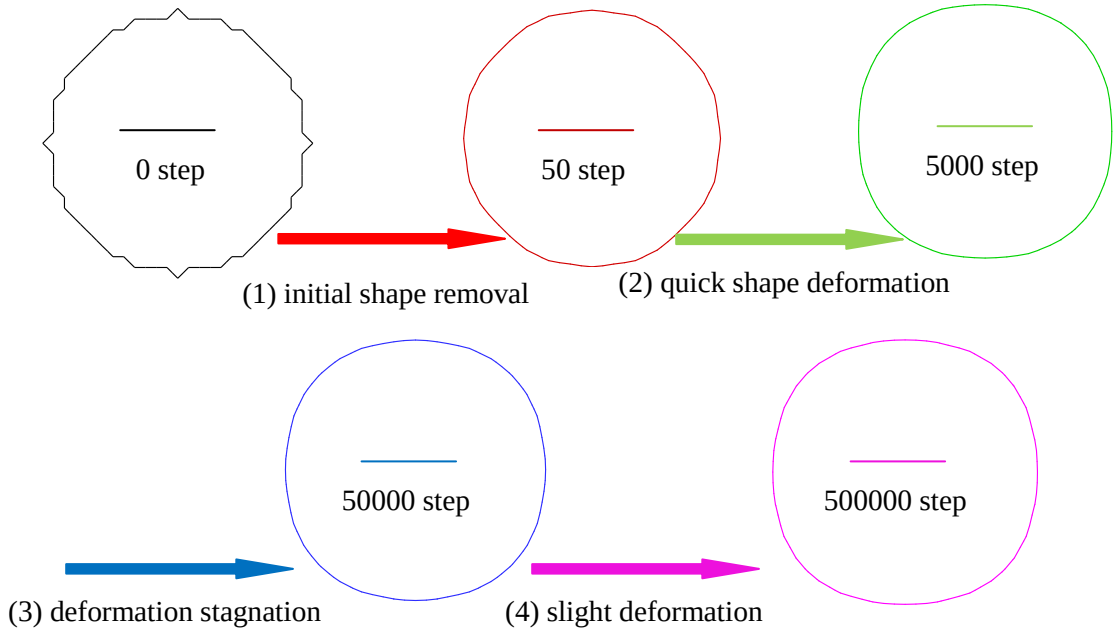

(c) R=12dx, a=1.0

Fig. 4-2 Examples of shape evolution histories of the water droplet in the unsteady stage

4.2 Interactions among the interface tension force, pressure gradient, and spurious velocity

In the present model, the shape and volume of a droplet is determined by the density or the order parameter distribution function, as described by the Eqs. (2-28), (2-30), (2-32), (2-38) . For convenience, we show Eq. (2-32) again here,

$$f_i^{eq} = H_i\phi + F_i\left[p_0 - \kappa_f\phi\frac{\partial^2\phi}{\partial x_\alpha^2} - \frac{\kappa_f}{6}\left(\frac{\partial\phi}{\partial x_\alpha}\right)^2\right] + 3E_i\phi c_{i\alpha}u_\alpha + E_i\kappa_f G_{\alpha\beta}(\phi)c_{i\alpha}c_{i\beta} \qquad 4\text{-}1$$

The distribution of the order parameter or the density of the two-phase system is decided by the balance effects of the pressure gradient force, the interface tension force and the velocity effect; or, mathematically speaking, the diffusion effect, the curvature effect and the advection effect. Physically, the shape of a stationary water droplet becomes constant and steady when its interfacial tension is balanced with the pressure gradient across the interface; at this moment, there is no velocity around the interface of the droplet. However, in the present LBM model, due to the imbalance of the discretized

force around the curved interfacial region of the liquid water /gas two-phase system, the spurious velocity field always exists in the simulation, as illustrated in Fig. 1-5 and Fig. 3-6. So the shape and volume variation in the simulation is determined by the interactions of the pressure gradient force, the interface tension force and the velocity effect. To thoroughly explain these interactions on the droplet shape and volume variation in the simulation, particularly in the unsteady stage, the simulation results of a droplet with a blending factor of α=1.0 and an initial radius of 12 *dx* will be adopted in the later discussions.

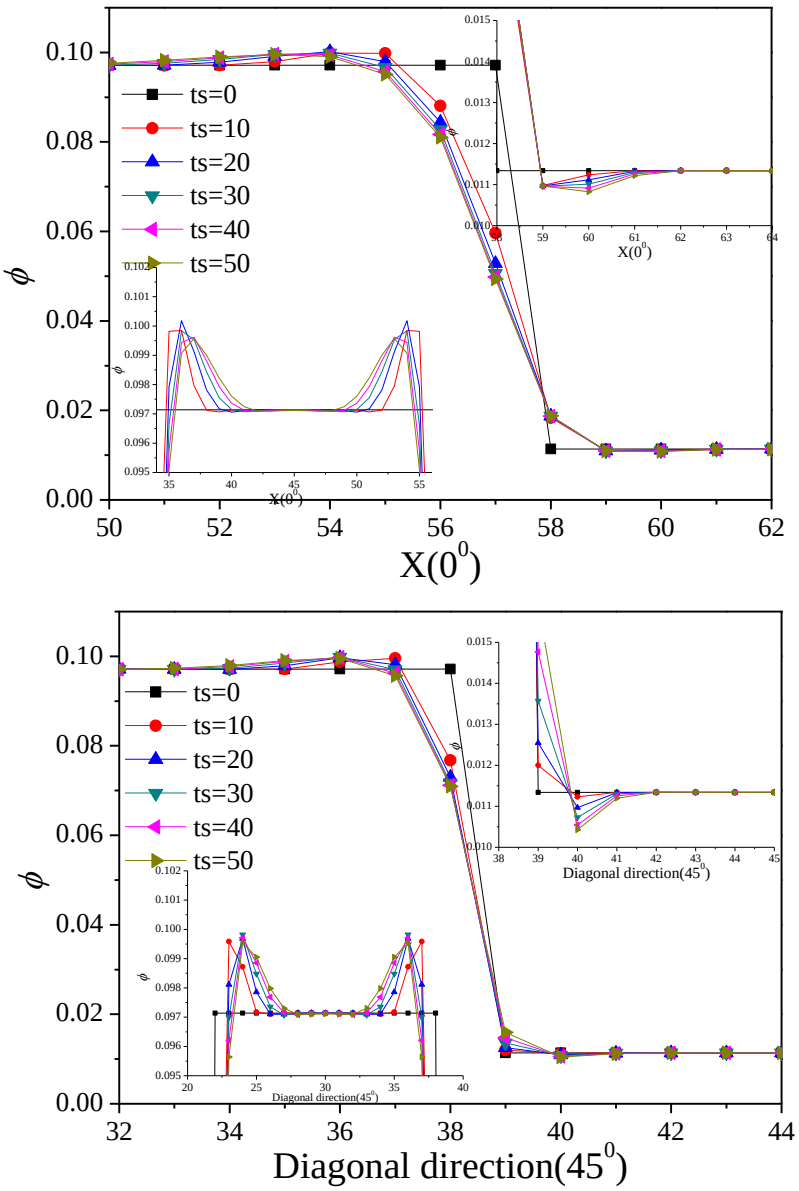

Fig. 4-3 Half profiles of the order parameter ϕ in the initial shape removal stage

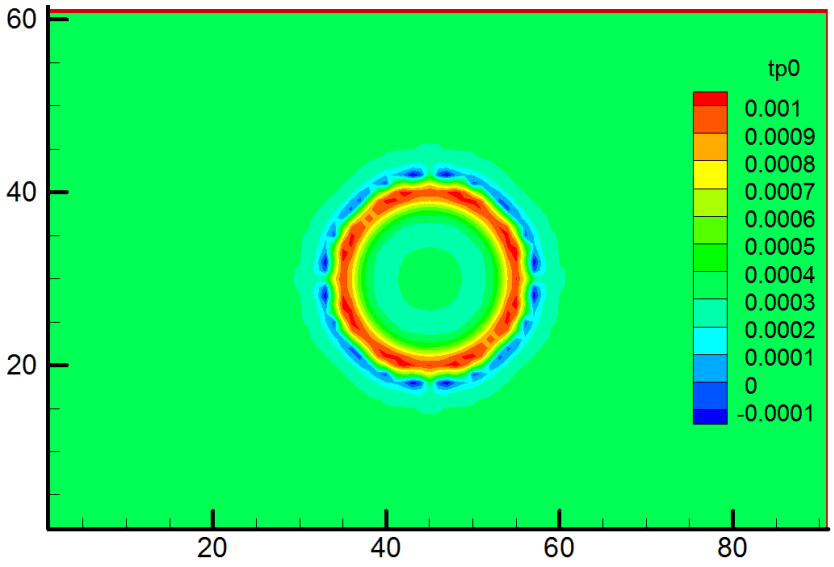

Fig. 4-4 Typical pressure field in the initial shape removal stage

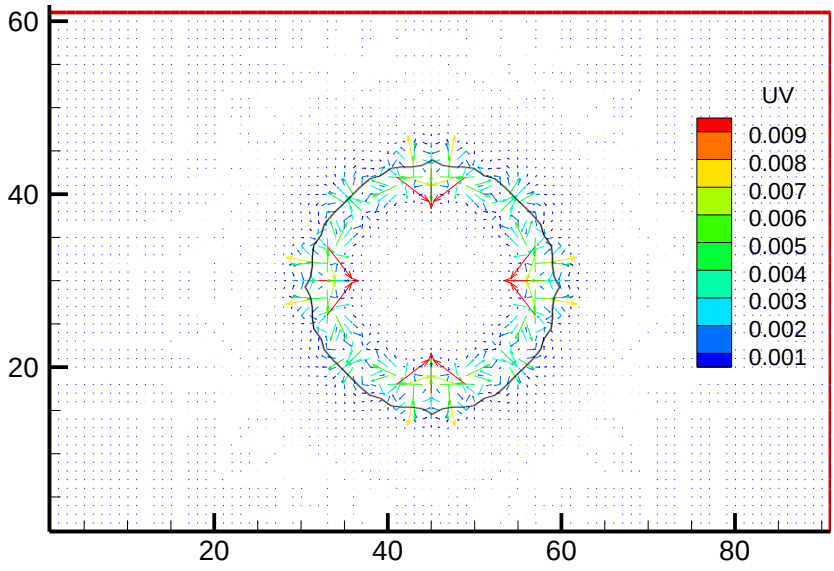

Fig. 4-5 Typical velocity field predicted in the initial shape removal stage

During the initial shape removal stage, as illustrated in Fig. 2-4, the initial values of the order parameter ϕ in the liquid and gas phases make the two phases have the same pressure of $p_0(\phi)$; this initial setting keeps the force balanced in the two bulk phases without considering the curvature effect. However, due to the large initial gradient of ϕ in the interface region of the droplet, as shown in Fig. 4-3,

a large interfacial tension, σ_f, is created. The large interfacial tension compressed the liquid phase inward the

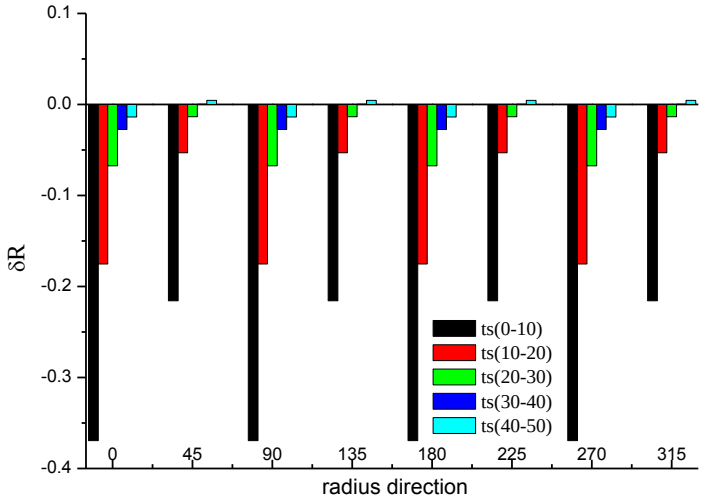

(a) real radius variation

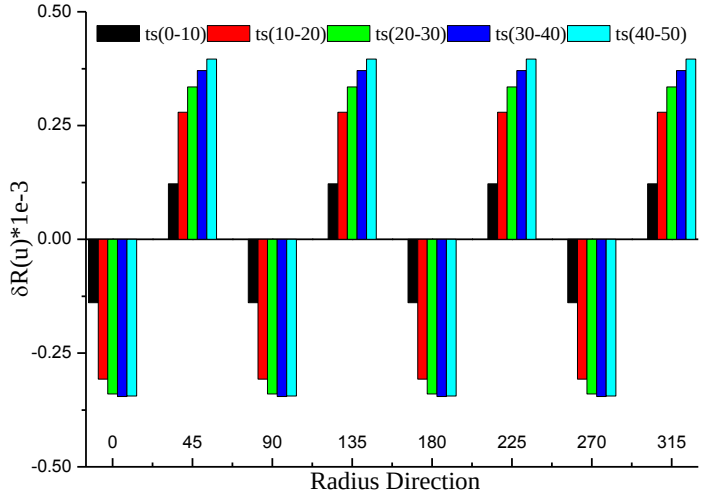

(b) radius variation calculated by velocity

Fig. 4-6 Radius variation in the initial shape removal stage

droplet and makes the ϕ and the pressure, $p_0(\phi)$, too high in the droplet (liquid phase), the ϕ in the gas phase is also dragged into the interfacial region, and $p_0(\phi)$ is lowered in the gas phase, particularly around the interface region. For the pressure defined in this LBM model, similar distribution can be observed as shown in Fig. 4-4, wherein $tp0(\phi) = p_0(\phi) - \kappa_f \phi \frac{\partial^2 \phi}{\partial x_\alpha^2} - \frac{\kappa_f}{6}\left(\frac{\partial \phi}{\partial x_\alpha}\right)^2$. Meanwhile, the curvature

effect of the interfacial tension force takes effect along the interface making the concave parts move outward and the convex parts move inward, as shown in Fig. 4-5, where the predicted velocity field and shape of the droplet are illustrated. During this process, the zigzag shape is removed and a smooth shape along periphery is formed, as in Fig. 4-2. Although the induced spurious velocity field is increasing in this stage, its magnitude is very small and its effect on the shape deformation of the droplet can be neglected, as illustrated in Fig. 4-6, wherein diagram (a) in Fig. 4-6 shows the real radius length variation in the first 50 time steps and diagram (b) shows the radius variation calculated from the velocity of the interface, where the order parameter gradient or the density gradient is maximum; here the x-axis represents the radius of the droplet along the corresponding directions. In this stage, the curvature effect of the interface tension force and the diffusion effect of the pressure gradient dominate the shape and volume variation. Fig. 4-7 shows the variation of the order parameter profile in the interface region along the 0^0 and 45^0 directions. From this figure, we can find that the interface with the appropriate density distribution inside it is still in the process of evolution.

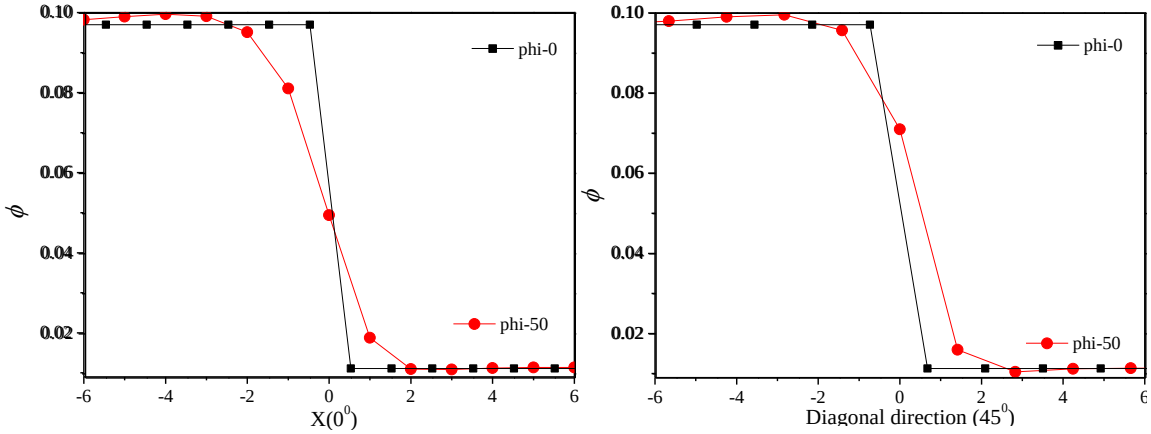

Fig. 4-7 Half profiles of ϕ in the interface region in the initial shape removal stage

During the quick shape deformation stage, first the overshot $p_0(\phi)$ or $tp0(\phi)$ around the interface region diffuses inward to form a smooth distribution; meanwhile, this drives the interface of the droplet outward, and Fig. 4-8 depicts typical $tp0(\phi)$ distributions in this period. Correspondingly, the order parameter, ϕ, diffuses in toward the center of the droplet to form a smooth distribution, and outward to expand the volume of the droplet, as shown in the left inserts of Fig. 4-9. During this stage, the induced velocity continuously increases and gradually takes effect on the shape of the droplet. As shown in Fig. 4-10, the induced spurious velocity field in the interface region flows inward in the orthogonal directions and outward in the diagonal directions. The transportation of the order parameter, ϕ, in the diagonal

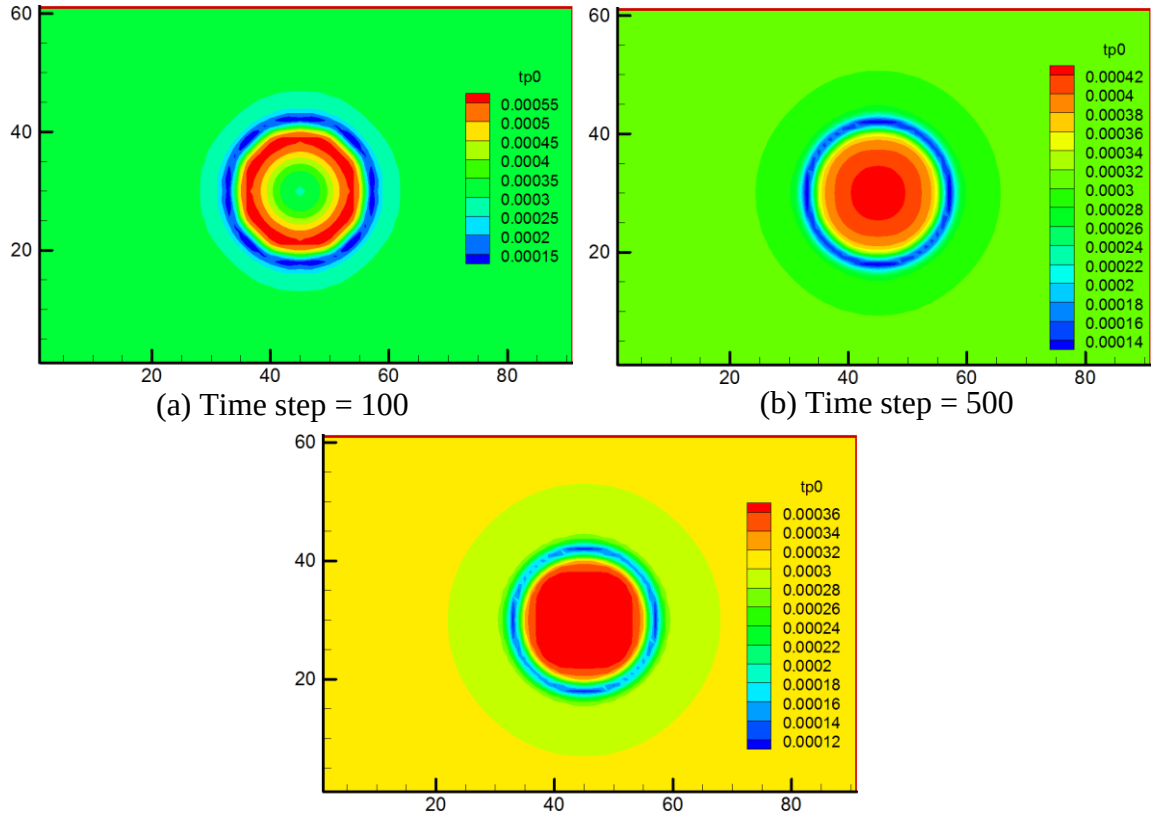

(a) Time step = 100 (b) Time step = 500

(c) Time step = 1000

Fig. 4-8 Typical pressure distributions in the first stage of the rapid shape deformation stage

directions is enhanced, but blocked in the orthogonal directions, due to the velocity direction differences in the interface. The overshot ϕ in the droplet therefore mostly flows outward along the diagonal directions, and the increasing velocity in the orthogonal directions finally drives the ϕ at the interface inward, as shown in Fig. 4-9. This leads to the expansion of the interface along the diagonal directions and contraction along the orthogonal directions, which causes the droplet shape beginning to deform in a rectangular shape, as illustrated in Fig. 4-1. In this stage, the diffusion of ϕ from the liquid phase to the interface region is gradually decreasing, the appropriate interface with a suitable order parameter distribution is gradually converging, and the increasing velocity effect is gradually playing a more obvious role in the force balance of the two-phase system. In general, the shape and volume variation is determined by the interaction of pressure gradient force, the interface tension force and the velocity effect. Fig. 4-11 illustrates the radius variation in this process, from this figure; we can conclude that the advection effect from the velocity field is gradually dominating the shape deformation of the droplet, as the radius change predicted by the velocity effect is more and more closing to the real radius change in

this process. Fig. 4-12 illustrates the interface profile variations in this process; it shows that the appropriate interface is still forming and has not yet converged; the order parameters from both the liquid and the gas phases are diffusing into the interface region.

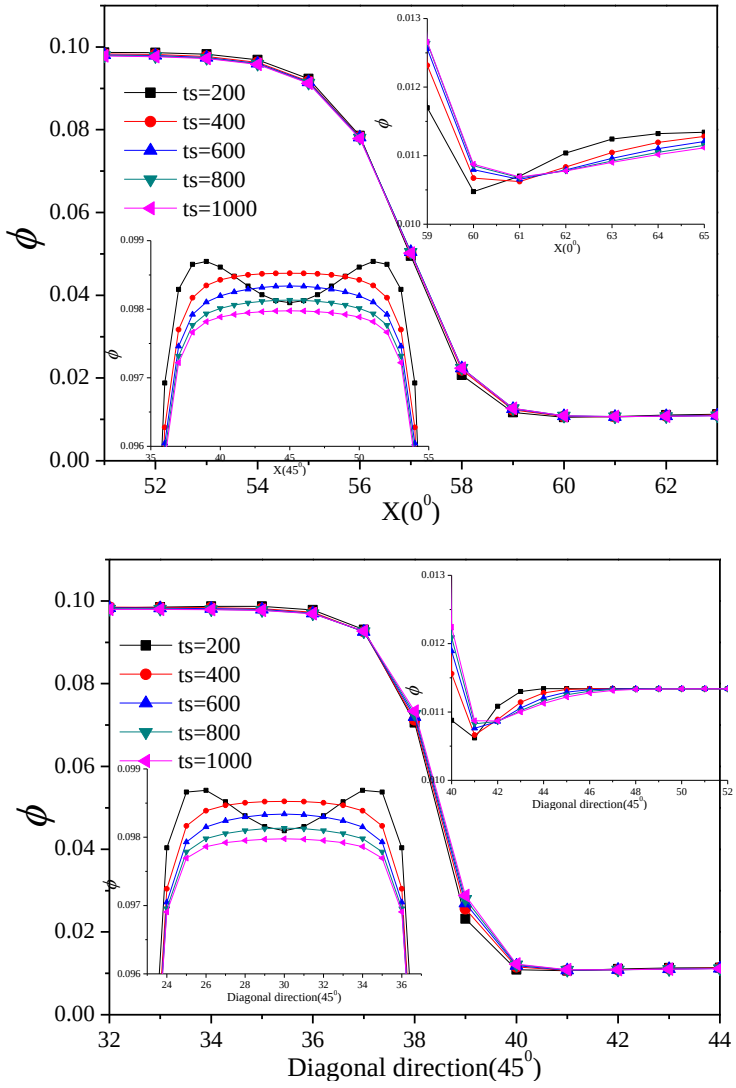

Fig. 4-9 Half profiles of the ϕ in the first stage of the rapid shape deformation stage

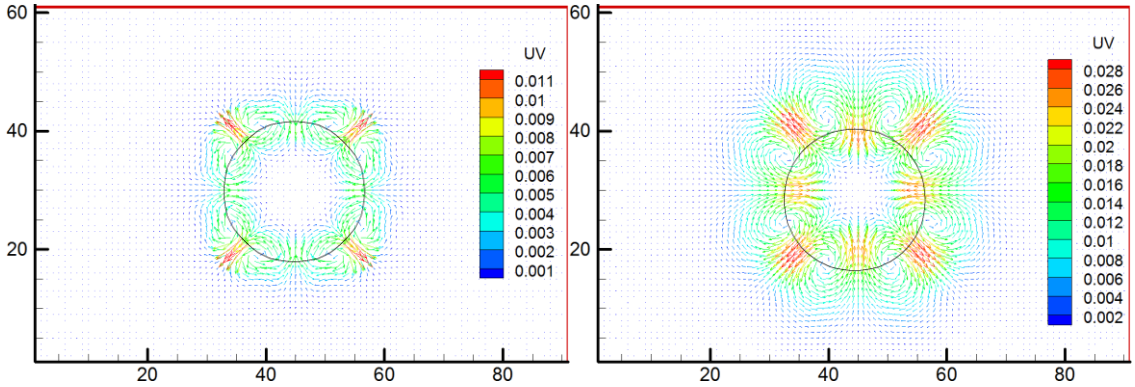

(a) Time step = 100 (b) Time step = 1000

Fig. 4-10 Velocity fields predicted in the first stage of the rapid shape deformation stage

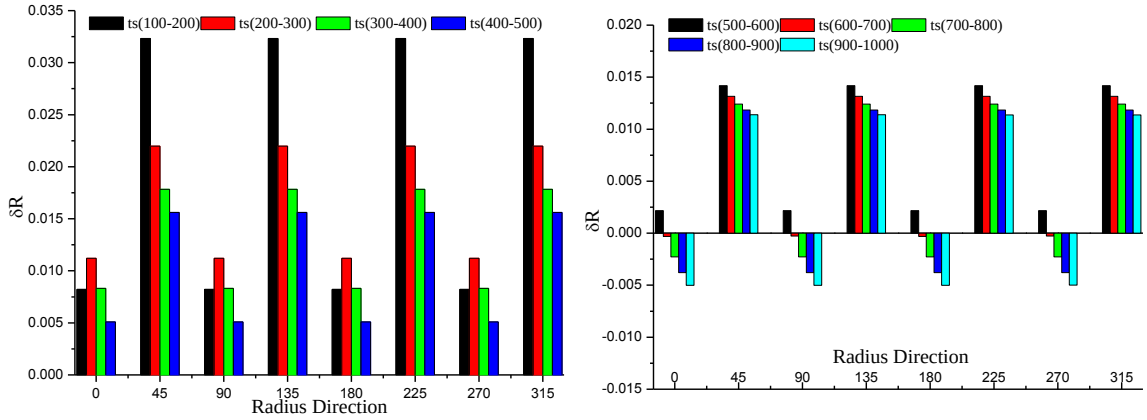

(a) real radius variation

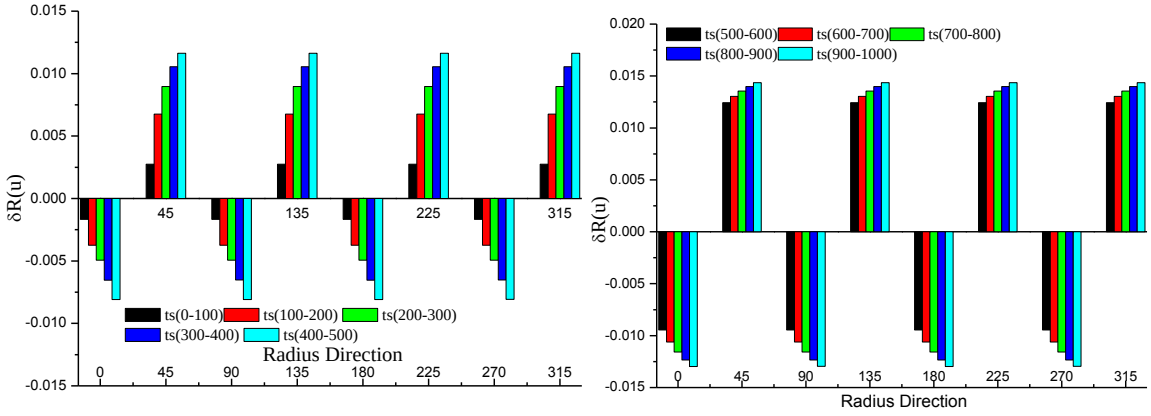

(b) radius variation calculated by velocity

Fig. 4-11 Radius variation in the first stage of the rapid shape deformation stage

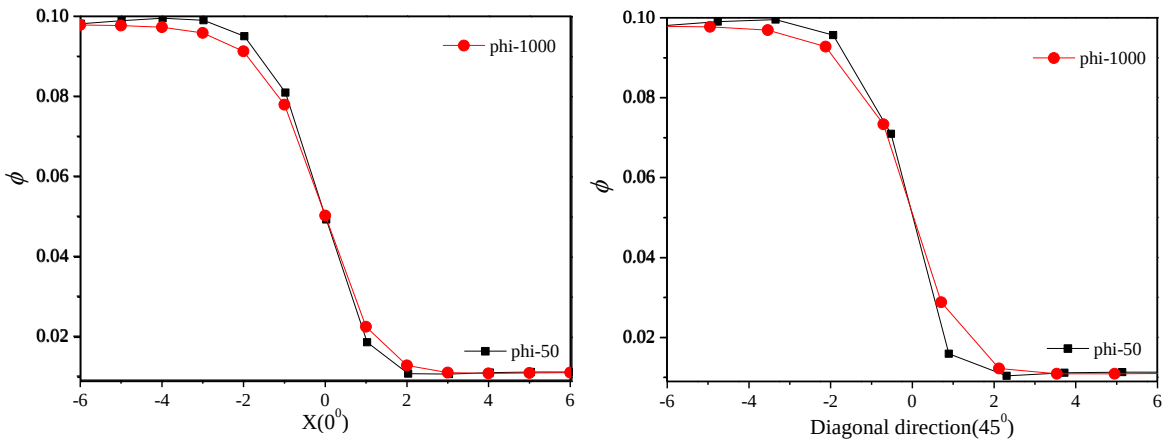

Fig. 4-12 Interface profile in the first stage of the rapid shape deformation stage

In the later stage of the rapid shape deformation stage, the expansion caused by the diffusion of the liquid phase ϕ and the absorption of the gas phase ϕ by the interface is very small, as shown in the insets of Fig. 4-13. The shape deformation of the droplet is primarily driven by the advection effect of the spurious velocity field, and this effect is mainly balanced by the curvature effect of the interface tension force. Fig. 4-14 shows the typical pressure distributions in the this process, and Fig. 4-15 shows interface profiles of the droplet along the 0^0 and 45^0 directions; from these figures, it can be seen that during this process, the pressure gradient of $tp0(\phi)$ across the interface keeps constant and the

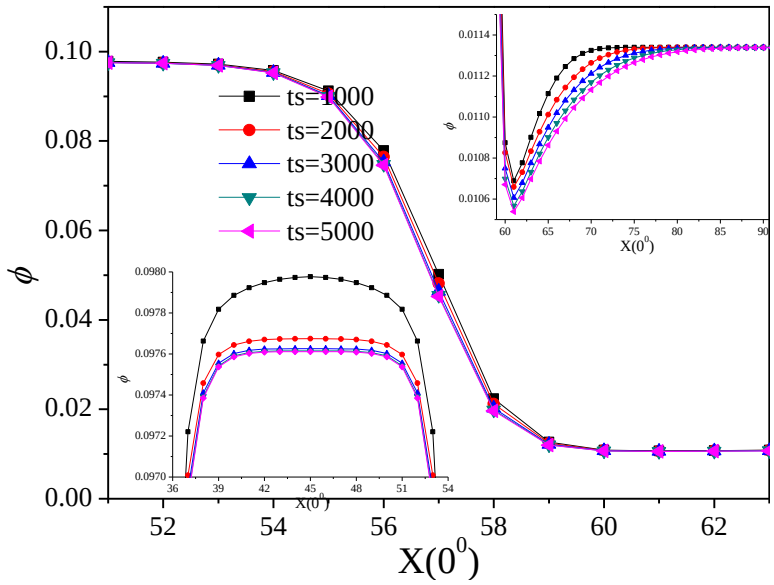

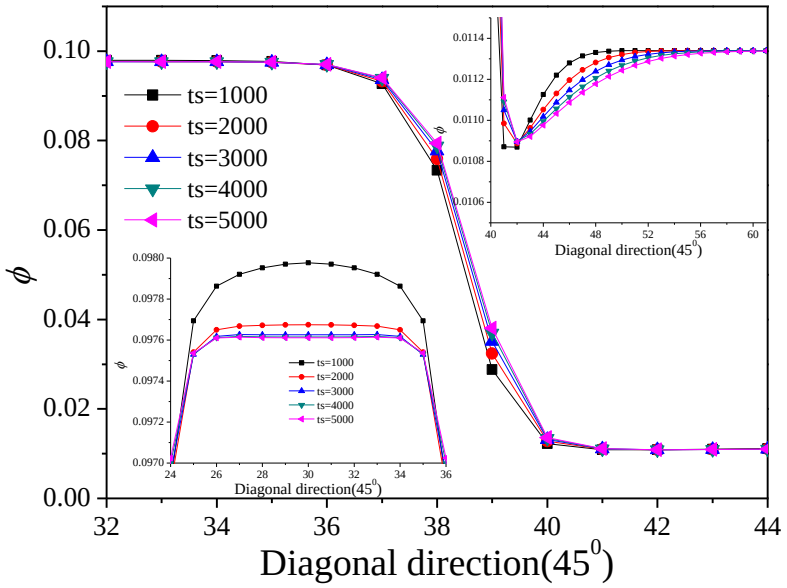

Fig. 4-13 Half profiles of the ϕ in the later stage of the rapid shape deformation stage

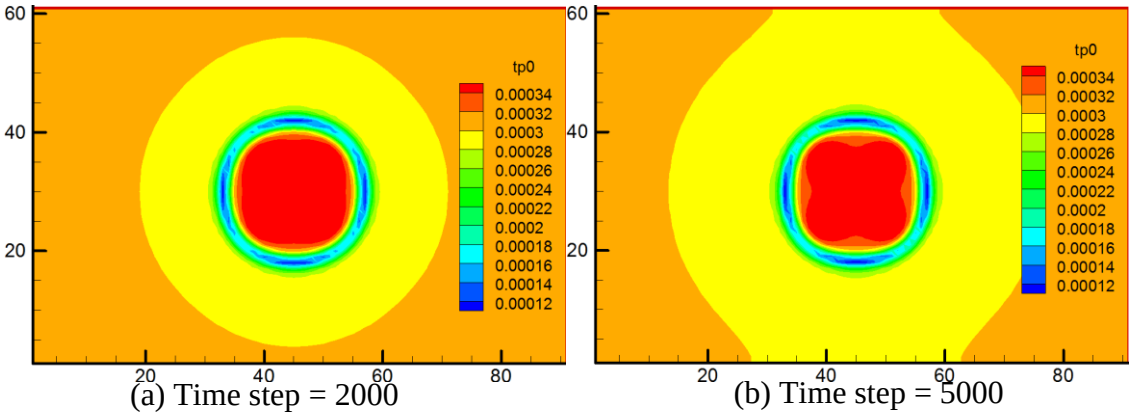

Fig. 4-14 Pressure distributions in the later stage of the rapid shape deformation stage

interface profiles have already converged. This means the movement of the interface is mainly caused by the advection effect. The radius variations shown in Fig. 4-17 further prove that the advection effect drives the shape deformation, as the real radius change is almost consistent with the radius variations calculated from the velocity field, not only in order but also in direction. As shown in Fig. 4-14 that the pressure gradient keeps constant around the interface region along the orthogonal and diagonal directions, so the advection effect or the velocity effect is balanced by the curvature effect. Fig. 4-16 shows typical velocity fields in this process, the magnitude of the spurious velocity decrease around interface region further validates this conclusion.

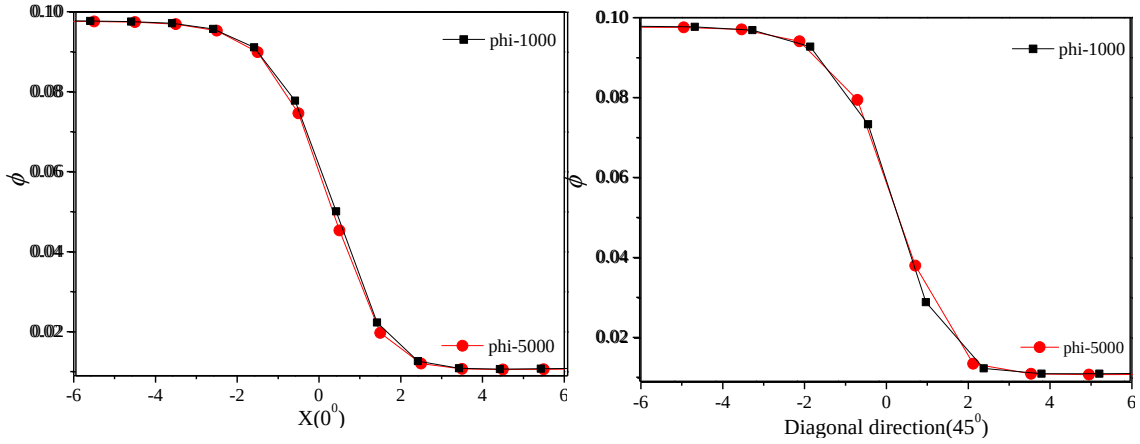

Fig. 4-15 Interface profile in the later stage of the rapid shape deformation stage

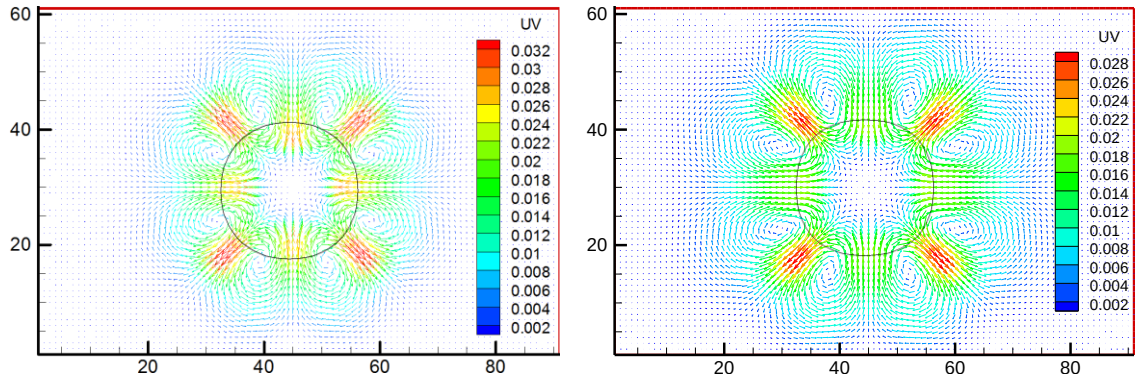

(a) Time step = 2000 (b) Time step = 1000

Fig. 4-16 Velocity fields predicted in the later stage of the rapid shape deformation stage

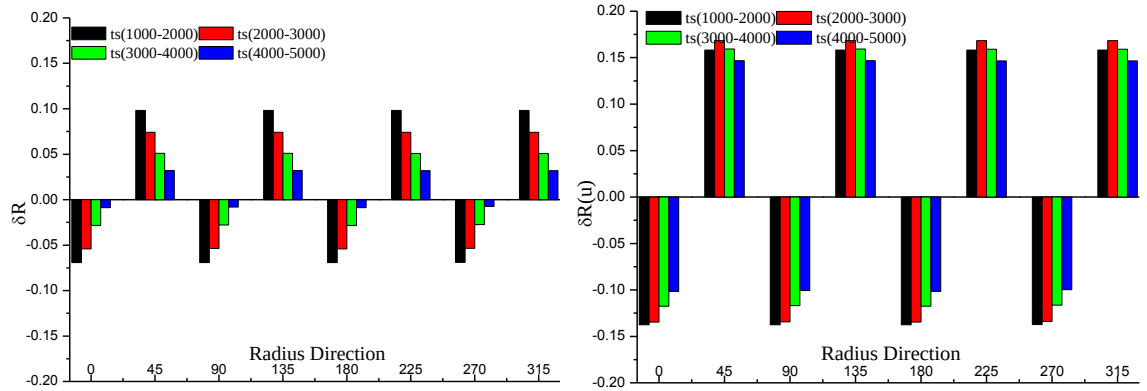

(a) real radius variation (b) radius variation calculated by velocity

Fig. 4-17 Radius variation in the later stage of the rapid shape deformation stage

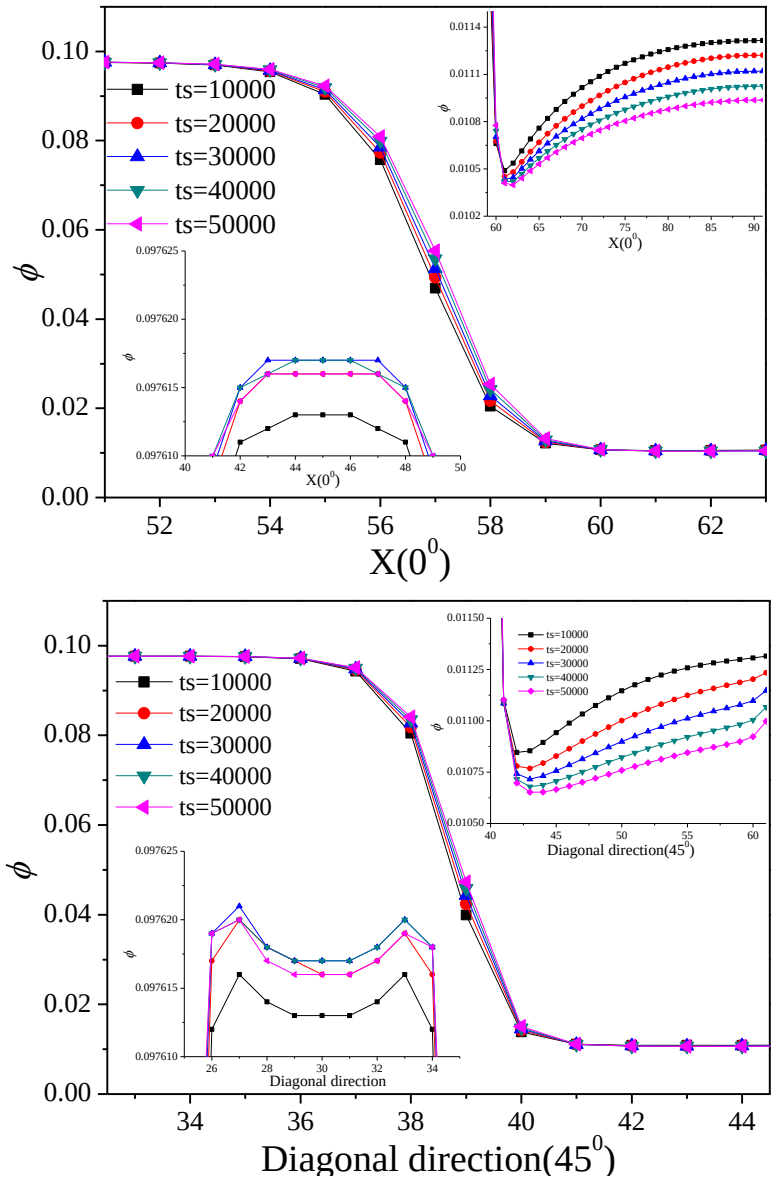

Fig. 4-18 Half profiles of the ϕ in the deformation stagnation stage

In the shape deformation stagnation stage, the shape of the simulated droplet remains constant, but its volume is continuously increasing. In the quick shape deformation stage, the pressure gradient, $\nabla \cdot tp0(\phi)$, across the interface, the spurious velocity field, and the interfacial tension force finally almost balanced with each other. The uniform expansion of the droplet, as shown in Fig. 4-18, comes from continuously absorbing the gas phase ϕ into the interfacial region, as locally around the contact line of the gas phase and the interface, the interfacial tension continuously drags the gas phase ϕ into the interfacial region before it is balanced by the pressure gradient, $\nabla \cdot tp0(\phi)$. In this stage, the ϕ in the gas

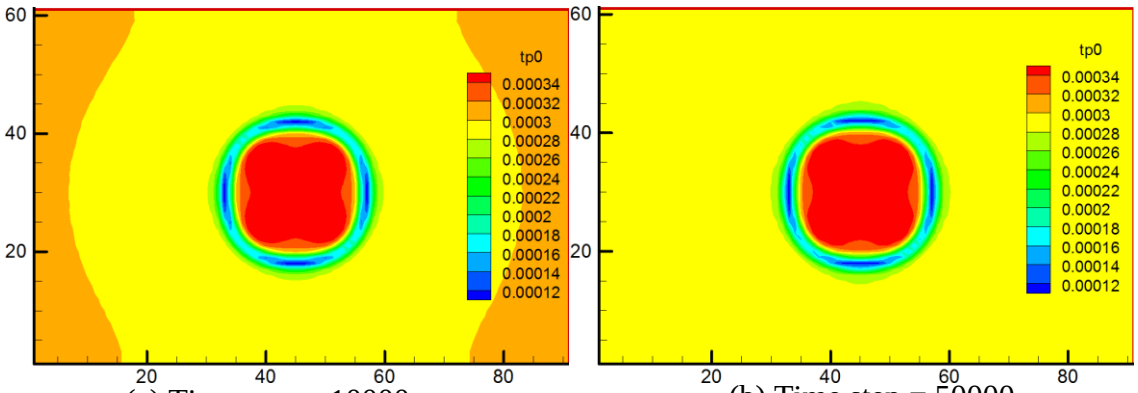

(a) Time step = 10000 (b) Time step = 50000

Fig. 4-19 Pressure distributions in the deformation stagnation stage

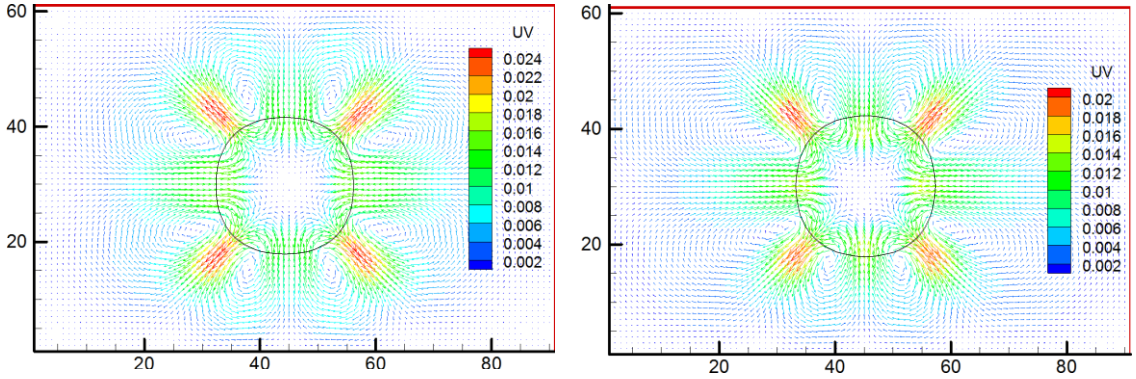

(a) Time step = 10000 (b) Time step = 50000

Fig. 4-20 Examples of the velocity fields in the deformation stagnation stage

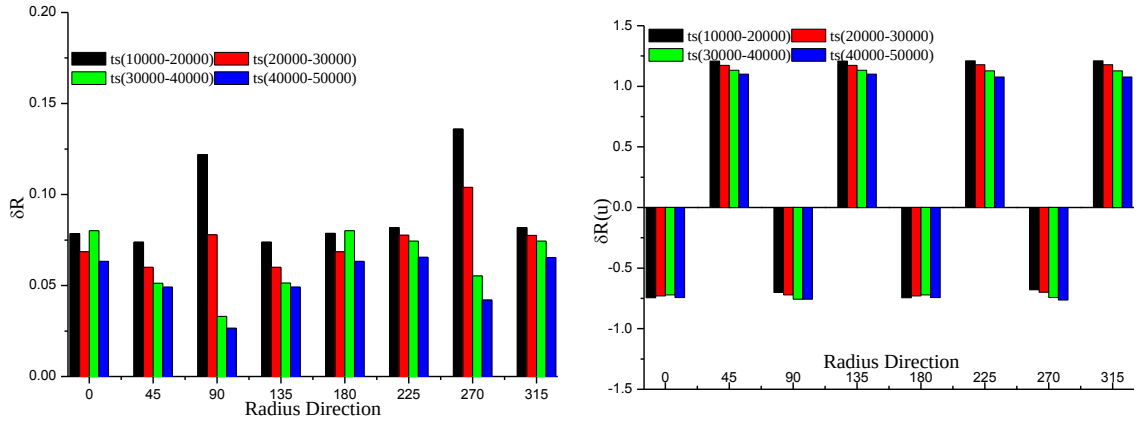

(a) real radius variation (b) radius variation calculated by velocity

Fig. 4-21 Radius variation in the deformation stagnation stage

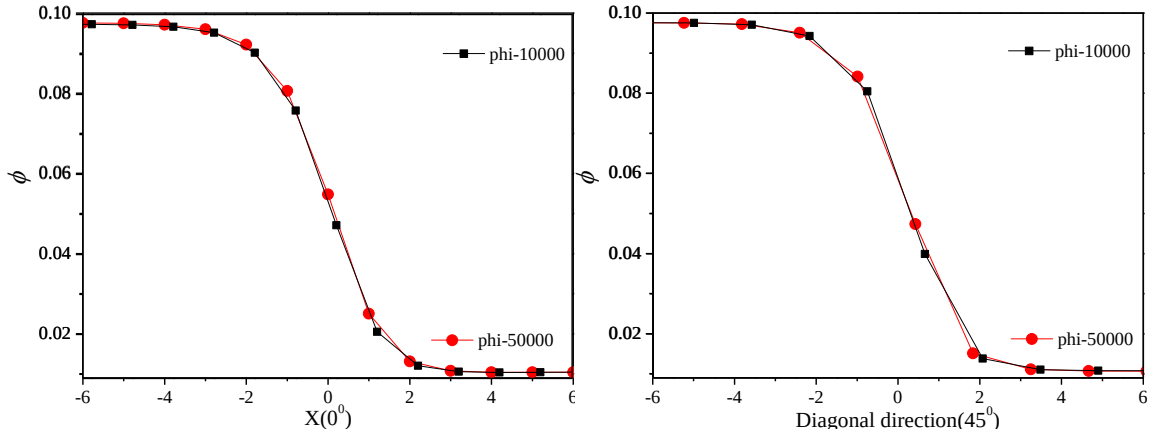

Fig. 4-22 Interface profile in the deformation stagnation stage

phase is small, the spurious velocity field in this region has very little effect, and the gas phase ϕ is uniformly absorbed into the interface without leading to obvious shape deformation. Because the ϕ in the gas phase continuously decreases, as shown in the inserts of Fig. 4-18, the corresponding pressure, $tp0(\phi)$, in the gas phase continuously decreases; at the same time, the $tp0(\phi)$ in the liquid phase remains constant, thus leading to a slight increase in the pressure difference across the interface of the droplet, as shown in Fig. 4-19. The increased pressure gradient is spontaneously balanced in all directions for the droplet by the interfacial tension force coming from its scalar gradient component. In the uniform expansion stage, the shape of the droplet and the profiles of the ρ and ϕ do not change in an obvious way, and there is only a small change in the magnitude of the spurious velocity field, as shown in Fig. 4-19 and in the interface region the spurious velocity keeps constant. Fig. 4-20 illustrates the radius variations in this stage, from these figures, it can be seen that the velocity effect has been balanced by the curvature effect, and that the radius change calculated by the velocity field cannot predict the real radius change in both magnitude and direction at this stage. Fig. 4-22 shows interface profiles of the droplet along the two neighboring directions. The two figures further prove that the interface profile has already converged.

Following the deformation stagnation stage is the slight shape deformation or adjustment stage. Gradually, with the continuous absorption of the gas phase ϕ to the interface, the pressure gradient, $\nabla \cdot tp0(\phi)$, across the contact line of the gas phase and the interface tends to balance with the scalar gradient part of the interfacial tension force, the spurious velocity field, and the boundary conditions begin to take effect in the gas phase region, as illustrated in Fig. 4-23. In the slight expansion and deformation stage, the ϕ in the gas phase is still continuously absorbed into the interface region with a

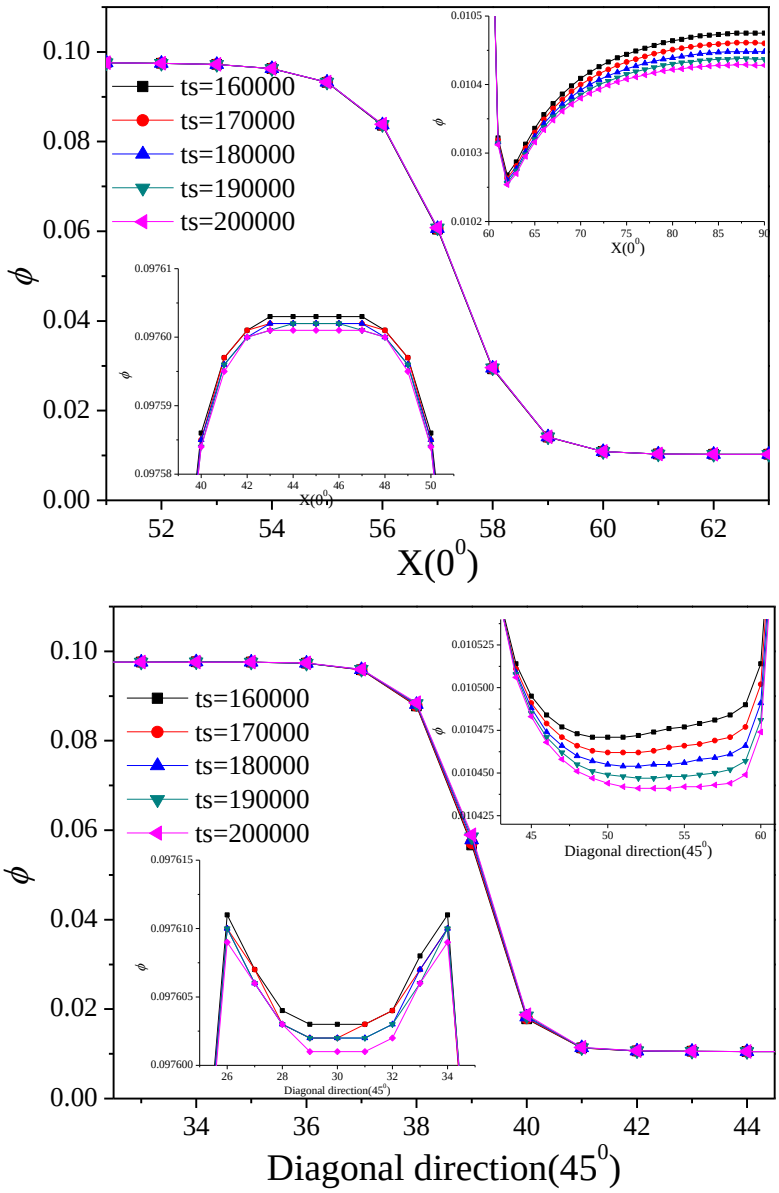

Fig. 4-23 Half profiles of the ϕ in the slight shape deformation stage

slower speed. Because of the spurious velocity field, the profile of the order parameter ϕ in the gas phase gradually changes, and eventually a steady state is established by balancing the effects of the spurious velocity field, boundary conditions, interfacial tension, and pressure gradient, $\nabla \cdot tp0(\phi)$, across the contact line of the gas phase and the interface, as shown in the insets of Fig. 4-23. In this process, the adjustment of these factors slightly changes the profile of the ϕ in different directions of the droplet and leads to a slight magnitude increase for the spurious velocity field, as shown in Fig. 4-24. As the ϕ in the gas phase continuously decreases and the ϕ in the liquid phase remains constant, the pressure gradient, $\nabla \cdot tp0(\phi)$,

across the interface of the droplet increases; this increased pressure gradient drives the interface of the droplet outward to expand its volume. During this process, the enhanced spurious velocity field affects the shape deformation; the expansion in the diagonal directions is enhanced and the expansion in the orthogonal directions is compressed, leading to a further shape deformation. The effect of the increased velocity is gradually balanced by the curvature effect of the interfacial tension force in the diagonal directions and by the decreasing curvature effect in the orthogonal directions, as shown in Fig. 4-1. Eventually, a final balance between the pressure gradient $\nabla \cdot tp0(\phi)$ across the droplet interface, the spurious velocity field, and the interfacial tension force is established, and the simulation reaches the steady state. Correspondingly, Fig. 4-25, Fig. 4-26 and Fig. 4-27 illustrate the typical pressure distributions, radius variations, and the interface profiles at this stage.

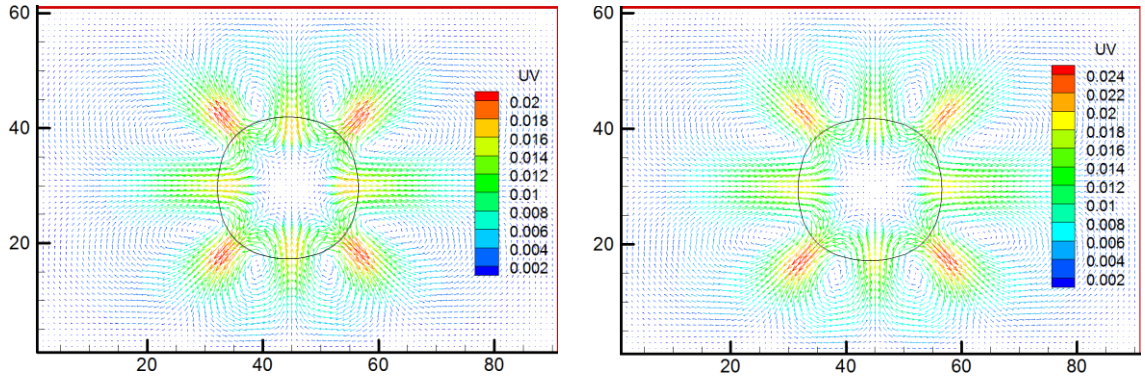

(a) Time step = 100000 (b) Time step = 300000

Fig. 4-24 Typical velocity fields in the slight shape deformation stage

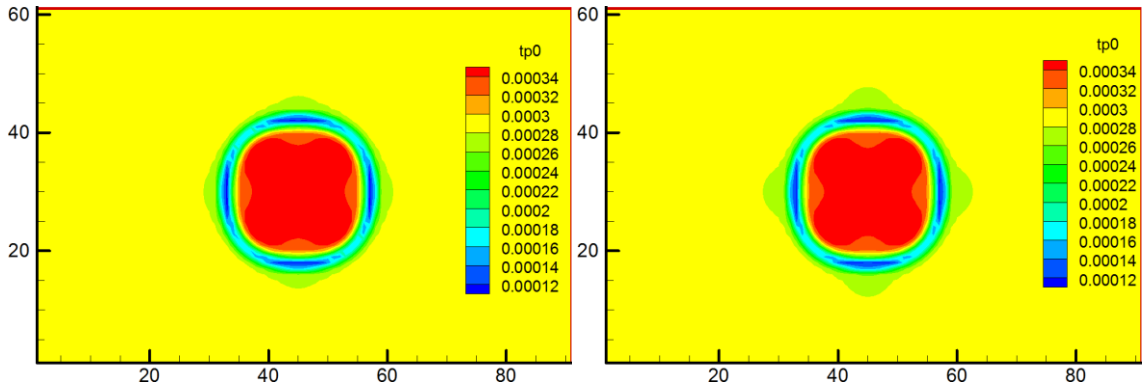

(a) Time step = 100000 (b) Time step = 300000

Fig. 4-25 Pressure distributions in the slight shape deformation stage

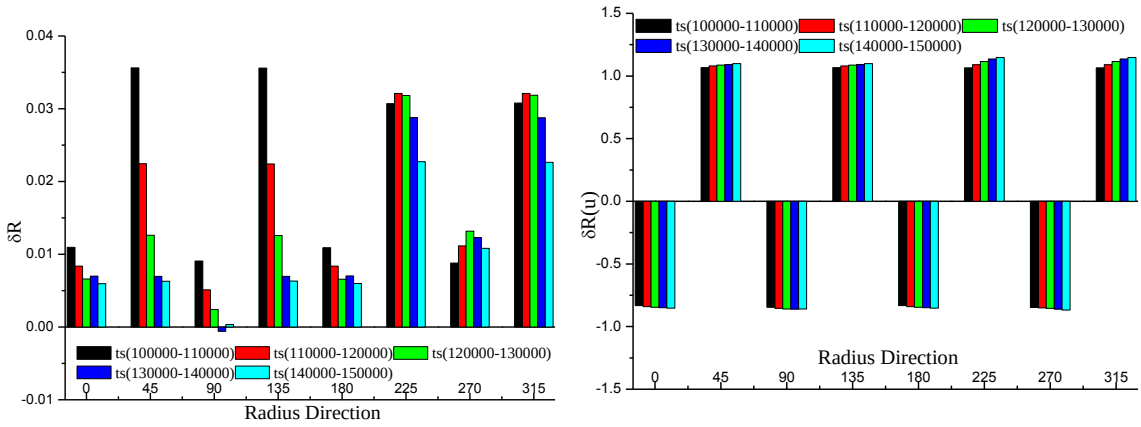

(a) real radius variation (b) radius variation calculated by velocity

Fig. 4-26 Radius variation in the slight shape deformation stage

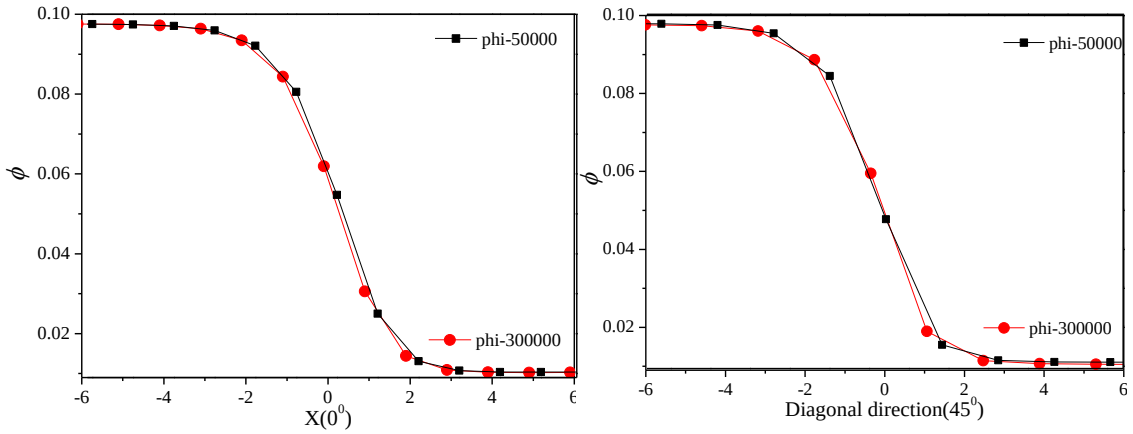

Fig. 4-27 Interface profile in the slight shape deformation stage

4.3 Validations of the volume and shape variation mechanism

From the analysis made in last section, it can be concluded that the shape of the droplet is determined by the interactions of the pressure gradient force, the interfacial tension force and the velocity effect. The shape deformation in this model is mainly coming from the advection effect of the spurious velocity, which is balanced by curvature effect of the interface tension force. The interactions of the diffusion effect and the advection effect also would induce shape deformation. The volume variation of the droplet arises from the interactions of the diffusion effect and the curvature effect; which comes from the initial inappropriate density distributions inside the interface and inappropriate initial order parameter settings in the two phases.

To validate these conclusions, three simulation cases were implemented:

1) Simulations with the initial order parameter values in the two phases coming from the equilibrium state instead of from the bulk phases without considering the curvature effect.
2) Simulations with the LBM model that remove the advection effect but keep present initial order parameter settings in two phases.
3) Simulations with the LBM model that remove the advection effect and use the initial order parameter values in the two phases from the equilibrium state.

In the second and third test cases, the equilibrium distribution function of f_i^{eq} became the following form:

$$f_i^{eq} = H_i\phi + F_i\left[p_0 - \kappa_f\phi\frac{\partial^2\phi}{\partial x_\alpha^2} - \frac{\kappa_f}{6}\left(\frac{\partial\phi}{\partial x_\alpha}\right)^2\right] + E_i\kappa_f G_{\alpha\beta}(\phi)c_{i\alpha}c_{i\beta} \qquad 4\text{-}2$$

The equilibrium values of the initial order parameters in the two phases are acquired in the simulation results in last section.

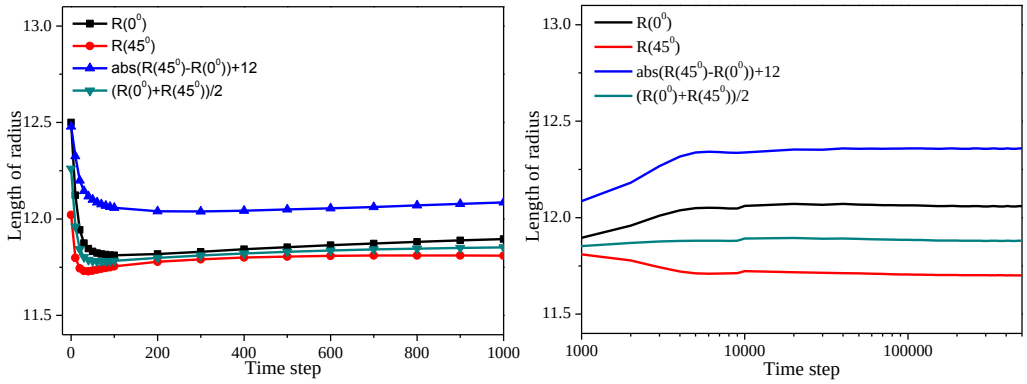

(a) R=12dx, α=0.0

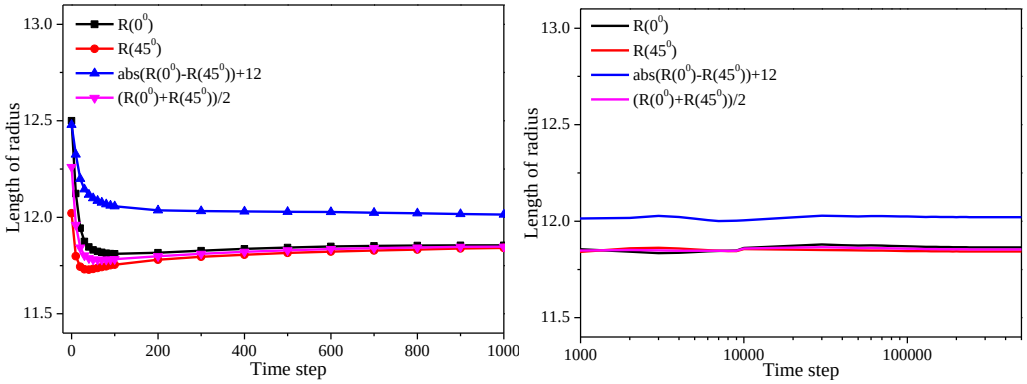

(b) R=12dx, α=0.5

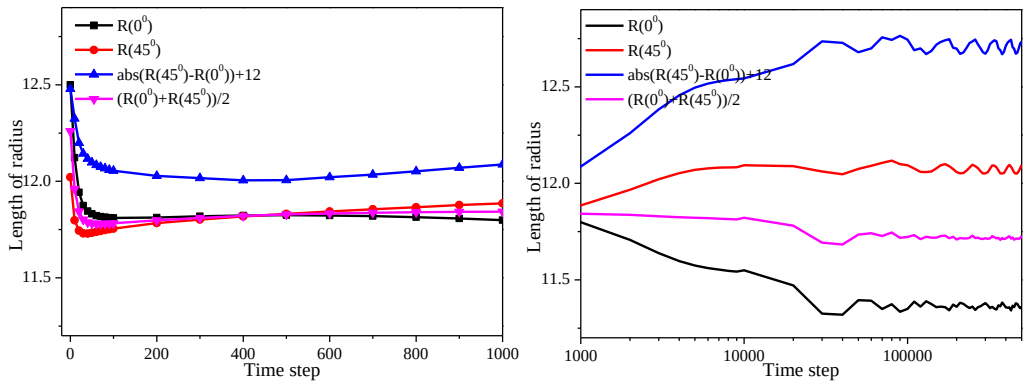

(c) R=12dx, α=1.0

Fig. 4-28 Radius evolution history when initial ϕ_G and ϕ_L are set to their equilibrium values

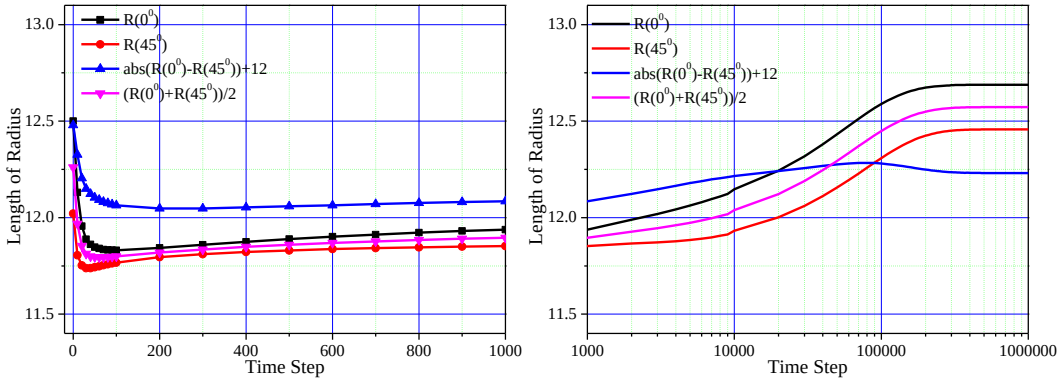

Fig. 4-29 Radius evolution history without advection effect

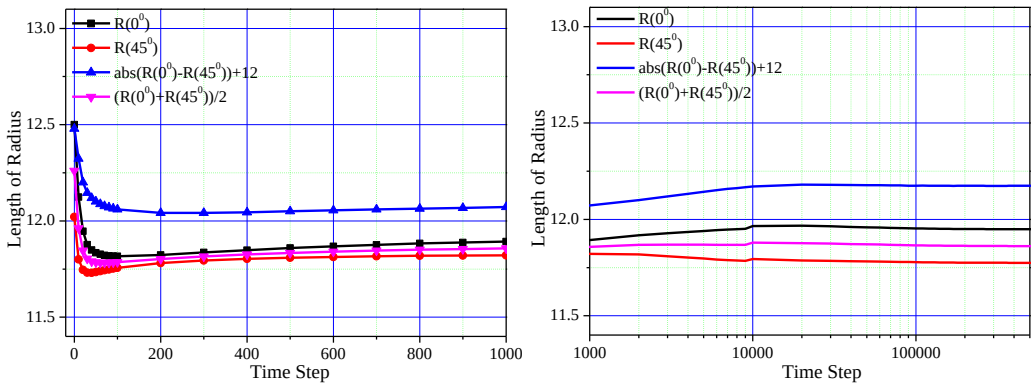

Fig. 4-30 Radius evolution history without advection effect when initial ϕ_G and ϕ_L are set to their equilibrium values

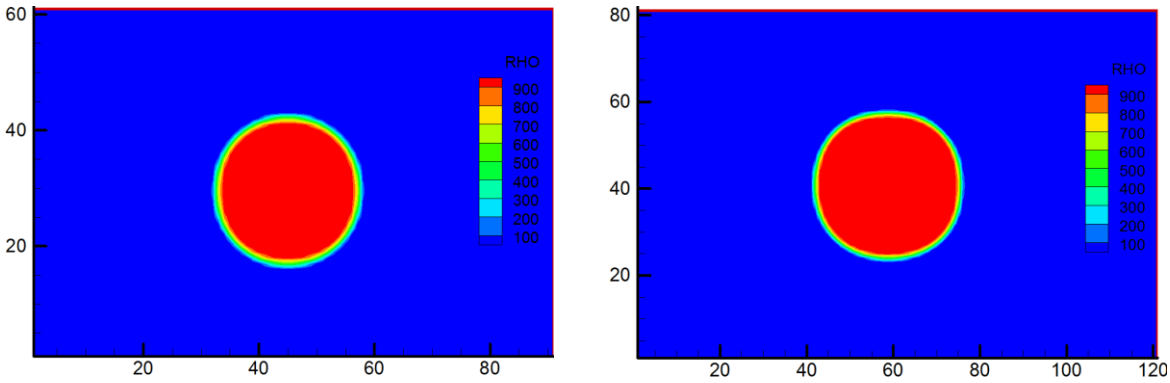

(a) R= 12 dx (b) R= 16 dx

Fig. 4-31 Density distributions when α= 0.5

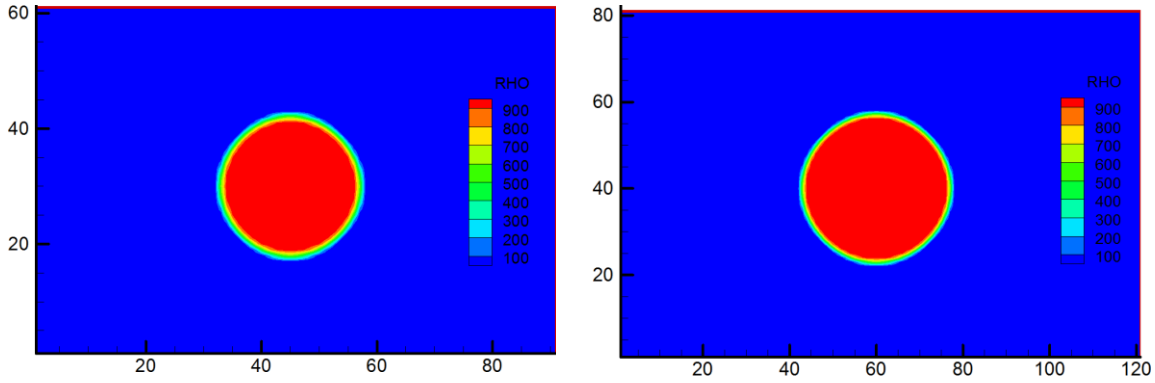

(a) R= 12 dx (b) R= 16 dx

Fig. 4-32 Density distributions without advection effect

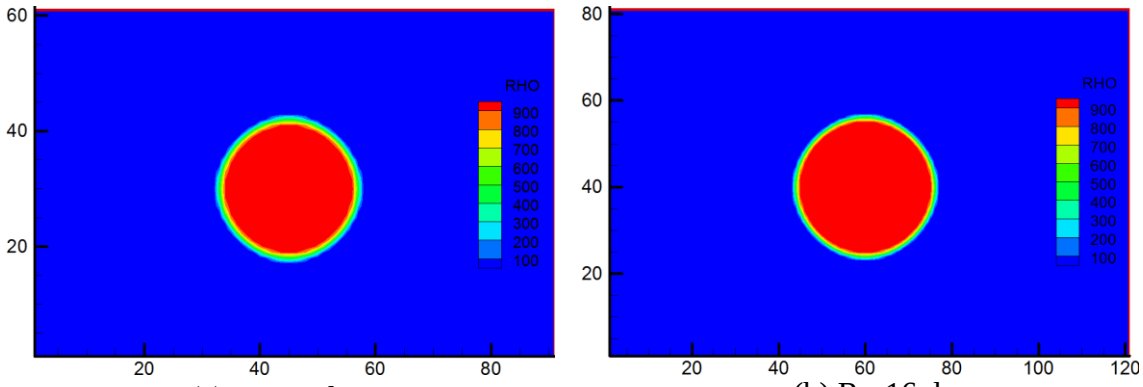

(a) R= 12 dx (b) R= 16 dx

Fig. 4-33 Density distributions without advection effect when initial ϕ_G and ϕ_L are set to their equilibrium values

Fig. 4-28 shows the radius length, shape and volume variation histories when the equilibrium values of the order parameter in the two phases are used as the initial values. By comparison with the diagrams shown in Fig. 4-1, it can be shown that the volume variation coming from the diffusion of the gas phase into the interface to achieve equilibrium between the pressure gradient force and the interface tension force can be greatly reduced. In this case, after the initial diffusion process to form the appropriate interface with suitable density or order parameter distribution and thickness, the volume of the droplet almost remains constant. The same phenomenon can be observed in simulations with the LBM model that removes the advection effect and uses the initial order parameter values in the two phases from the equilibrium state, which is illustrated in Fig. 4-30. Due to the removal of the diffusion of the order parameter in the gas phase to the interface through the use of the equilibrium values in the two phases, the interactions of the advection effect and the diffusion effect in the deformation stagnation stage and the slight shape deformation stage are also eliminated, thus leading to a smaller magnitude of deformation as shown in the comparisons between the Fig. 4-1 and Fig. 4-28, Fig. 4-29 and Fig. 4-30.

Fig. 4-29 and Fig. 4-30 show the radius length, shape, and volume variation histories of a droplet in the LBM model when the equilibrium and the bulk phase values of the order parameter in two phases are used, respectively, without considering the advection effect. Compared with the figures in Fig. 4-1 and Fig. 4-28 where the LBM model keeps its advection term, the shape deformation can be decreased greatly in the quick shape deformation stage. In these cases, the shape deformation arises from the interaction of the diffusion effect of the pressure gradient and the curvature effect of the interface tension force. And the shape deformation coming from the interactions of the diffusion effect and the curvature effect is smaller than that caused by the advection effect.

Moreover, according to the simulation results from the two cases where the advection term in the LBM model is removed, the shape deformation tendencies with the blending factor α and the radius length are totally eliminated, as Fig. 4-32 and Fig. 4-33 show, compared with the simulation results shown in Figs. 1-1 to 1-4 and the Fig. 4-31; in other words, the advection effect is not only the reason the droplet deforms with different blending factors, but also the reason that the droplet deforms with the radius length variations.

4.4 Conclusions

1 The volume variation of the droplet in the simulation is determined by the interactions of the diffusion effect and the curvature effect.

2 The shape deformation is mainly caused by the advection effect of the spurious velocity field and is balanced by the curvature effect of the interface tension force.

3 The numerical error coming from the interactions of the diffusion effect and the curvature effect is also a reason for shape deformation. The droplet deformation arising from this effect is smaller than the one from the advection effect.

4 The droplet deformation tendency with radius changes is also coming from the advection effect.

5 It is possible for the LBM model that removes the advection term to predict the equilibrium or the static problem with better accuracy, due to the removal of the numerical errors from the calculation of the advection term.

5 Appropriate blending factor

According to the analysis conducted in the previous chapters, the advection effect of the spurious velocity is the main cause of shape deformation for the simulations of a static droplet in the gas channel. For the purpose of reducing or eliminating the droplet deformation, the smaller magnitude of the spurious velocity is better. Understanding the mechanism behind the spurious velocity is important for finding the correct way to remove or decrease the spurious velocity.

Among the factors that affect the spurious velocity field, the blending factor, α, of velocity components from the two types of staggered grids adopted in the calculation process of the Poisson-equation-based fractional step method is an important variable that determines the structure and magnitude of the spurious velocity and thus determines the type and degree of the droplet shape deformation. Besides, while the radius is changing, the deformation degree is also changing for the same blending factor value, in order to accurately simulate the droplet behaviors, particularly, the interface tension related phenomena; an appropriate blending factor for each radius is needed.

In this chapter, we will investigate how the blending factor affects the spurious velocity field in the simulation and how to decide the appropriate blending factor for a droplet with varying radius.

5.1 Common origins of the spurious velocity in free-energy-based LBM

The spurious velocity, also referred to as parasitic current, is an artificial velocity with small amplitude, which exists in the vicinity of an interface in the simulation. This artificial velocity field is a common problem in the two-phase flow simulation techniques of diffuse interface methods, such as the LBM, the volume of fluid (VOF), the phase field (PF) and the level set (LS) methods (Ryu and Ko, 2011; Scarbolo, et al., 2012). This artificial velocity field is nonphysical and arises from a slight force imbalance between the discretized forces in the interface region. Its presence not only degrades the simulation accuracy, but may also cause instability problems. Many efforts have been made to reduce or eliminate the spurious velocity and identify its origins in the LBM models, especially, in the free-energy-based LBM models (Wagner, 2003; Lee and Fischer, 2006; Pooley and Furtado, 2008; Seta and Okui, 2007; Chiappini, et al., 2010; Guo, et al., 2011; Connington and Lee, 2012).

From the mathematical standpoint, the treatments of the intermolecular force terms in Eqs. (2-18), (2-21), and (2-23) are the same. Therefore, the calculation of these equations can be divided into two parts: calculation of (1) the gradient of scalar(s) and (2) the gradient of the non-isotropic tensor. Both Wagner (2003) and Lee and Fischer (2006) proved that the truncation error between the two parts is the

origin of the spurious velocity in the free-energy-based LBM model, and it was defined as the incompatible discretization error.

$$F_\alpha^S = \frac{\partial}{\partial x_\alpha}\left(p_0(\lambda) - \kappa\rho\frac{\partial^2\lambda}{\partial x_\alpha^2} - \frac{\kappa}{2}\left(\frac{\partial\lambda}{\partial x_\alpha}\right)^2\right)\delta_{\alpha\beta} + \kappa\frac{\partial}{\partial x_\alpha}\left(\frac{\partial\lambda}{\partial x_\alpha}\frac{\partial\lambda}{\partial x_\beta}\right) \qquad 5\text{-}1$$

Scalar part

Tensor part

Incompatible discretization

Additionally, the anisotropic discretization of the derivatives in the intermolecular force terms is also a source of spurious velocity. It has been found that the magnitude of the spurious velocity can be significantly decreased by computing the derivatives with higher isotropic discretization schemes in the free-energy-based LBM models (Seta and Okui, 2007; Pooley and Furtado, 2008).

5.2 The spurious velocity from the calculation of the Poisson equation

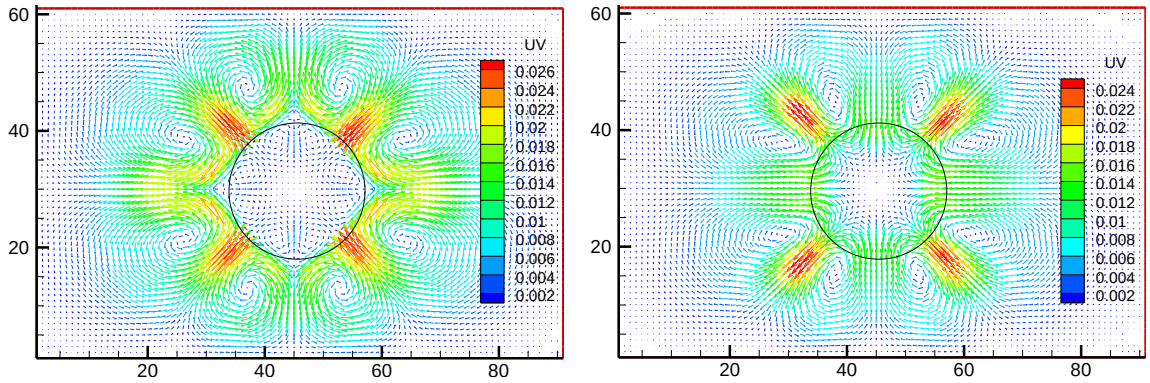

(a) staggered grid 2 (α = 0.0) (b) staggered grid 2 (α = 1.0)

Fig. 5-1 Spurious velocity field in steady state

Focusing on the spurious velocity coming from the implementation of the Poisson-equation-based fractional step method (or the so called projection method); the simulation results of a water droplet with an initial radius of 12 dx are used in this section to remove the effect of radius on the spurious velocity.

The calculation of the hydrodynamic pressure from the Poisson equation by the SOR method with the staggered grids is a new source of spurious velocity. It belongs to the category of anisotropic discretization error. As shown in Fig. 5-1, when different staggered grids are used in the calculation, different types of spurious velocity fields are observed. The Staggered Grid 1 that uses the predicted velocity in the orthogonal directions for the estimation of the p_H creates an orthogonal type of spurious

velocity field. The Staggered Grid 2 that uses the predicted velocity in the diagonal directions creates a diagonal type of spurious velocity field. If the derivatives in the hydrodynamic pressure, p_H (Eq. (5-2)), are calculated through an isotropic discretization scheme, the p_H value should distribute inside and outside the droplet isotropically, as the thermodynamic pressure p_0 in the equation defining p_H can be calculated

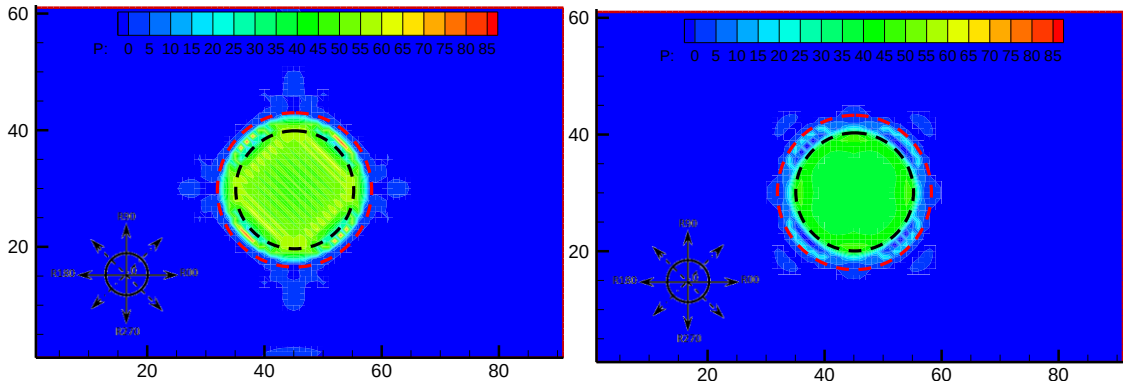

(a) staggered grid 2 (α = 0.0) (b) staggered grid 2 (α = 1.0)

Fig. 5-2 Hydrodynamic pressure field calculated from Eqs. (5-3) and (5-4)

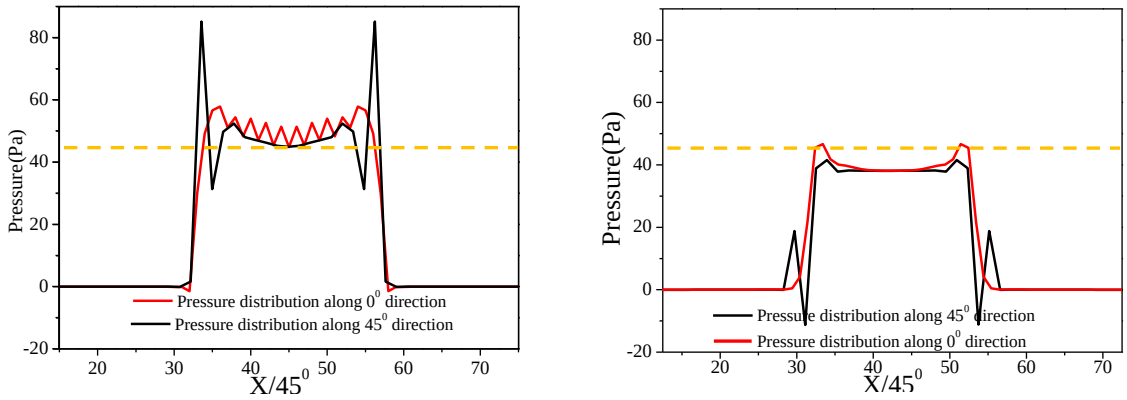

(a) staggered grid 2 (α = 0.0) (b) staggered grid 2 (α = 1.0)

Fig. 5-3 Hydrodynamic pressure distribution along the 0° and 45° directions

without any error by the equation of state (EOS, Eq. (5-5)). Fig. 5-2 shows the hydrodynamic pressure field calculated from Eqs. (5-6) and (5-7), based on the iterative SOR method. In Fig. 5-2, the dotted black line is the iso-surface of $\phi = \phi_L$ or $\rho = \rho_L$, the dotted red line is the iso-surface of $\phi = \phi_G$ or $\rho = \rho_G$, and the region between them is the interface region. Fig. 5-3 shows the corresponding pressure distributions across the center of the simulated droplet along the 0° and 45° directions. In this figure, the dotted yellow line is the expected pressure inside the water droplet, which is predicted from the

Laplace equation. From these figures, it can be seen that in both cases, in the interface region, the distribution of the p_H is anisotropic and the value of the p_H deviates from the theoretical prediction. Such anisotropic distributions are considered to be the source of the spurious velocity around the interface region of the water droplet. Besides, the p_H predicted by using the Staggered Grid 2, distributed in a chalkboard-type configuration in the liquid region, is believed to be the source of small spurious velocity eddies inside the water droplet.

Originally, the hydrodynamic pressure, p_H, was solved from the Poisson equation by Inamuro et al. (2004). This was accomplished in the framework of the LBM scheme with a co-located grid that defined the pressure and the velocity within the same grid point, as also shown in Fig. 2-5. In this case, all the velocity components along all directions (including both diagonal and orthogonal directions) were taken into account. Such treatment makes the predicted p_H to be associated with a better isotropy and accuracy than the corresponding estimates calculated with the staggered grids, discussed earlier.

Adopting the Staggered Grid 1 in the discretization equation of the Poisson equation for the iterative SOR method means that only the velocity components along the orthogonal directions are taken into account. Correspondingly, adopting the Staggered Grid 2, means that only the velocity components along the diagonal directions are considered. In order to increase the isotropy in the calculation process of the hydrodynamic pressure, a possible way is to combine the velocity components from the two types of staggered grids together. The problem that arises, however, relates to the determination of the ratio for each type of the staggered grid employed in the discretization equation of the Poisson equation. As for the Poisson equation solved by the LBM scheme in which the co-location grid is used, the weight ratio of the velocity components used in the calculation along the diagonal and the orthogonal directions is 1/9:1/36. A primary question that arises is whether the same ratio value would be suitable to be used (or not) in the discretization equation for the SOR method for blending velocity components from the two types of staggered grids.

To test this idea, based on the discretization equations (Eqs. (5-8) and (5-9)) used in the SOR iteration with the Staggered Grid 1 and the Staggered Grid 2, the velocity components from the two types of staggered grids are blended together. The definition of the blending factor and the formulation of the hydrodynamic pressure derived from the Poisson equation based on the two types of staggered grids are shown from Eq. (2-61) to Eq. (2-63). In order to obtain the appropriate blending factor that can elicit the most isotropic and the most accurate value of the hydrodynamic pressure, eleven α values are tested ranging from 0.0 to 1.0, with a step interval of 0.1. The choice of $\alpha = 0.0$ corresponds to the case in which

only the Staggered Grid 2 is adopted in the discretization equation of the Poisson equation, whereas α = 1.0

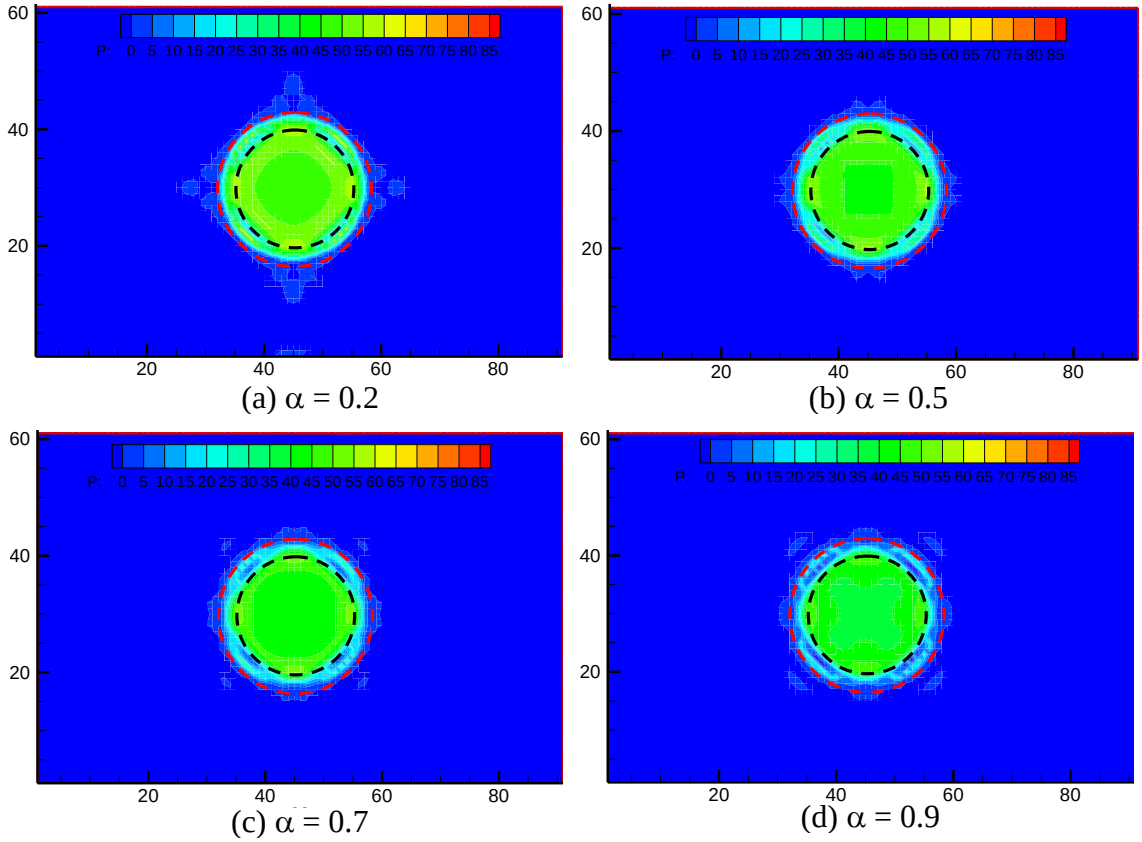

Fig. 5-4 Hydrodynamic pressure fields

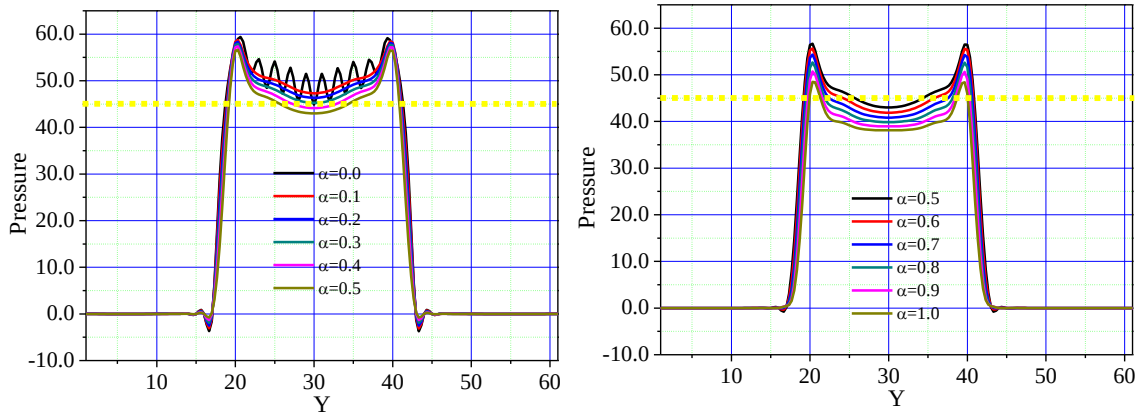

Fig. 5-5 Hydrodynamic pressure distributions across the center of the calculation domain along the y axis

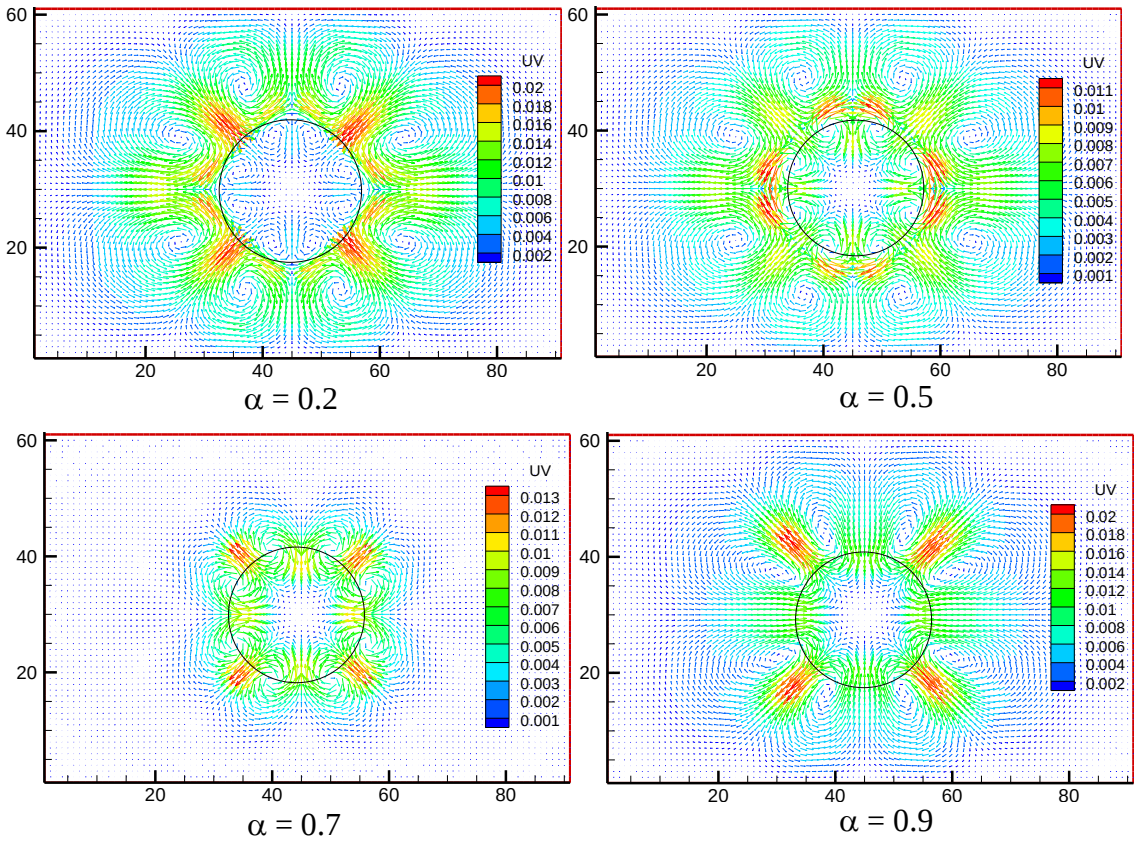

Fig. 5-6 The Spurious velocity fields with typical blending factor α

corresponds to the case in which only the Staggered Grid 1 is adopted. It is found that starting from α =0.0 (or α =1.0) and gradually increasing the ratio of the velocity components in the discretization equation of the Poisson equation from another staggered grid, the predicted hydrodynamic pressure, p_H, becomes more isotropic and accurate. When α =0.5, at which the velocity components in the discretization equations of the Poisson equation from the two types of staggered grids are equally blended, the p_H can attain the most isotropic distribution and the most accurate value, although the anisotropy cannot be totally removed at the interface region of the droplet. Fig. 5-4 shows the predicted p_H field based on the simulation with a selection of different α values. The results of Fig. 5-4, in combination with those of Fig. 5-2, indicate that the isotropy of the p_H increases when α approaches 0.5, irrespective of the starting value (that is, either from 0.0 or from 1.0). Fig. 5-5 shows the predicted hydrodynamic pressure distribution across the center of the calculation domain, along the y direction. From this figure, it is seen that, as a value of α becomes close to around 0.0, the solution tends to predict a higher averaged p_H value inside the water droplet, whereas a corresponding value of α around 1.0 tends to predict a

smaller value. The averaged p_H value inside the droplet can be accurately predicted when α = 0.5. Corresponding to Fig. 5-4, Fig. 5-6 shows the spurious velocity field predicted by different blending factors. In combination with Fig. 5-1, it can be shown that starting from α =0.0 (or α =1.0), the magnitude of the spurious velocity gradually decreases with the increase of contribution from another staggered grid. The predicted hydrodynamic pressure with the smallest anisotropy makes the magnitude of the spurious velocity field the smallest. When α =0.5, (where the contributions from the two types of staggered grids are blended equally), the magnitude of the predicted spurious velocity is decreased to half of its original value. Fig. 5-7 illustrates the typical density distributions which correspond to the spurious velocity fields shown in Fig. 5-6. From these figures, it can be seen that the smallest spurious velocity leads to the smallest shape deformation.

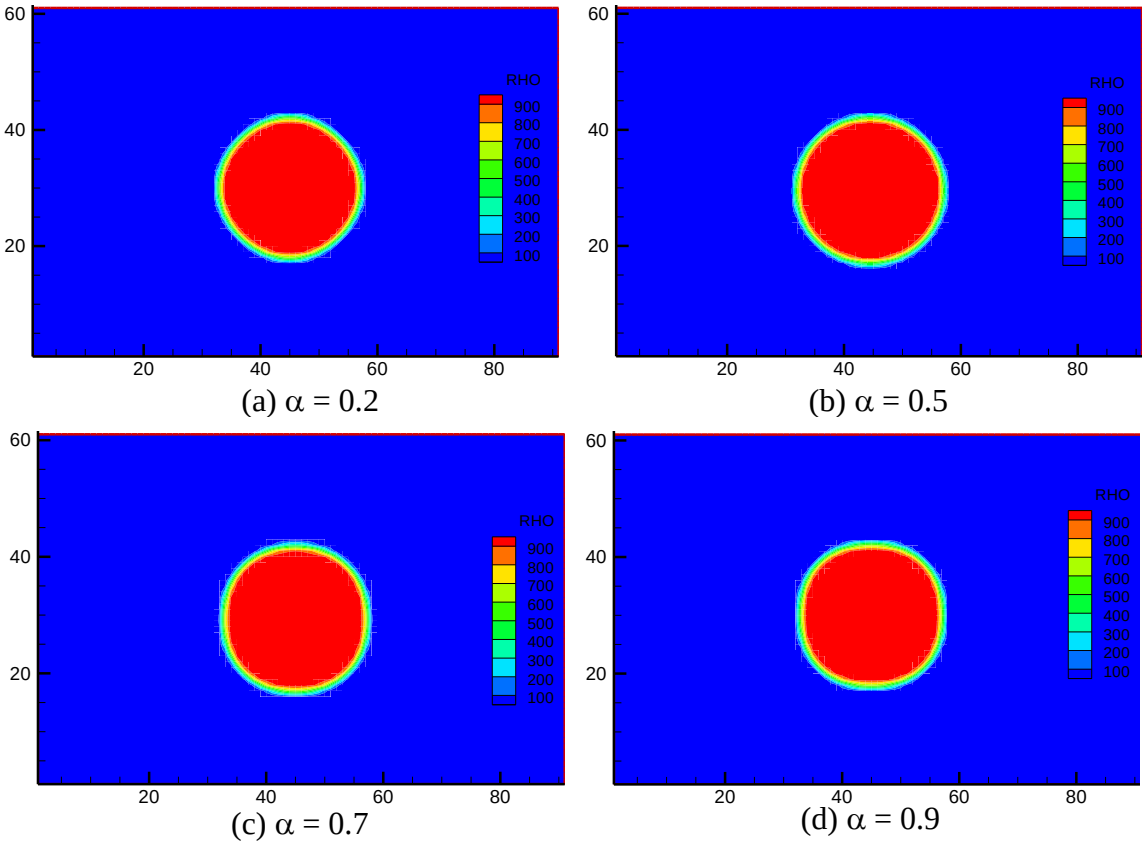

Fig. 5-7 Density distributions with typical blending factor α

5.3 The spurious velocity variation with the droplet radius

As discussed in the last section, an average blending of the velocity components from the two types of staggered grids can preduce a droplet with the smallest shape deformation and the smallest spurious velocity field when its radius is 12 *dx*. However, when different radii are adopted in the simulation, the tendencies observed in the last section change and some special numerical phenomena occur. When the radius lengths of the droplet are small (compared with the cases mentioned in last section), a blending factor α value approaching to 0.0 makes the magnitude of the spurious velocity obviously smaller than that predicted by the α = 1.0; in these small radius length cases, α around 0.5 predicts the smallest magnitude of the spurious velocity. Fig. 5-8 shows examples of the spurious velocity fields predicted by the typical blending factor values with a smaller initial radius length of 6 *dx*.

On the other hand, when the radius lengths of the simulated droplet in the present LBM model are large, gradually with the radius length increases, the magnitude of the spurious velocity predicted by the blending factor α around 0.0 becomes larger and larger; meanwhile, the magnitude of the spurious velocity predicted by the α that is approaching to 1.0 becomes smaller and smaller. Eventually, when the radius length of the droplet becomes large enough, α = 0.0 will predict a spurious velocity field with the largest magnitude compared to other blending factors used in the simulation with the same radius length, and α = 1.0 will predict the smallest magnitude of the spurious velocity. At this moment, the magnitude of the predicted spurious velocity will gradually decrease as the α varies from 0.0 to 1.0. Fig. 5-9 is a corresponding example, where the spurious velocity fields of a water droplet with a large radius length (20 *dx*) and the typical blending factor α values adopted in the simulation are illustrated.

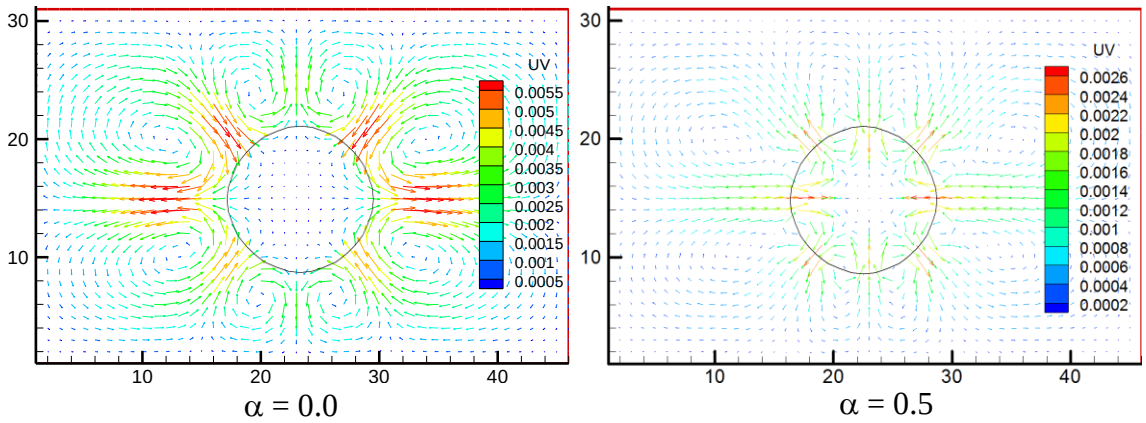

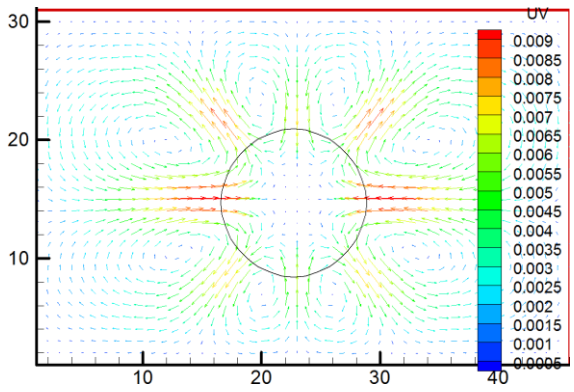

α = 1.0

Fig. 5-8 Typical spurious velocity fields when the initial radius is 6 *dx*

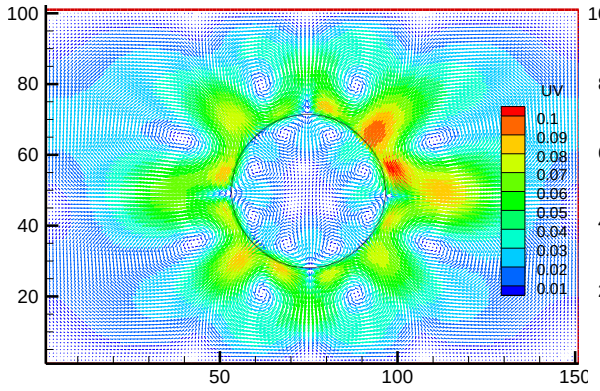

α = 0.0

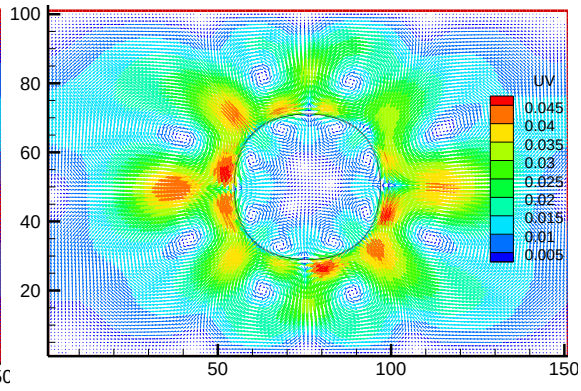

α = 0.5

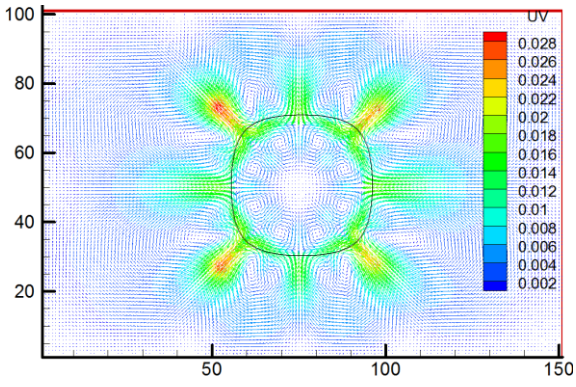

α = 1.0

Fig. 5-9 Typical spurious velocity fields when the initial radius is 20 *dx*

The black circles shown in Fig. 5-8 and Fig. 5-9 are the corresponding shapes of the droplets in the case of each blending factor α value. The spurious velocity is believed to come from the imbalance of the discretized intermolecular forces in the interface region; thus, large spurious velocity leads to large

deviation from equilibrium, and thus large shape deformation. But in these figures, particularly in cases of large radius length, the larger spurious velocity corresponds to the smaller shape deformation, and smaller spurious velocity corresponds to the larger shape deformation.

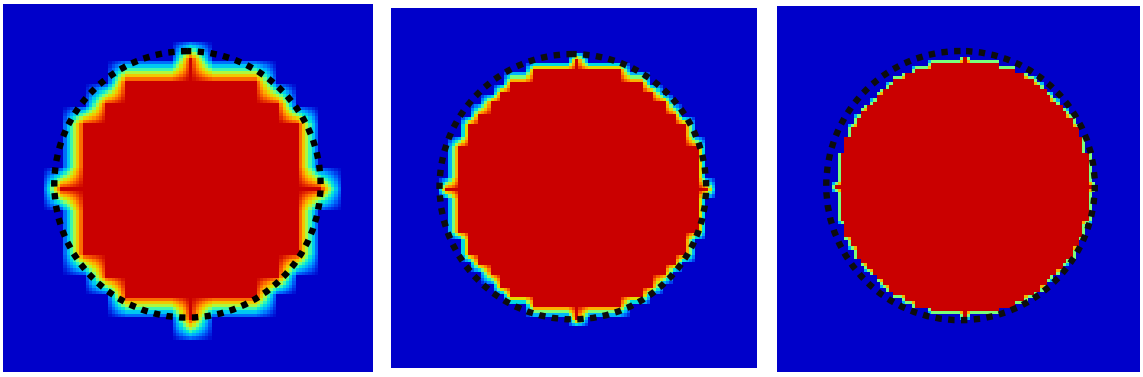

(a) R = 6 dx (b) R = 12 dx (c) R = 20 dx

Fig. 5-10 Initial order parameter assignments in two phases with typical radii

A reasonable explanation of these strange numerical phenomena is given in the following part. As discussed in Chapter 4, the droplet shape deformation mainly occurs in the second stage of the unsteady stage, where the rapid shape deformation happenes. The rapid shape deformation stage can be divided into two sub-stages. In the first sub-stage, the over-shot order parameter ϕ in the liquid phase diffuses outward by the pressure gradient, such that the volume of the droplet expands outwards; meanwhile the advection effect of the spurious velocity starts to drive the droplet to deform along the directions of the spurious velocity vectors. During this sub-stage, the diffusion process is affected by the initial assignment of the liquid phase lattice points along the interface, and such an assignment is determined by the initial radius length. The initial order parameter assignments in two phases of a droplet with radius length of 6 dx, 12 dx and 20 dx are considered as the examples, as illustrated in Fig. 5-10, which are the examples of droplet with small radius length, middle radius length and large radius length, respectively. For the droplets with small radii, as the shown in Fig. 5-10 (a), the number of liquid phase lattice points along the interface region in the orthogonal directions is more than in the diagonal directions; when the overshot ϕ in the center of the droplet diffuses outward through these points, more order parameter ϕ is diffused into the interface region in the orthogonal directions than in the diagonal directions. So the interface curvature of the droplet in the orthogonal directions is increased, and meanwhile, the interface curvature in the diagonal directions is decreased, as illustrated in Fig. 5-14. The increased curvature in the orthogonal directions will create an additional inward interfacial tension force, thus an additional inward velocity component; the decreased curvature in the diagonal directions will make an

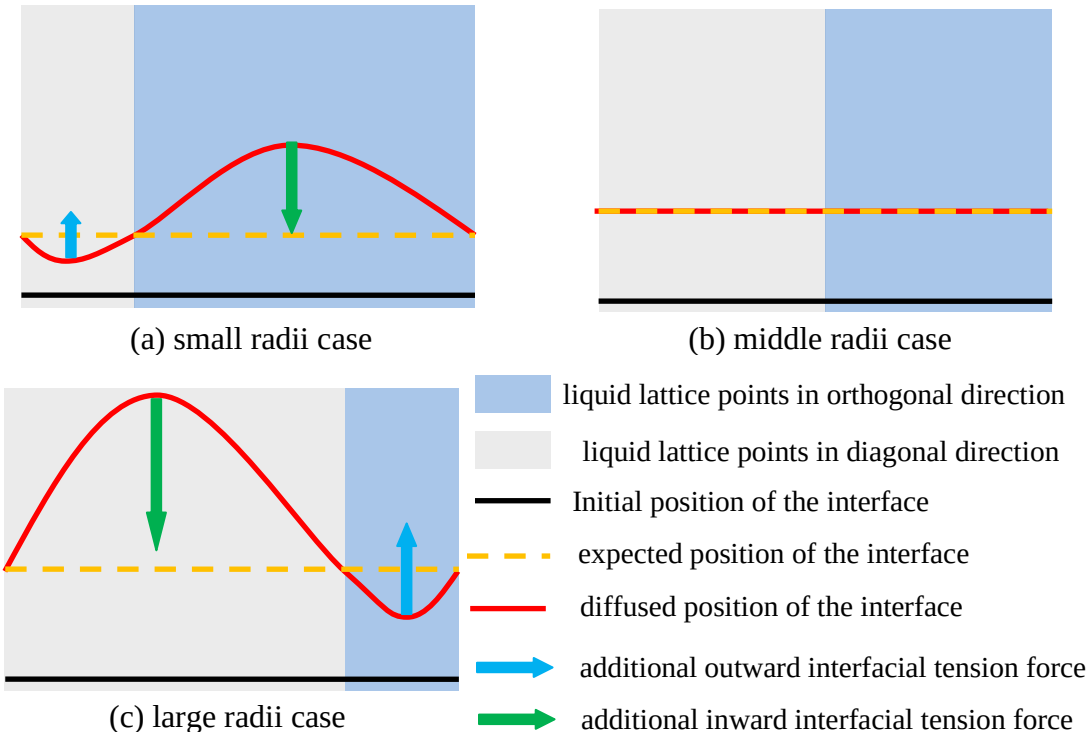

Fig. 5-11 Interface evolution due to the diffusion effect

additional outward velocity component. For the droplets with medium radii, as the shown in Fig. 5-10 (b), the number of liquid phase lattice points along the interface region in the orthogonal directions is almost the same as in the diagonal directions. When the interface diffuses outward, the curvatures in both the orthogonal and diagonal directions keep the same variation ratio with no additional interfacial tension force created, and thus no additional velocity components arise in the interface region. When the radius further increases, for the droplets with large radius length, as the shown in Fig. 5-10 (c), the number of liquid phase lattice points along the interface region in the diagonal directions becomes greater than the number of liquid phase lattice points in the orthogonal directions. When the overshot ϕ in the center of the droplet diffuses outward, more overshot ϕ is diffused into the interface region in the diagonal directions than in the orthogonal directions, and thus the interface curvature of the droplet in the diagonal directions is increased, and meanwhile, the interface curvature in the orthogonal directions is decreased. Correspondingly, the increased curvature in the diagonal directions will create an additional inward interfacial tension force, and thus an additional inward velocity component; the decreased curvature in the orthogonal directions will make an additional outward velocity component. In the large radius length cases, due to the larger number of liquid phase lattice points in the interface region, the magnitude of the overshot ϕ is larger than in the smaller radius length cases; when the overshot ϕ diffuses outward, it

should induce larger volume expansion and shape deformation, and further larger additional velocity component from the curvature effect.

Fig. 5-12, Fig. 5-13 and Fig. 5-14, are the corresponding hydrodynamic pressure fields predicted from the Poisson equation with typical blending factors; from these figures, we can see that the spatial distribution of the hydrodynamic pressure field from each blending factor is independent of the radius variation, although, the pressure gradient in the interface region increases along with the increase of the dimensionless radius length. Besides, the pressure differences in the interface region among the typical

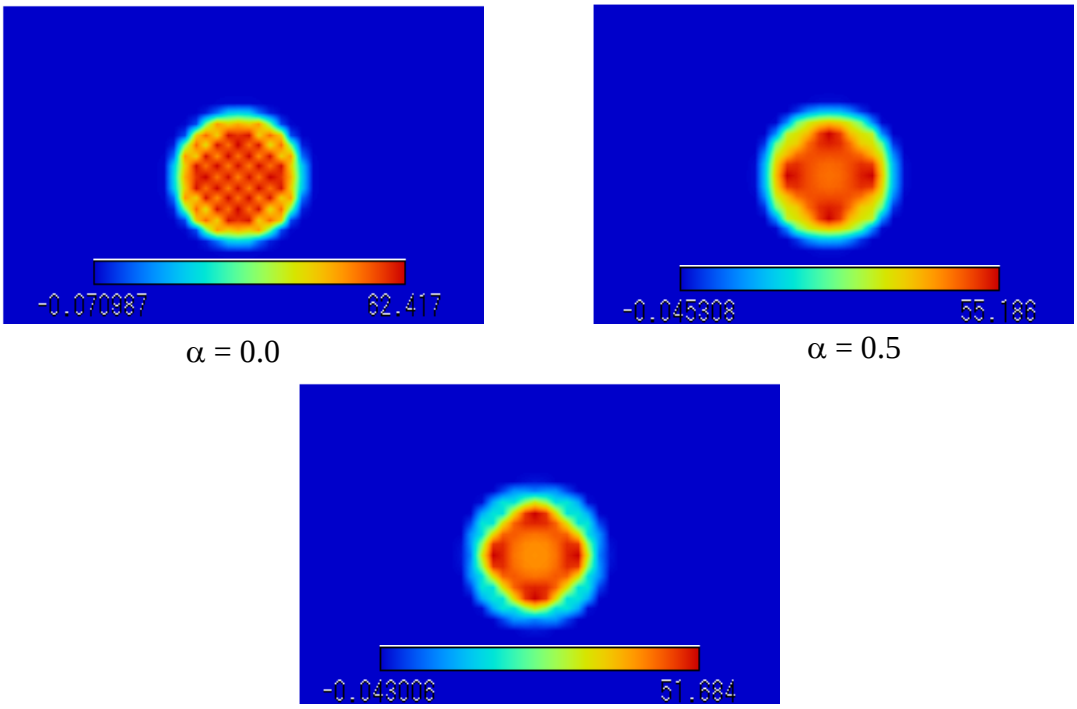

α = 0.0 α = 0.5

α = 1.0

Fig. 5-12 Typical hydrodynamic pressure fields when the radius is 6 dx

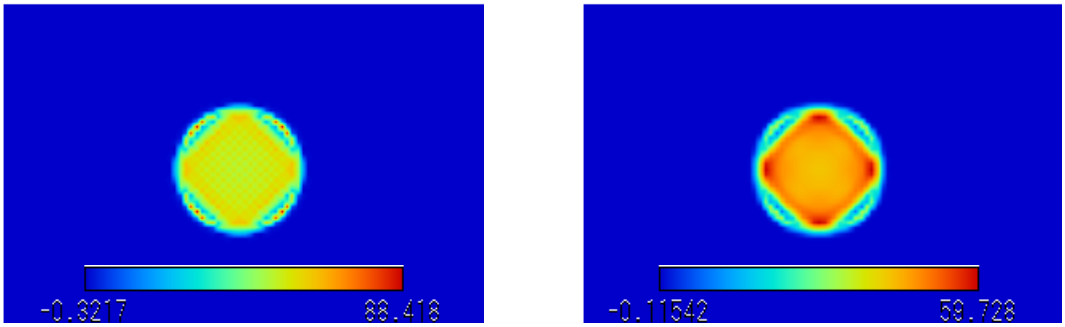

α = 0.0 α = 0.5

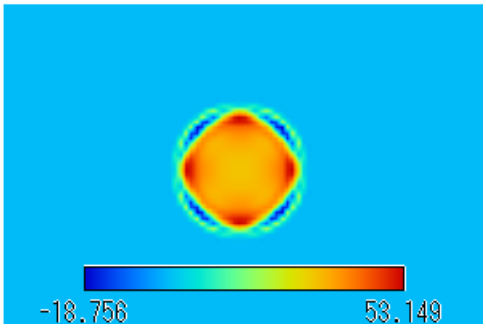

α = 1.0

Fig. 5-13 Typical hydrodynamic pressure fields when the radius is 12 dx

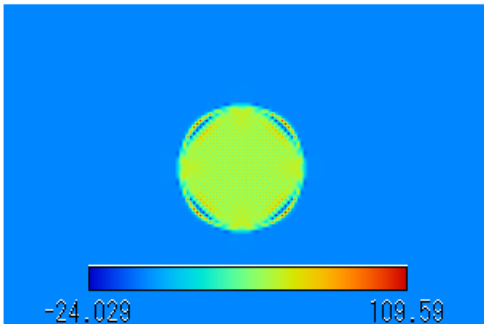

α = 0.0

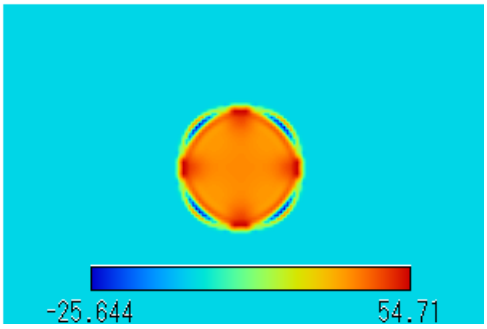

α = 0.5

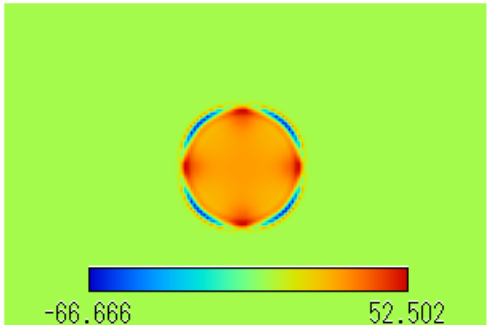

α = 1.0

Fig. 5-14 Typical hydrodynamic pressure fields when the radius is 20 dx

blending factors almost keep the same ratio for each radius length case. Thus, it is persuasive that in each radius case, the velocity predicted by the hydrodynamic pressure gradient in the interface region keeps the same ratio among the different blending factors. When the blending factor α = 0.0 is used, due to the anisotropic discretization error, the calculated hydrodynamic pressure gradient force tends to predict a velocity field that is flowing inward the droplet along the diagonal directions and outward long the orthogonal directions in the interface region; when α = 1.0 is used, the calculated hydrodynamic pressure gradient force tends to predict a velocity field that flows oppositely. Together with Fig. 5-3, in both the α

=0.0 and α = 1.0 cases, the pressure variations along the diagonal directions are obviously larger than along the orthogonal directions, thus the induced spurious velocity in the diagonal directions should be distinctly larger than in the orthogonal directions. The α = 0.0 will create an inward velocity component along the diagonal directions and the α = 1.0 will create an outward velocity component along the diagonal directions.

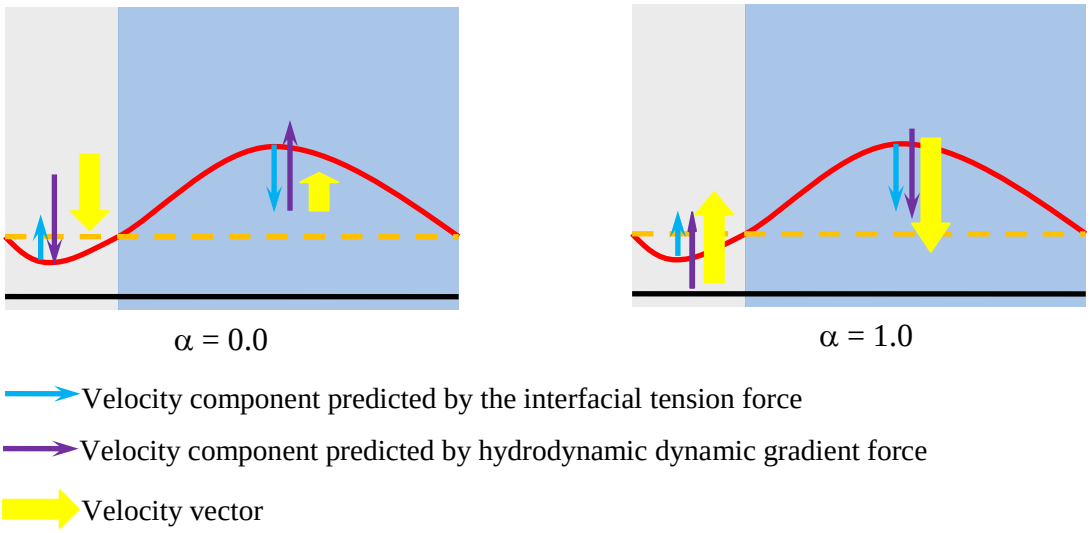

Fig. 5-15 Velocity composition in small radius cases

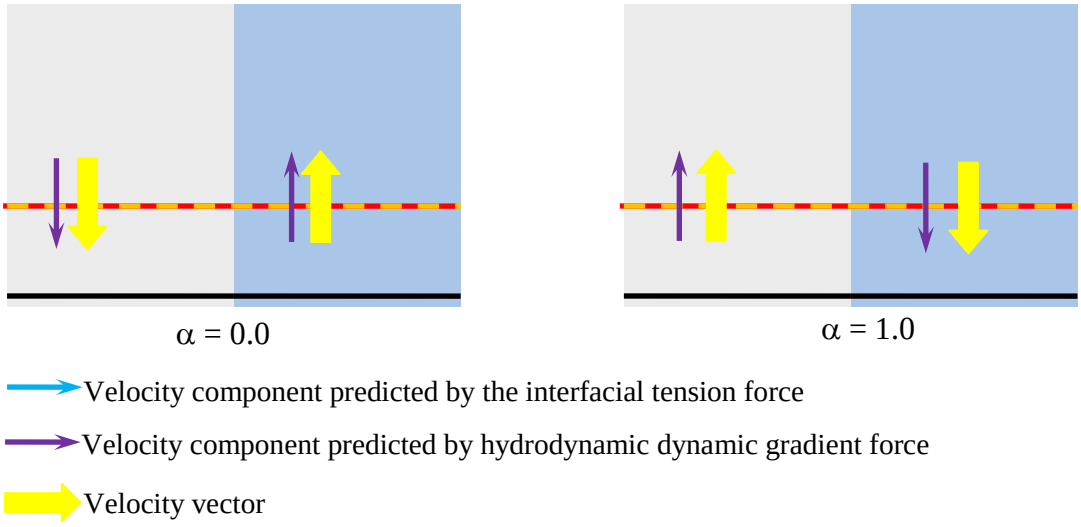

Fig. 5-16 Velocity composition in middle radius cases

For the droplets with small radii, as shown in Fig. 5-15, in the first sub-stage of the rapid shape deformation stage, due to the curvature variations arising from the diffusion of the overshot ϕ in the liquid

phase, the velocity component predicted by the additional interface tension force in the orthogonal directions is larger than in the diagonal directions. Meanwhile, the velocity component predicted by the additional hydrodynamic pressure gradient force (because of the anisotropic discretization error in solving the Poisson-equation-based fractional step method or the so called projection method) is always larger in the diagonal directions than in the orthogonal directions, but with the opposite directions when the blending factor α = 0.0 and 1.0. Thus, the magnitude of the total spurious velocity vector predicted by the two types of the velocity components is larger when in the case of α = 1.0 than in the case of α = 0.0. Besides, due to the limited number of liquid phase lattice points along the interface region, the spurious velocity component from the additional interface tension force is small; thus, enforcement of the two velocity components is small when the blending factor α is around 0.5. So in these cases, the blending factors in the middle range still predict the smallest magnitude of spurious velocity.

For the droplets with the middle radii, as shown in Fig. 5-16, curvature variations coming from the diffusion of the overshot ϕ in the liquid phase keep the same level in both the orthogonal and the diagonal directions, and there is very small or almost no spurious velocity component coming from the additional interface tension force. In these cases, the magnitude of the total spurious velocity is mainly determined by the spurious velocity coming from the anisotropic discretization of the Poisson equation for the calculation of the hydrodynamic pressure. Thus, in this case, total spurious velocity in the α = 0.0 and α = 1.0 cases keeps the same level, and the blending factor approaching to 0.5 results in the smaller spurious velocity.

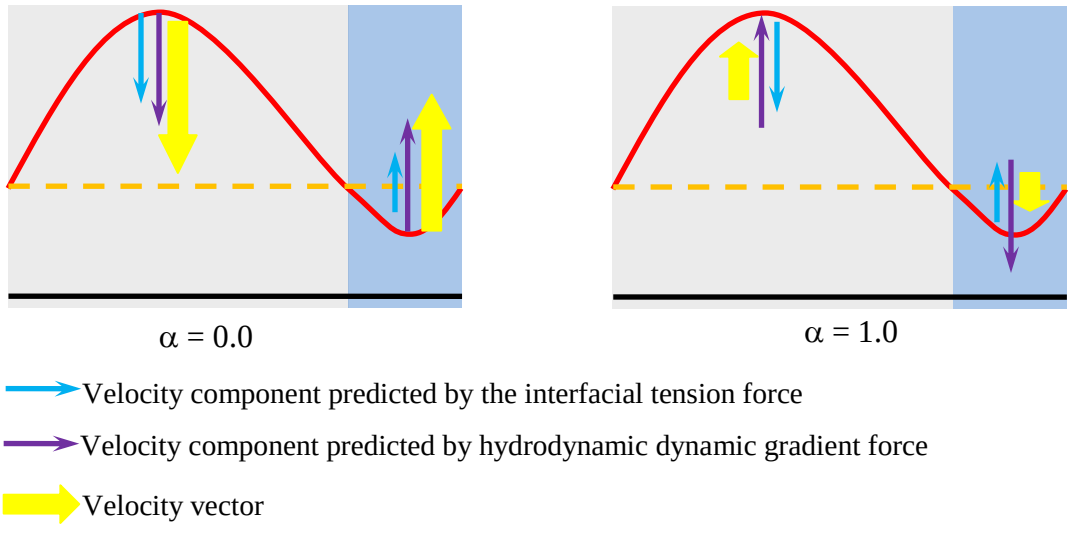

Fig. 5-17 Velocity composition in large radius cases

For the droplets with large radii, as shown in Fig. 5-17, in the first sub-stage of the rapid shape deformation stage, the additional interface tension force arising from the curvature variation is larger in the diagonal directions than in the orthogonal directions, and thus the corresponding the velocity components the orthogonal directions are larger than that in the diagonal directions. The same as the cases in the small and middle radius length cases, that in the blending factor α = 0.0 case, the velocity components from the additional hydrodynamic pressure gradient force are flowing inward the droplet along the diagonal directions and outward along the orthogonal directions; and in the case of α = 1.0, the velocity components from the additional hydrodynamic pressure gradient force flow in the opposite directions. So in these large radius length cases, the total magnitude of the spurious velocity vector predicted from the two components is larger in the case of α = 0.0 than in the case of α = 1.0. For the cases of middle blending factor α values, where the velocity component from the additional hydrodynamic pressure gradient force is small, the total velocity vector is mainly decided by the additional interface tension force, and due to large lattice points in liquid phase in the interface region, the over shot ϕ is much larger than smaller radius length cases. Thus the curvature variation in the two directions is much larger. The large curvature variation will create a much larger additional interface tension force that leading to larger spurious velocity component. That is the reason even if in the case of blending factor α around 0.5 in the large radius length cases, the total magnitude of spurious velocity is larger than in the case of blending factor α = 1.0.

5.4 The appropriate blending factor

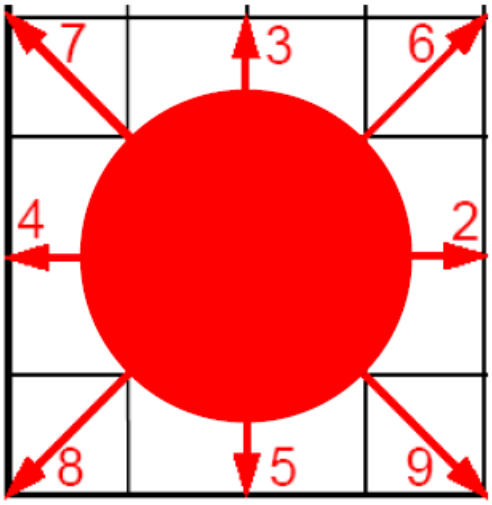

Fig. 5-18 Directions along which the droplet radius is measured

From the discussions in the Chapter 4, we can find that the advection effect of the spurious velocity drives the deformation of the droplet. From the discussions in the last section, we can see that the magnitude of the spurious velocity is affected by the interactions of the additional curvature effect of interface (which is caused by the overshot ϕ in the liquid phase diffusing outward to expand the droplet volume); and the anisotropic discretization error in the calculation of the hydrodynamic pressure. As the additional curvature effect of interface is determined by the initial radius length through the initial assignment of the liquid phase lattice points in the interface region; the appropriate blending factor α that leading to the smallest deformation becomes dependent on the radius.

In order to acquire the appropriate blending factor of the two types of staggered grids for each radius length case that produces the smallest deformation, the droplets with radii ranging from 6 *dx* to 24 *dx* are simulated with 11 blending factor α, ranging from 0.0 to 1.0 with a constant step interval of 0.1. The droplet deformation degree is evaluated by measuring radii in eight directions, as shown in Fig. 5-18, when the simulation reached the steady stage. The radius is defined as the distance from the center of the droplet to the water/gas interface iso-surface where its density is the average value of the densities of liquid water and gas. The relative degree of deformation is taken as the ratio of the largest length difference among the radii of the simulated water droplet and its initial radius.

From the simulation results, we find that the effect of the blending factor α on the shape deformation of a water droplet can be divided into three sections, which is also the criteria in the last section we divided the range of radius for the purpose of analyzing the spurious velocity variation with the droplet radius, as shown in Fig. 5-19. For a water droplet with initial radius ≤ 9 *dx* [defined as 'Section 1' or the small radius cases, and shown in Fig. 5-19 (a)], the blending factor α approaching 0.0 leads to an increase in the degree of shape deformation whereas the α approaching 1.0 minimizes the shape deformation of the water droplet.

For a water droplet with the initial radius in the range of 10 to 18 *dx* [defined as 'Section 2' or middle radius length cases, and shown in Fig. 5-19 (b)], an α value that near 0.0 maintains the same magnitude for the degree of shape deformation as in Section 1; however, the α values approaching 1.0 lead to increasing degrees of shape deformation. The α that gives the best description of the shape of a water droplet in this Section is in the range of 0.1 to 0.5 and it decreases from 0.5 to 0.1 with the increases of the initial radius of the water droplet.

For a water droplet with the initial radius of more than 18 *dx* [defined as 'Section 3' or the large radius length cases, and shown in Fig. 5-19 (c)], the shape deformation degree of a water droplet increases as

the α increases from 0.0 to 1.0, and the appropriate α in this Section is 0.0. Unlike Sections 1 and 2, the degree of shape deformation in Section 3 is smaller when the α is around 0.0. Overall, from Fig. 5-19 (a), (b), and (c), we find that the average degree of shape deformation increases with the increase of the initial radius of the water droplet when the value of α approaches 1.0.

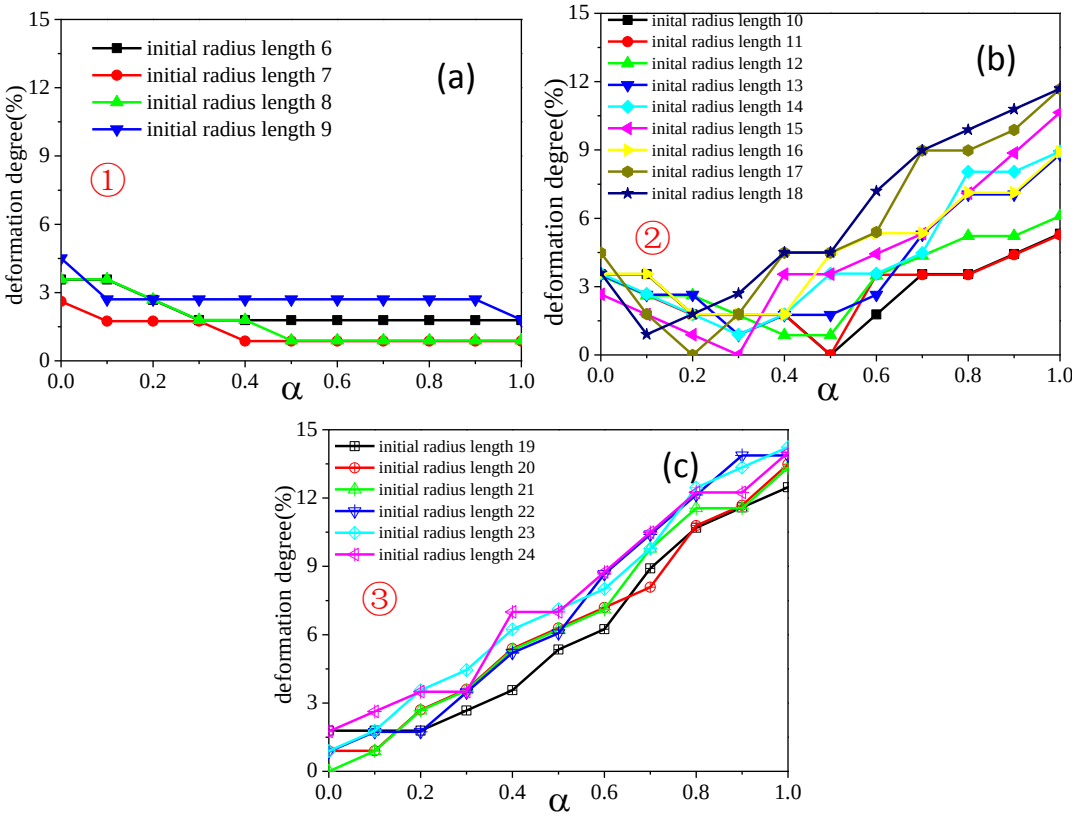

Fig. 5-19 The effects of blending factor α on the shape deformation degree of a water droplet with various initial radii

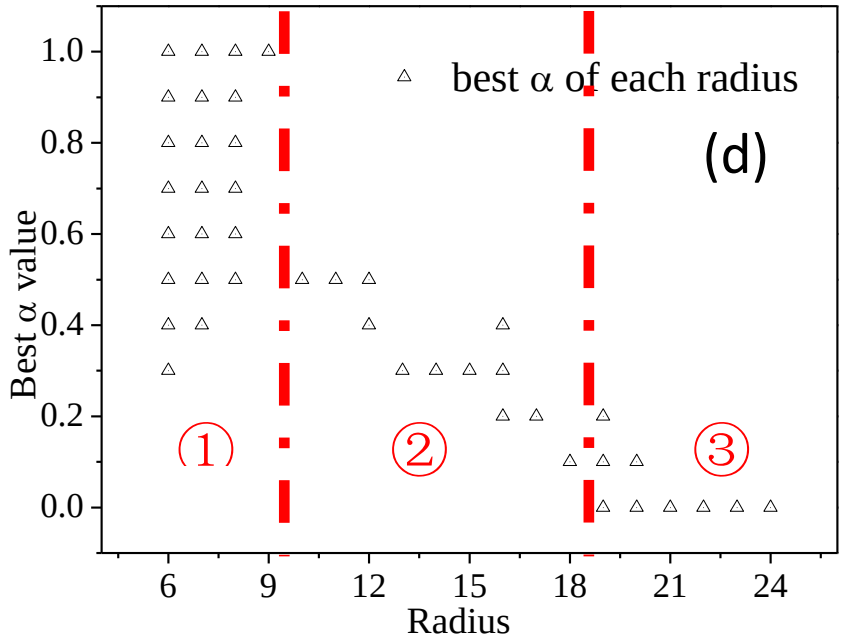

Fig. 5-20 The appropriate blending factor α for each radius

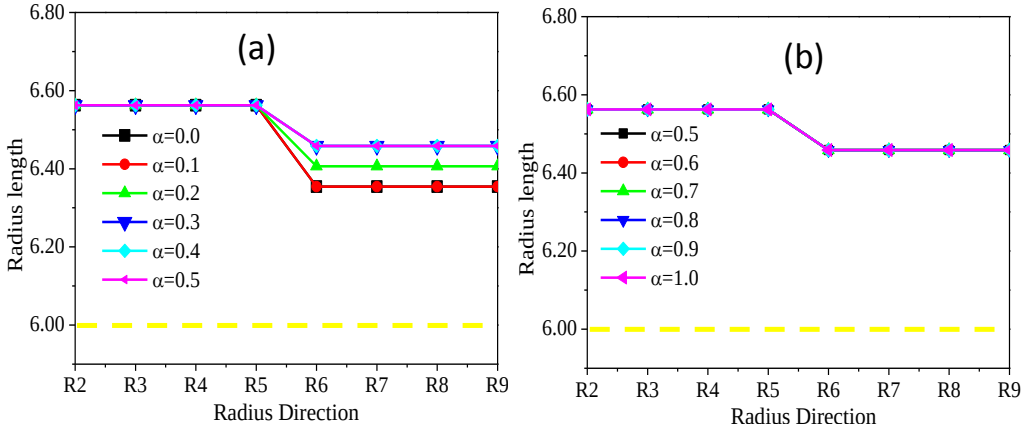

Fig. 5-21 Radius distribution of a droplet with an initial radius of 6 *dx*

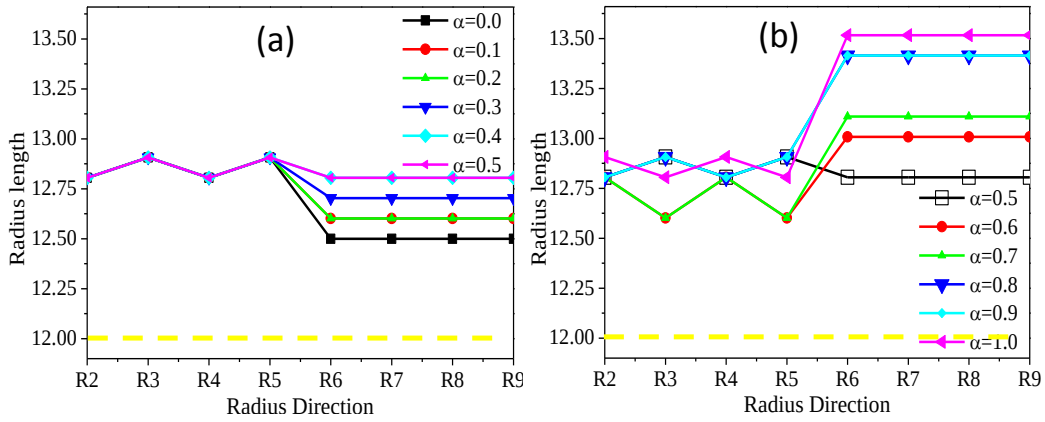

Fig. 5-22 Radius distribution of a droplet an initial radius of 12 *dx*

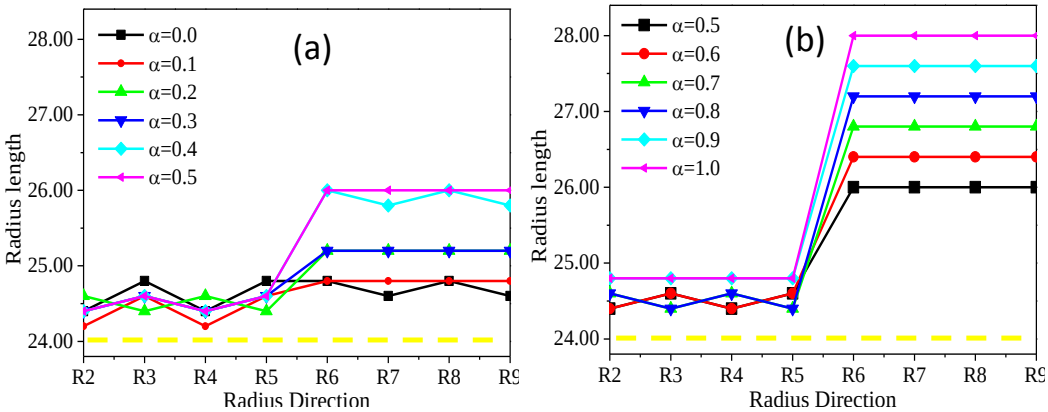

Fig. 5-23 Radius distribution of a droplet an initial radius of 24 *dx*

For the purpose of accurate shape description, appropriate values of the blending factor α for a water droplet with various initial radii are summarized in Fig. 5-20 according to Fig. 5-19 (a), (b) and (c). Fig. 5-21, Fig. 5-22, and Fig. 5-23 separately show typical distributions of the radius in eight directions as measured at the steady stage for a water droplet with the typical initial radii in Fig. 5-19 (a), (b), and (c), respectively, subjected to the effects of various values of the α. In these figures, each of the symbols R2–R9 represents the radius of a droplet in a different direction, as shown in Fig. 5-18, and the yellow dotted lines are their initial radius.

From these figures, we can see that, for a water droplet with an initial radius in Section 1 (small radius length cases), an α approaching 0.0 causes the measured radii in directions 2, 3, 4, and 5 (the orthogonal directions) to be larger than those in directions 6, 7, 8, and 9 (the diagonal directions), whereas the α approaching 1.0 reduces this difference in radius. Fig. 5-24 shows the corresponding shapes of a water

droplet at various representative α values; the deformations caused by adopting different values of α are small in Section 1, and all values of α produce diamond-shaped droplets.

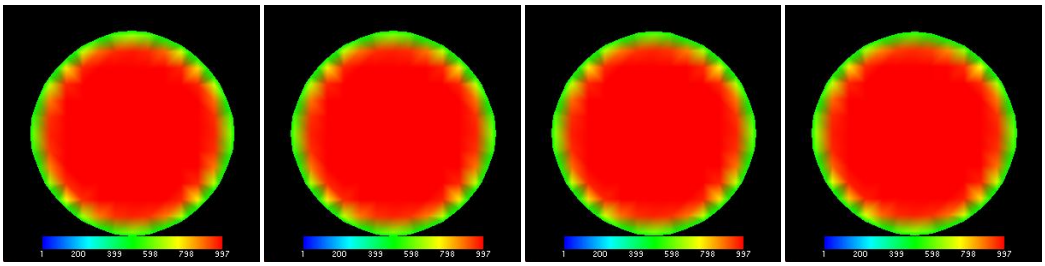

(a) α = 0.0 (b) α = 0.3 (c) α = 0.7 (d) α = 1.0

Fig. 5-24 Typical shapes of a droplet with an initial radius of 6 *dx*

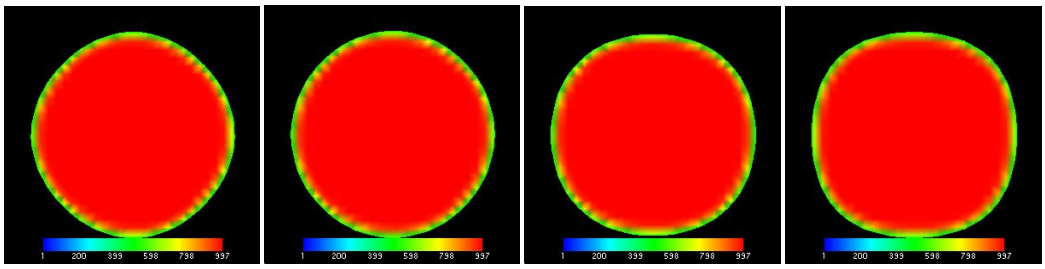

(a) α = 0.0 (b) α = 0.3 (c) α = 0.7 (d) α = 1.0

Fig. 5-25 Typical shapes of a droplet with an initial radius of 12 *dx*

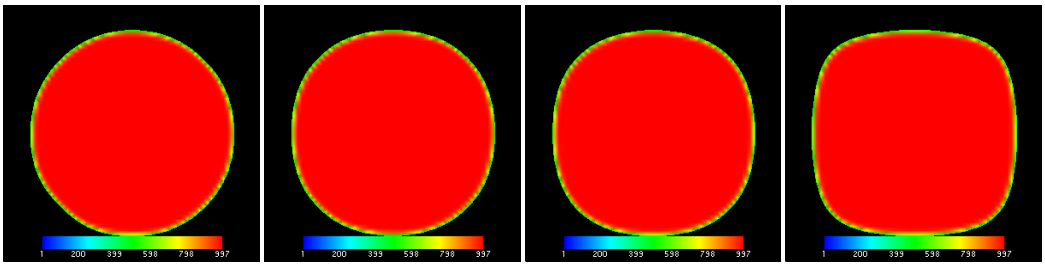

(a) α = 0.0 (b) α = 0.3 (c) α = 0.7 (d) α = 1.0

Fig. 5-26 Typical shapes of a droplet with an initial radius of 24 *dx*

For a water droplet with an initial radius in Section 2 (middle radius length cases), the blending factor α near 0.0 makes the measured radii in orthogonal directions larger than in those in the diagonal directions; the α near 1.0 leads to the reverse effect. Values of the α in the middle result in the simulated radii that are almost equal in all directions. Fig. 5-22 shows the radius distribution of a water droplet with an initial radius of 12 *dx*, which is taken as an example of cases in Section 2; Fig. 5-25 shows the

corresponding shapes of various representative α values. A value of α approaching 0.0 makes the droplet more diamond-like, a value of α approaching to 1.0 makes the droplet more rectangular, and a medium value of the α makes the droplet more spherical.

For a water droplet with an initial radius in Section 3 (large radius length cases), values of α from 0.0 to 1.0 cause the measured radii in directions 6, 7, 8, and 9 (diagonal directions) to exceed those in directions 2, 3, 4, and 5 (orthogonal directions), and these differences increase with increasing values of the α. Fig. 5-23 shows the radius distribution of a water droplet with an initial radius of 24 *dx*, which is an example of cases in Section 3, and Fig. 5-26 shows the corresponding simulated shapes for representative values of α. The blending factor α approaching 0.0 makes the droplet more spherical, and the α approaching 1.0 leads to an increasingly rectangular shape.

In Fig. 5-24, Fig. 5-25 and Fig. 5-26, the black region is the gas phase and the red region is the liquid phase, the colorful region is the interface region and the iso-surface with the averaged density of liquid water and gas is set as the boundary of the interface.

5.5 Conclusions

1 The anisotropic discretization error arising from the calculation of the hydrodynamic pressure and the consequent velocity modification from the Poisson-equation-based fractional step method is a new source of the spurious velocity in the free-energy-based two-phase flow LBM model for large density ratio.

2 The anisotropic discretization error in the fractional step method can be reduced by averagely blending two types of staggered grids, one of which makes use of the velocity components in the orthogonal directions and the other in the diagonal directions.

3 The spurious velocity variation with the radius length is believed to come from the curvature variation difference along the orthogonal and diagonal directions during the process of the overshot ϕ in the liquid phase diffuse to the interface.

4 The appropriate value of the blending factor α used to predict the best shape can be divided into 3 cases, according to the radius variation. For small radius length cases, the blending factor $\alpha = 1.0$ predicts the best shapes; for the middle radius length cases, the α in the middle of 0.0 and 1.0 makes the deformation smallest; for the large radius length cases, the α around 0.0 makes the best shape.

6 The spurious velocity from the cut-off and magnification equation

The existence of the spurious velocity is harmful, as it prevents the two-phase system from achieving a true equilibrium state; it is also difficult to distinguish the physical velocity from the spurious velocity; when the magnitude of the spurious velocity is large, it even leads to severe instability. In Chapter 4, we proved that the spurious velocity in the present model is the main "driving force" behind the deformation of the simulated droplet. In the Chapter 5, we proved that anisotropic discretization error in the calculation process of the Poisson-equation-based fractional step method is a source of the spurious velocity, which can be reduced by improving the isotropy of the derivative schemes in the Poisson equation. In order to further reduce the magnitude of the spurious velocity in the present model, we will investigate the other new origins of the spurious velocity and find new ways to remove or reduce their contributions.

As discussed in Chapter 1, the two-phase system described by the order parameter ϕ can only deal with density ratios around 10:1. A heuristic treatment that uses the cut-off and magnification equation to realize large density ratios around 1000: 1 is needed. Such a treatment may break the force balance around the curved interface. So in this chapter, we are going to prove that the cut-off and magnification equation is the source of another type of the spurious velocity; moreover, we will reduce its contributions to the total magnitude of the spurious velocity.

6.1 Cut-off effect

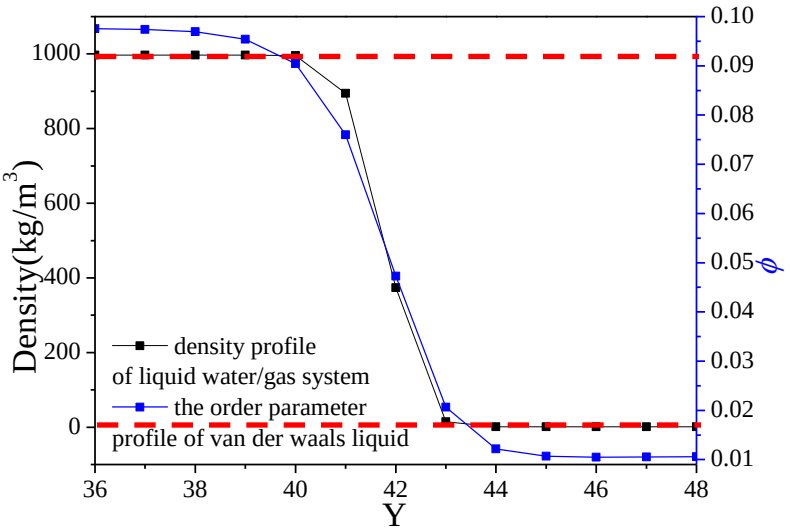

Fig. 6-1 Profiles of ϕ and ρ across the interface

Fig. 6-1 shows the order parameter ϕ and the density ρ distributions along the cross section of a droplet in the y direction. The red dotted lines are the cut-off threshold values for the liquid and gas phases. In the present model, the distribution of ρ is calculated through the cut-off and magnification equation based on the order parameter distribution, as:

$$\rho = \begin{cases} \rho_G, & \phi \le \phi_G \\ \dfrac{\Delta\rho}{2}\left[\sin\left(\dfrac{\phi-\bar{\phi}}{\Delta\phi}\pi\right)+1\right]+\rho_G, & \phi_G < \phi < \phi_L \\ \rho_L, & \phi \ge \phi_L \end{cases} \qquad 6\text{-}1$$

The derivatives, in the intermolecular force as shown in Eqs. (2-18), (2-23) and (2-33), are calculated based on the density, ρ, distribution. As shown in Eq. (6-1) and Fig. 6-1, the density, ρ, distribution is non-continuous around the threshold values that are used to distinguish the two phases and the interface region. In the interface of the liquid water and the gas, the density gradient changes sharply among the limited grid numbers, so it is inappropriate to directly calculate the derivatives from the density, ρ, distribution with the following schemes:

$$\frac{\partial\rho}{\partial x_\alpha} \approx \frac{1}{6\Delta x}\sum_{i=2}^{9} c_{i\alpha}\rho\left(x + c_i\Delta x\right) \qquad 6\text{-}2$$

Because the ϕ profile varies smoothly across the interface, the derivatives of ρ can be appropriately approximated based on the ϕ distribution. Take the derivative operation on both sides of the Eq. (6-1), as shown in Eq. (6-3),

$$\frac{\partial\rho}{\partial x_\alpha} = \begin{cases} 0, & \phi \le \phi_G \\ \dfrac{\Delta\rho}{2}\cdot\dfrac{\pi}{\Delta\phi}\cdot\dfrac{\partial\phi}{\partial x_\alpha}\cos\left(\dfrac{\phi-\bar{\phi}}{\Delta\phi}\pi\right)+\rho_G, & \phi_G < \phi < \phi_L \\ 0, & \phi \ge \phi_L \end{cases} \qquad 6\text{-}3$$

The derivative of the density ρ can be calculated indirectly from the order parameter ϕ's derivative; thus the newly calculated ρ derivative varies smoothly around the threshold values. With this type of treatment, Tabe et al. (2007) stabilized the simulation and greatly decreased the predicted magnitude of the spurious velocity. Following their instructions, we compare the simulation results from the two treatments. Fig. 6-2 and Fig. 6-3 are the spurious velocity fields predicted with typical blending factor α values when the derivative of ρ is calculated from Eq. (6-2) and Eq. (6-3), respectively. The simulation results prove that

with Tabe's improvement, the variation of density, ρ, along the cross sectional profile of the interface around the cut-off threshold values becomes smooth; the spurious velocity coming from discontinuities in the profile can be reduced greatly. The magnitude of the spurious velocity can be reduced by about one order. Meanwhile, due to the large magnitude of spurious velocity in the original model (calculated with the scheme shown in Eq. (6-2)), in these cases, it is difficult to obtain stabilized simulation results, and the shape of the droplet is continuously changing. As shown in Fig. 6-5 and Fig. 6-5, the predicted droplet shape deforms more strongly than these stabilized simulation results with Eq.(6-3), which are shown in Fig. 6-3, Fig. 6-4 and Fig. 6-6.

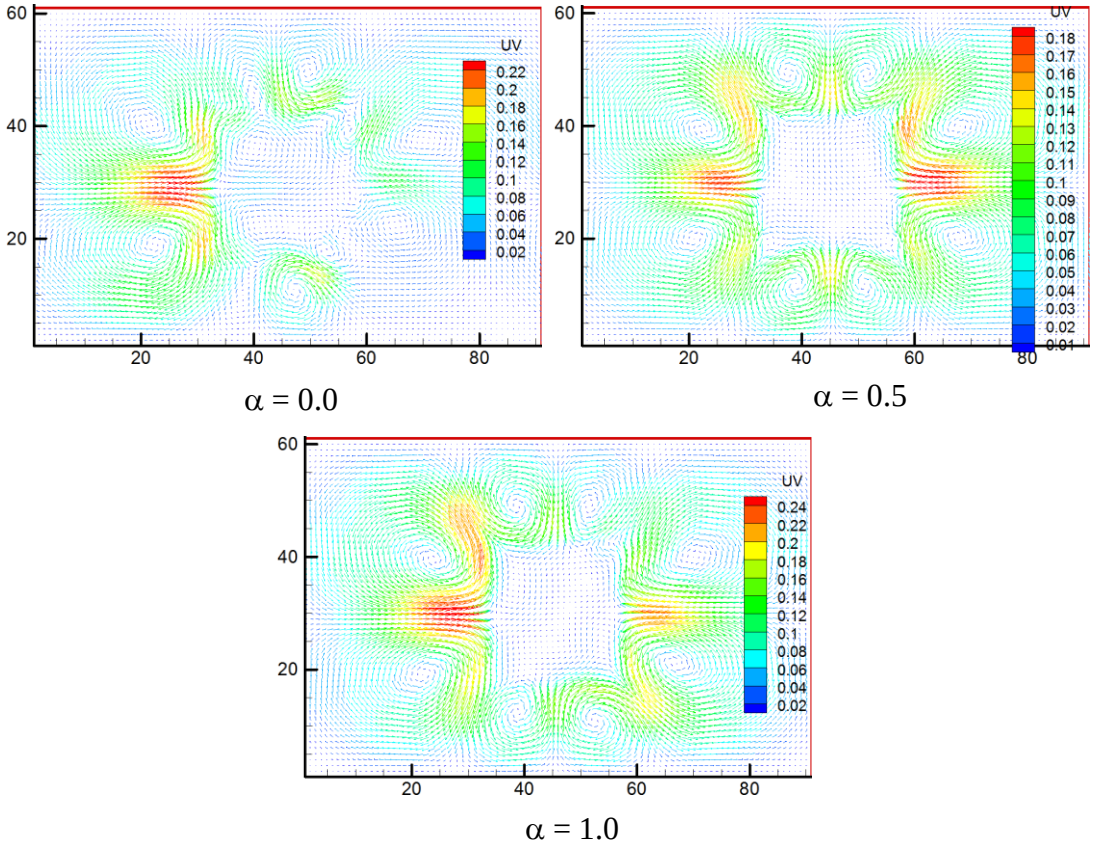

Fig. 6-2 The spurious velocity calculated with Eq. (6-2).

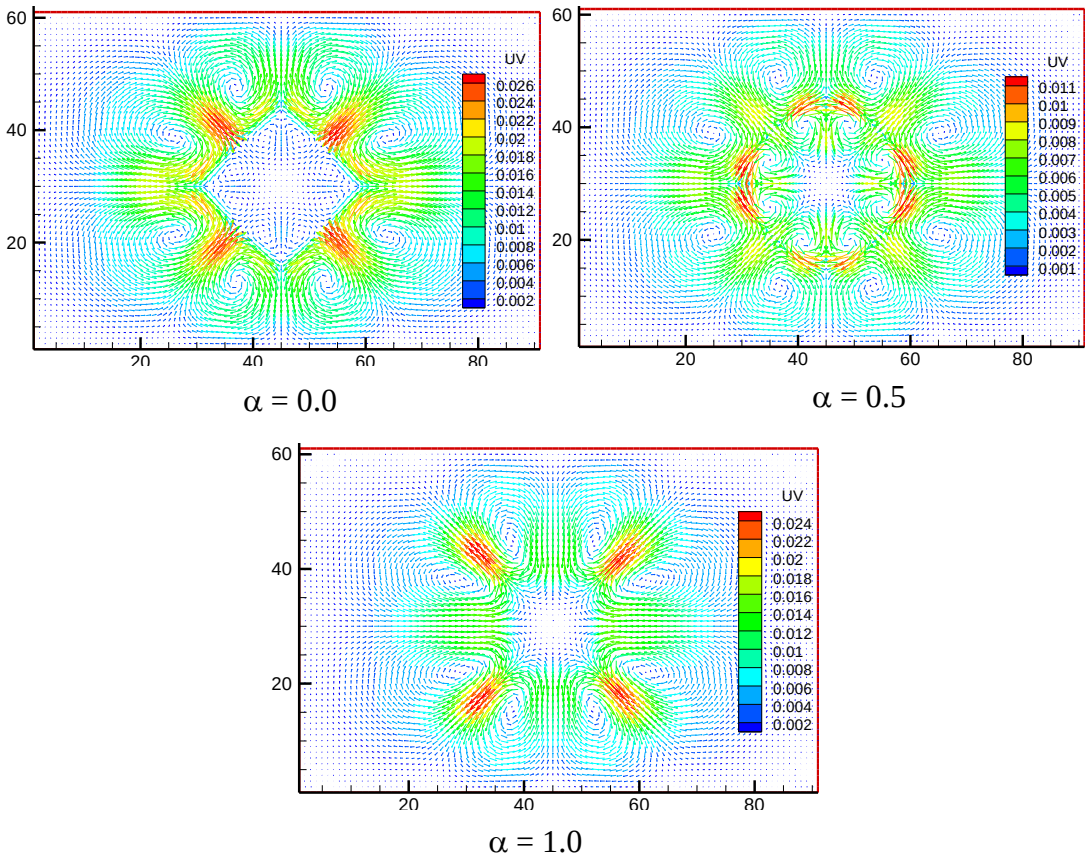

Fig. 6-3 The spurious velocity calculated with Eq. (6-3)

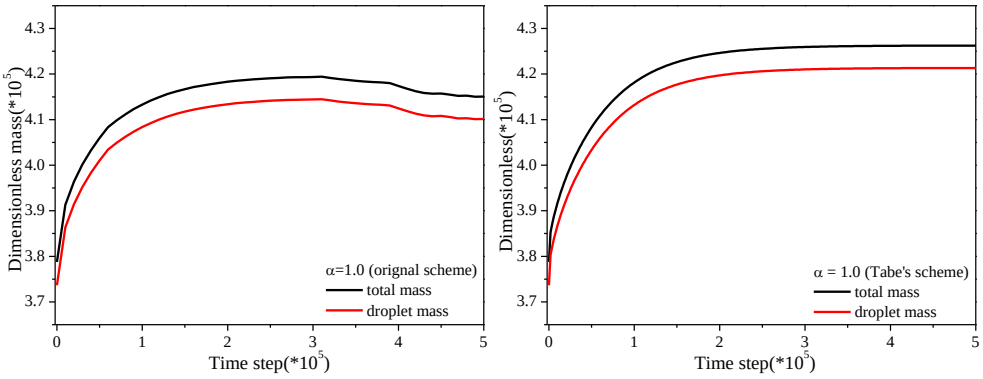

Fig. 6-4 Typical mass evolution histories under the two schemes

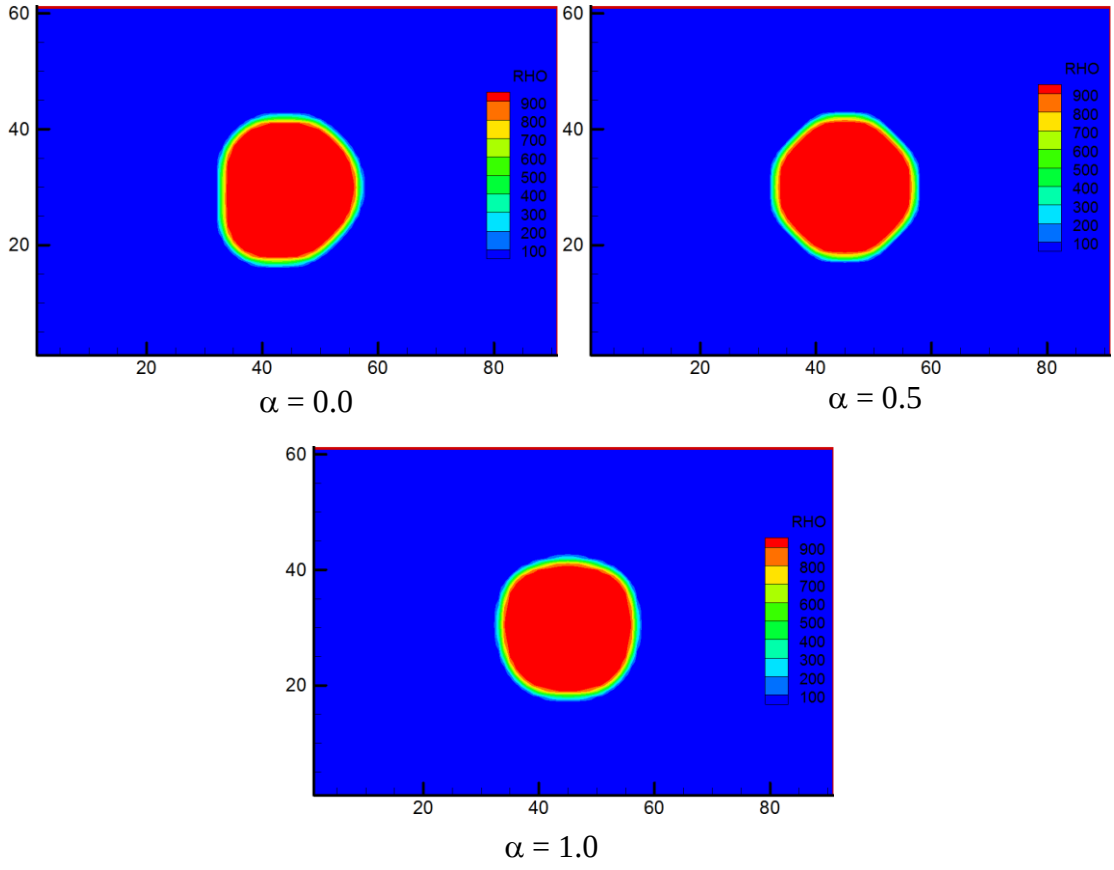

Fig. 6-5 Density distributions with typical blending factor when Eq. (6-2) is used

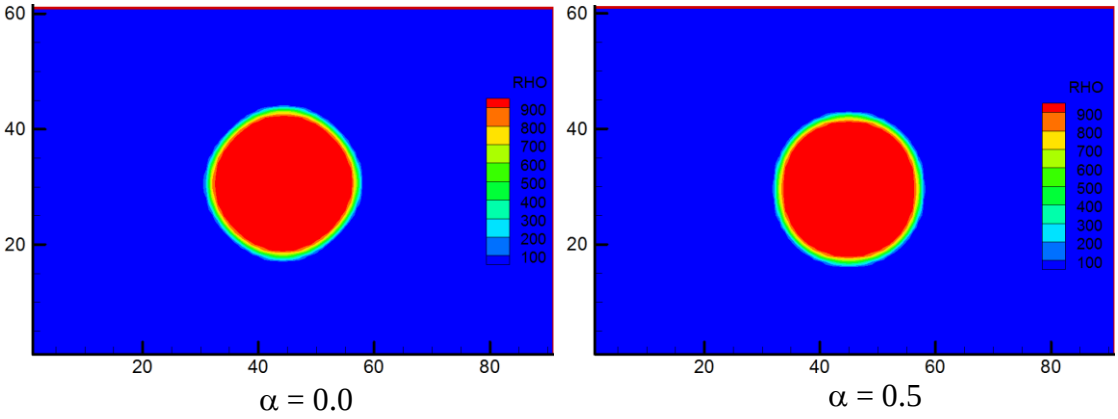

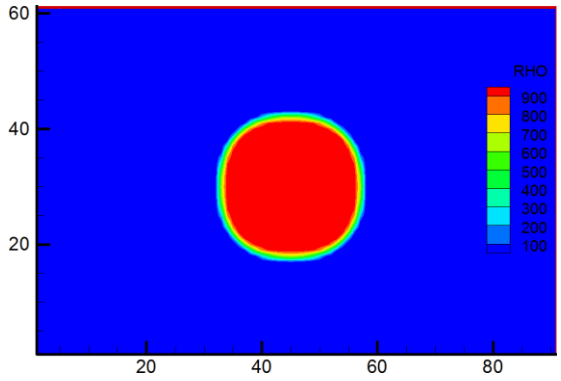

α = 1.0

Fig. 6-6 Density distributions with typical blending factor when Eq. (6-3) is used

6.2 Interface profile difference between the ρ and ϕ

In the present model, the interface capturing is realized by the prediction of the order parameter, ϕ, which describes a two-phase system with a small density ratio. As shown in Eqs. (2-28), (2-30) and (2-32) the distribution of the order parameter ϕ is decided by the interaction of the intermolecular forces and the advection effect. However, the prediction of the velocity in the advection term comes from the g_i equation; as shown in Eqs. (2-29), (2-31), (2-33), (2-41) and (2-42), the profile of the density ρ is used in these equations. And from Fig. 6-1 and Eq. (6-1), we can find that there is some difference between the profiles of the ρ and the ϕ, particularly in the interface region; thus, the predicted velocity based on the density, ρ, profile is believed to deviate from the velocity directly predicted from the ϕ profile. This difference is considered to be a new source of the spurious velocity. To remove this type of error, maintaining the same profile for the ρ and the ϕ in the interface may be a solution.

$$\rho = \begin{cases} \rho_G, & \phi \le \phi_G \\ \dfrac{\phi - \phi_G}{\phi_L - \phi_G}\left(\rho_L - \rho_G\right) + \rho_G, & \phi_G < \phi < \phi_L \\ \rho_L, & \phi \ge \phi_L \end{cases} \qquad 6\text{-}4$$

Yan and Yu (2007), for the purpose of simplifying the equilibrium particle distribution functions of the f_i^{eq} and the g_i^{eq} and thus reducing the required computational resources; used a linear type of cut-off and magnification equation (as shown in Eq. (6-4)) instead of the present sine type. With this improvement, both the derivatives of the ρ and the ϕ calculated with the scheme shown in Eq. (6-2) use the same profile in the interface region and the derivatives in the interface tension force parts of f_i^{eq} and g_i^{eq} can be

calculated simultaneously. We believe that with this method, the spurious velocity coming from profile difference between the density, ρ, and the order parameter, ϕ, in the interface can be removed. Fig. 6-7 illustrates the predicted profiles of the ρ and ϕ when the linear cut-off and magnification equation (6-4) is adopted in the simulation. From this figure, we can see that the two profiles keep the same distribution in the interface region. Fig. 6-8 is the spurious velocity fields with typical blending factor α values when the linear cut-off and magnification equation (6-4) is used in simulations. From these figures, we can find that the magnitude of the spurious velocity is slightly decreased compared with the original model which calculated the derivative of the density, ρ, with Eq. (6-2) based on the sine type of cut-off and magnification equation (6-1) (as the figures shown in Fig. 6-2). With this new approach, the simulation can acquire the stabilized simulation results compared with the original scheme; although, the simulated droplets still deform severely, as shown in Fig. 6-9.

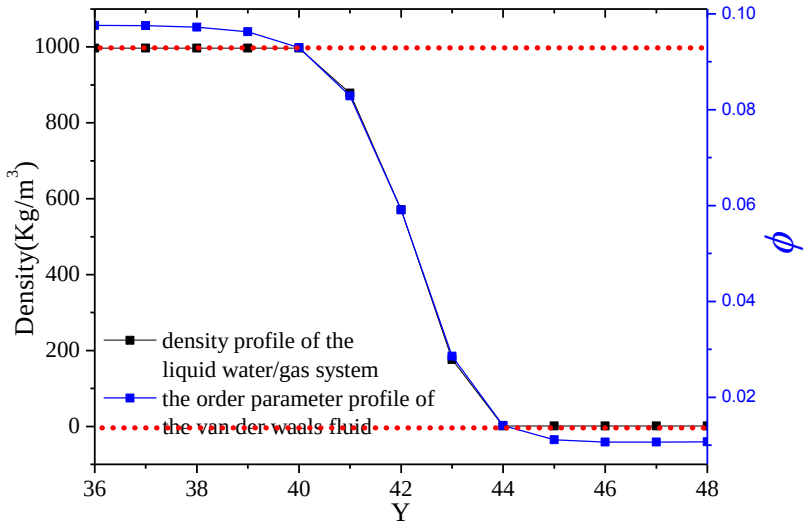

Fig. 6-7 Profiles of ϕ and ρ across the interface predicted from Eq. (6-4)

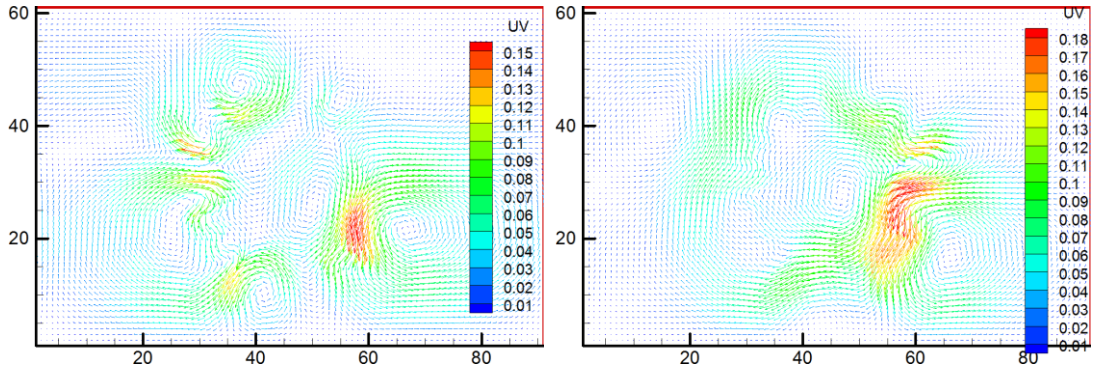

α = 0.0 α = 0.5

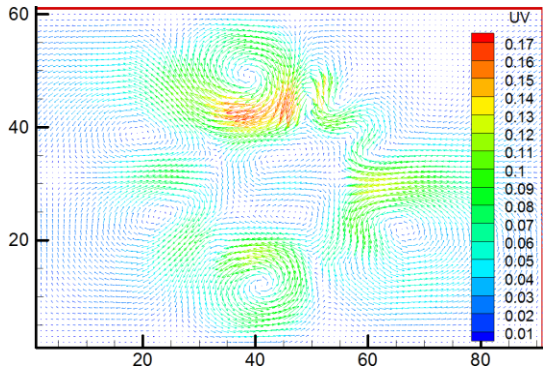

α = 1.0

Fig. 6-8 The spurious velocity calculated from the liner magnification equation

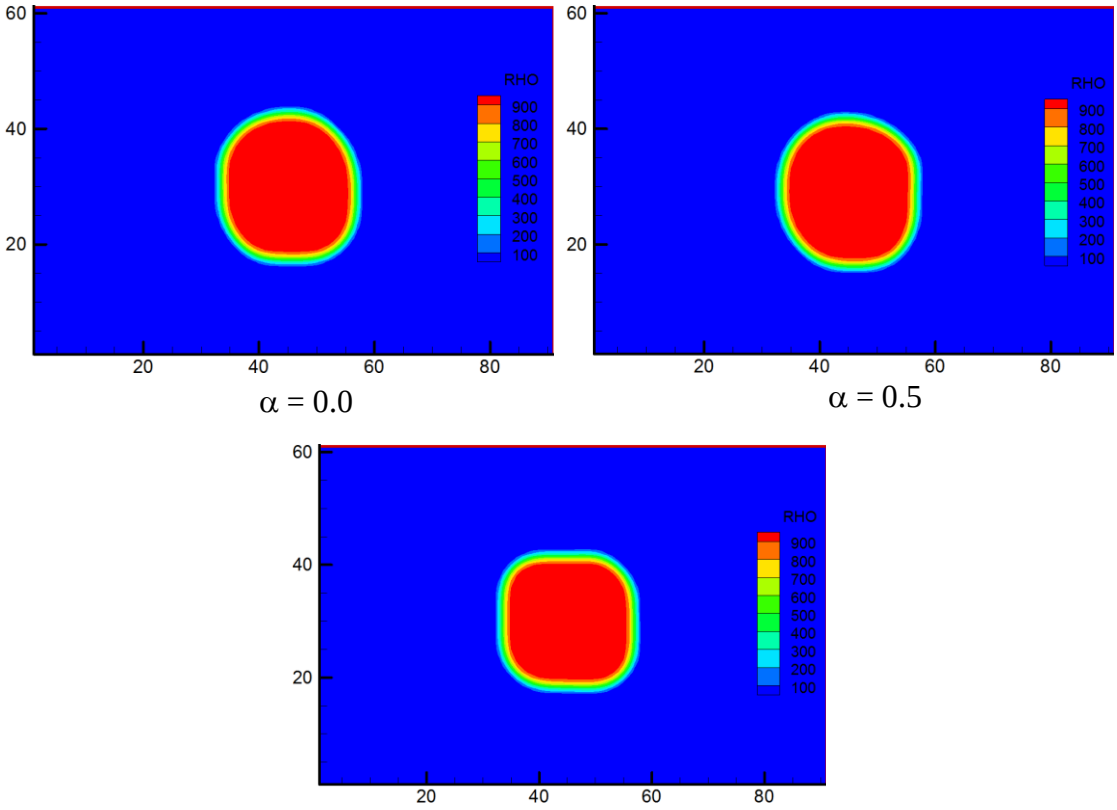

α = 0.0 α = 0.5

α = 1.0

Fig. 6-9 Density distributions with typical blending factor values when the linear magnification equation is used in the simulation

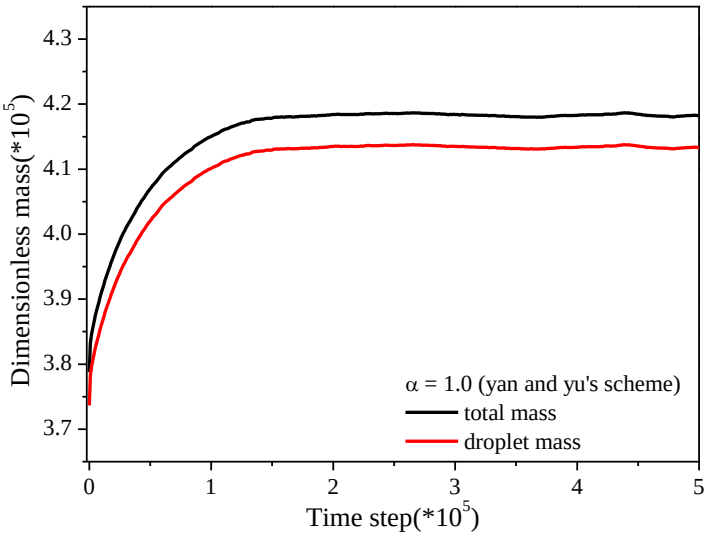

Fig. 6-10 Example of mass evolution history under Yan and Yu's scheme

6.3 Effect of the interface thickness

The thickness of the interface usually determines the magnitude of the spurious velocity coming from the incompatible and anisotropic discretization errors. The thicker the interface, the smaller the truncation errors from the two types of discretization; thus causes a smaller magnitude of the spurious velocity. As discussed in the previous sections, the density, ρ, profile that is used to obtain the velocity field in the present model is decided by the order parameter, ϕ, profile. Thus, as shown in Fig. 6-1 and Fig. 6-7, with the increase of the interface thickness for the ρ profile, the profile difference between the ρ and the ϕ can be further decreased, particularly in the case of the Yan and Yu's scheme.

However, in the simulations with the original scheme or in that of Yan and Yu (2006), there is a large magnitude of spurious velocity, and the simulation time is much larger than in the cases with Tabe's scheme. The simulation times for the three cases when the blending factor α = 0.5 for the first 10000 steps are listed in the following table. To test our idea and shorten the calculation time, we increase the interface thickness following the scheme adopted by Tabe et al. (2009) for the calculation of the density, ρ, derivatives in the intermolecular force terms of the g_i^{eq} equation.

Table 6-1 Computation time

Original scheme	Yan and Yu's scheme	Tabe's scheme
22.0 *24 hours	16.3 *24 hours	0.167*24 hours

Because the profile of the density, ρ, is decided by the order parameter, ϕ, profile through the cut-off and magnification equation (Eq. (6-1)), the interface thickness of ρ can be adjusted by changing the cut-off threshold values, rather than changing the κ value in the traditional LBM models. Three groups of cut-off threshold values are tested here, with the detailed values being: $(\phi_G = 0.012, \phi_L = 0.095)$, $(\phi_G = 0.015, \phi_L = 0.092)$, and $(\phi_G = 0.012, \phi_L = 0.095)$. Fig. 6-11 shows variations of the interface thickness of the ρ profile, when the cut-off threshold values change; with the three groups of threshold values adopted, the thickness of the interface increases along the liquid phase region with one more lattice point, along the gas phase region with one more lattice point and along both regions with two more lattice points. Meanwhile, due to the sine-type cut-off and magnification equation, with the increase of the interface thickness, the profile difference in the interface region becomes larger than before. Fig. 6-12 , Fig. 6-13, and Fig. 6-14 are the typical spurious velocity fields predicted from the three groups of cut-off threshold values with typical blending factor α values. From these figure, we can find that with the increase of the interface thickness, the magnitude of the spurious velocity gradually decreases. Such a small degree of reduction may result from the increase of the profile difference when the truncation errors from the incompatible and anisotropic discretization errors decrease in these cases. Because of the small reduction in the magnitude of the spurious velocity, taking the simulation results from the threshold value being $(\phi_G = 0.012, \phi_L = 0.095)$ as an example which is shown in Fig. 6-15, there is no obvious difference in the predicted shape of the droplet compared with that predicted from Tabe's scheme with the original cut-off threshold values shown in the section 1.

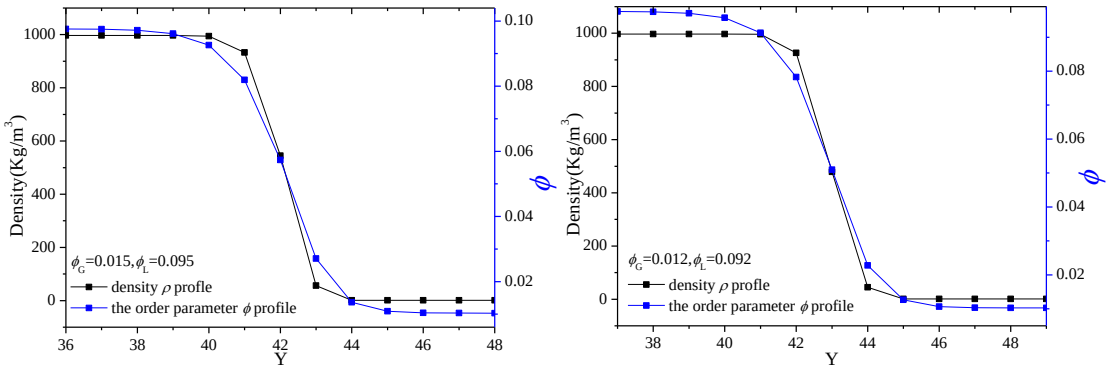

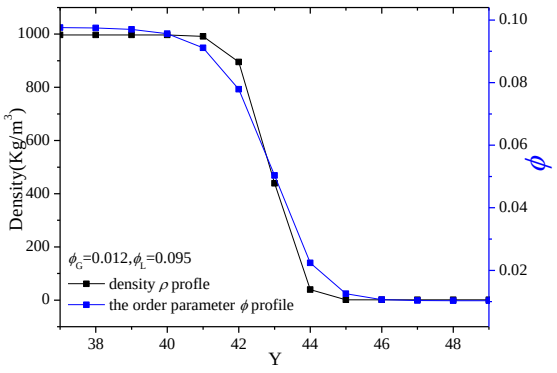

Fig. 6-11 The interface thickness variations when different groups of the threshold values are used

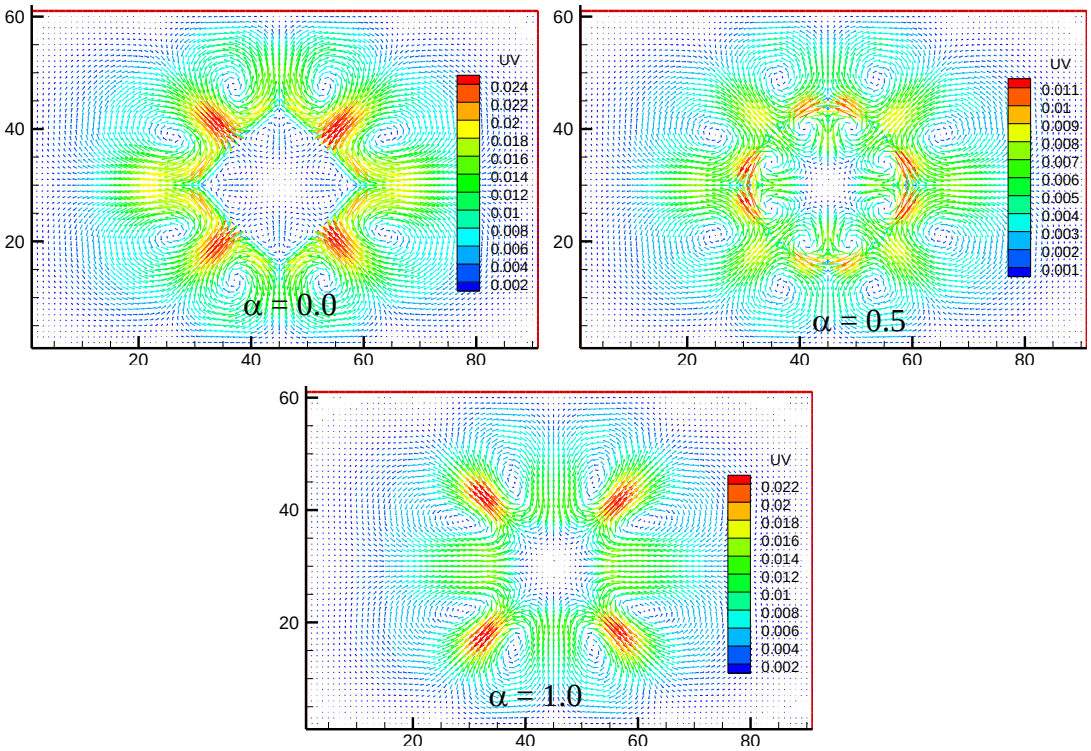

Fig. 6-12 The spurious velocity fields with the threshold values of $(\phi_G = 0.012, \phi_L = 0.095)$

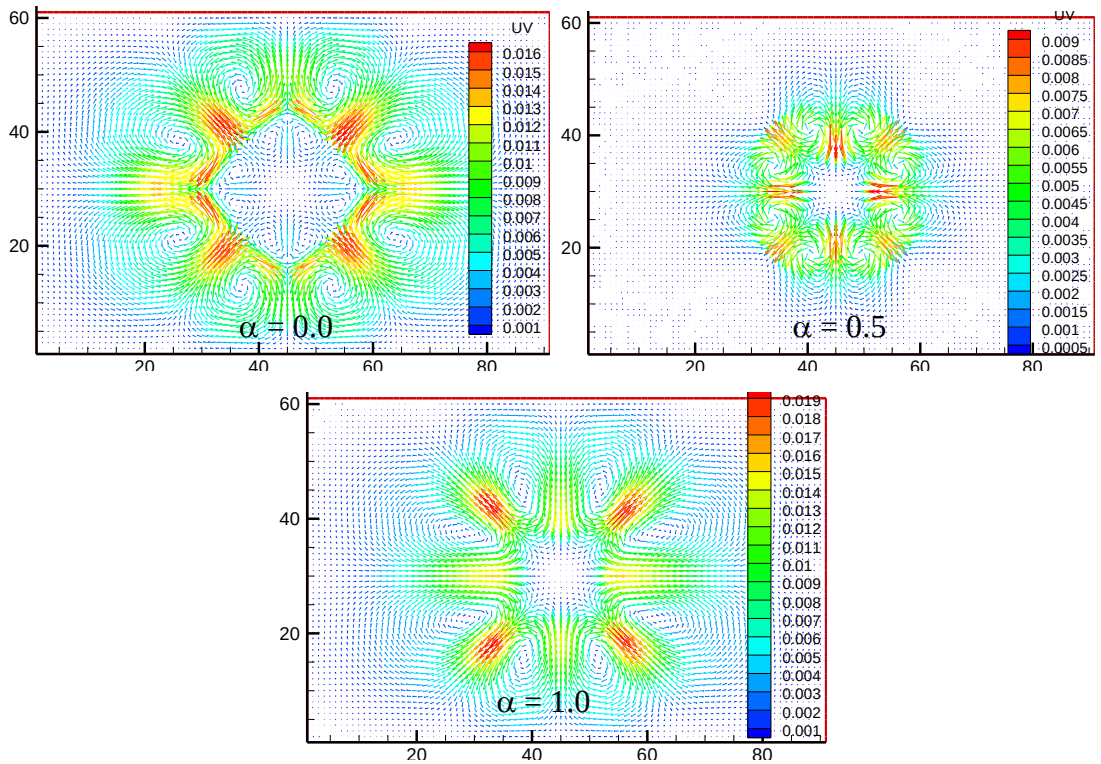

Fig. 6-13 The spurious velocity fields with the threshold values of $(\phi_G = 0.015, \phi_L = 0.092)$

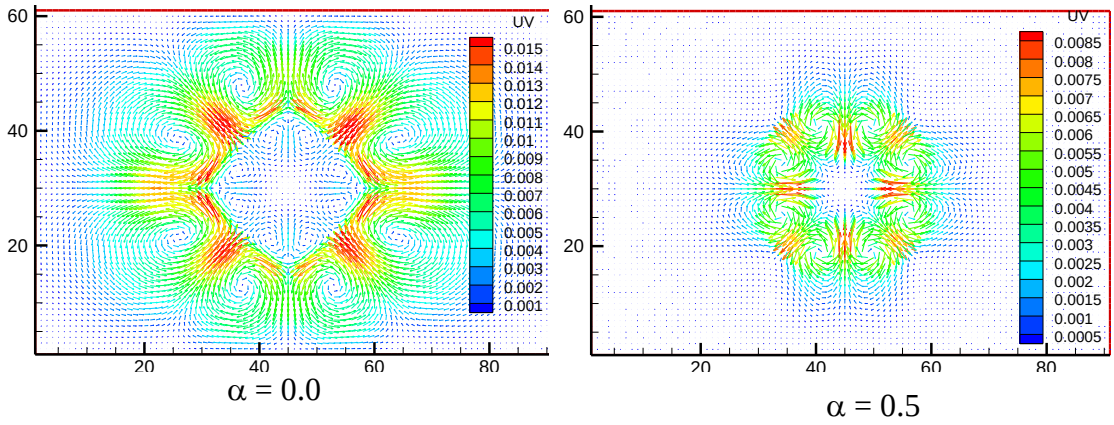

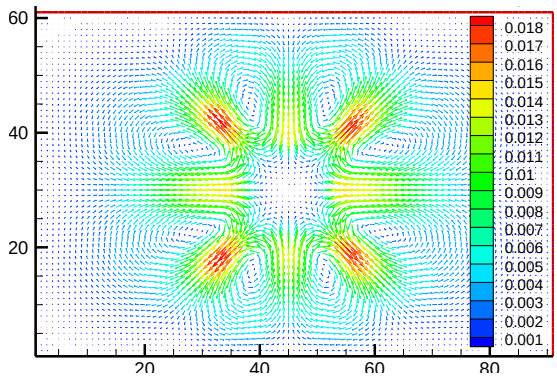

α = 1.0

Fig. 6-14 The spurious velocity fields with the threshold values of $(\phi_G = 0.012, \phi_L = 0.095)$

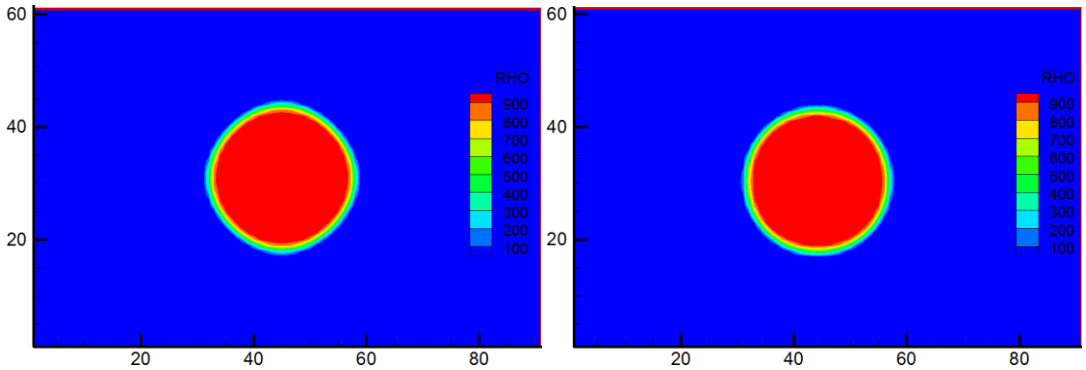

α = 0.0 α = 0.5

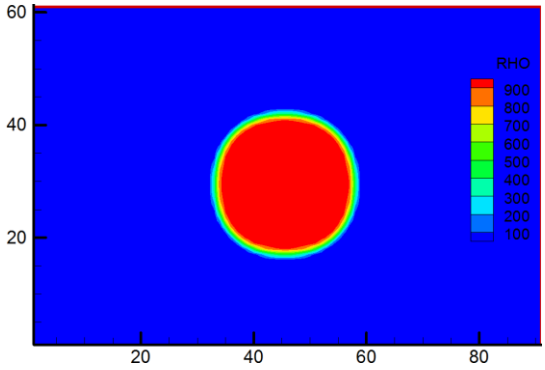

α = 1.0

Fig. 6-15 Density distributions with typical blending factor values when $(\phi_G = 0.012, \phi_L = 0.095)$

6.4 Discussion and conclusions

Through the investigations made in the chapter, we have proved that the profile difference coming from the cut-off and magnification process is another new source of the spurious velocity. The profile

discontinuities around the cut-off threshold values causd the largest magnitude of the spurious velocity, which could be greatly reduced by using the scheme proposed by Tabe et al. (2009) to smooth the density profile. Also, with the linear cut-off and magnification equation proposed by Yan and Yu (2006), we succeeded in reducing the spurious velocity coming from the ρ and ϕ profile difference in the interface region. Moreover, based on the scheme adopted by Tabe et al. (2009), we reduced the magnitude of the spurious velocity by increasing the interface thickness, which is believed to come from the decrease of the truncation errors in the incompatible and anisotropic discretization.

However, as shown in Fig. 6-1, Fig. 6-7 and Fig. 6-11, in all of the treatments we adopted in this chapter, the differences between the ρ and ϕ profiles in the bulk phase regions of the liquid and gas have been paid little attention. Due to the cut-off effect, the ρ profile in the bulk phase regions keeps exactly constant values, so as to satisfy the incompressible condition in the momentum equation recovered by the g_i equation. However, the interface capturing equation recovered by the f_i equation and described by the variable ϕ is slightly compressible even in the bulk phases. The existence of the spurious velocity in the two-phase system described by ϕ will break the force balance in the bulk phases, such that it will eventually affect the force balance in the interface region. So a more sophisticated cut-off and magnification equation combining with a more elaborate derivative scheme is expected to be able to further reduce the spurious velocity arising from the profile difference between the ρ and ϕ profiles. Such that the magnitude of the spurious velocity can be further decreased, the droplet shape deformation tendency with the radius length variation can also be removed.

7 General conclusions and future plan

Although containing some heuristic treatments and being poor in computational efficiency, the free-energy-based one-component-two-phase flow lattice Boltzmann method for large density ratio, which was proposed by Inamuro et al. (2004), is still a good choice for simulating two-phase flow phenomena with large density ratio. This because it can be easy implemented and can be used to simulate two-phase flows with arbitrary density ratios less than 1000:1. In order to improve its performance and make the simulated results reliable, numerical analysis of the effects of the heuristic treatments in both the model itself and the boundary conditions, and the implementation of the successive over-relaxation method to solve the Poisson equation are deeply required. Concentrating on these motivations and objectives, together with the strange phenomena mentioned in the Chapter 1, we solved the shape deformation and volume variation problems met in simulations of a static water droplet in the gas phase and supplied reasonable explanations to the desired questions based on the numerical investigations in subsequent chapters of this dissertation.

7.1 Summary of the concluding remarks

The main achievements and conclusions in each chapter are organized as the follows:

In chapter 1, we emphasized the importance of two-phase simulation, particularly, of two-phase flows with large density ratios; then compared the advantages and disadvantages of the typical numerical techniques, such as the microscopic molecular dynamics, the mesoscopic LBM models, and the macroscopic continuum methods. The mesoscopic methods are believed to be a better choice, as the interface dynamics occur on the mesoscopic scale. Among the LBM models, the free-energy-based model is preferred, due to its thermodynamic consistency. Among the existing three free-energy-based LBM models, the one developed by Inamuro et al. (2004) is believed to be not difficult to use; however, the effects from the heuristic treatments and existence of some undesired numerical phenomena have not yet been investigated. So we determined the research targets of this dissertation to be finding the origins of the shape and volume variation problems and making improvements.

In chapter 2, starting from the basic LBM model for ideal gas, we introduced the transformations of the intermolecular interaction forces formula for the non-ideal gas and showed how these intermolecular terms were combined with the basic LBM model to establish the free-energy-based two-phase flow LBM model for large density ratio. In this process, the thermodynamic meaning of the pressure calculated in the Poisson-equation-based fractional step method was found to be the hydrodynamic pressure. Then, we introduced the successive over-relaxation method (SOR)-based formula that was adopted by Tabe et al.

(2009) for the purpose of solving the Poisson-equation-based fractional step method with easier implementation and faster calculation speed, together with its corresponding staggered grids. Thus, the blending factor α between the staggered grids was introduced into this model. Following the parameters, initial conditions and the boundary conditions adopted in Tabe et al. (2009), we concluded that the shape deformation and volume variation problems that occurred in the simulation were independent of the grid resolution. Thus, in the subsequent chapters, to keep the same physical problem, droplets with the same physical size were used for the investigations.

In chapter 3, we introduced the detailed numerical treatments of the typical boundary conditions adopted in the simulation; special concentration was made for the differences between the 0-velocity inlet and free-out outlet boundary conditions and the periodic boundary condition. From the simulation results from both the two sets of boundary conditions, it was found that the volume expansion and shape oscillation of the droplet in the steady stage came from the implementation of the 0-velocity inlet and free-out outlet boundary condition, and these numerical phenomena can be removed by using the periodic boundary condition. The numerical simulation results also proved that both the velocity inlet and the free-out outlet boundary conditions could be sources of mass non-conservation; the order parameter exchange with the outside at the outlet by the advection effect made the outlet a source of mass non-conservation. The constant initial value (which was different from the equilibrium value) set at the inlet is another larger source of mass non-conservation encountered when implementing velocity inlet and free-out outlet boundary conditions. The mass non-conservation at the velocity inlet essentially arose from the fact that the initial order parameter values in the two phases with the existence of the curved interface could not be analytically obtained.

In chapter 4, with the periodic boundary condition, we traced the shape deformation and volume variation process in the unsteady stage and proved that volume variation of the droplet in the simulation was determined by the interactions of the diffusion effect of the pressure gradient force and the curvature effect of the interfacial tension force, and volume variation can be greatly reduced by using the equilibrium values in the two phases as the initial values. In this way the diffusion process could be greatly reduced so as to minimize the volume variation. Also, shape deformation was proved to be mainly caused by the advection effect of the spurious velocity field and the advection effect was balanced by the curvature effect of the interface tension force. The numerical error coming from the interactions of the diffusion effect and the curvature effect was also a reason for shape deformation, thought the droplet deformation arising from this effect was smaller than the one from the advection effect. Besides, droplet deformation tendency with the change of radius was also coming from the advection effect. More importantly, the numerical simulation result proved that it is possible for a LBM model that removes the

advection term to predict the equilibrium or the static problem with better accuracy, due to the removal the numerical errors arising from the calculation of the advection term.

In chapter 5, we first introduced the common origins of the spurious velocity shared by the free-energy-based LBM models, and then proved that the spurious velocity from the calculation of the Poisson-equation-based fractional step method was a new source. This new source belongs to the category of the anisotropic discretization error and has not been reported before. The spurious velocity from this source could be reduced by averagely blending the velocity components from the two types of staggered grids (which make use of the velocity components in the orthogonal and diagonal directions) when the simulated droplet wass free from the radius length effect. For the simulated droplet with different radii, a reasonable explanation that combines the interactions of the interface tension force and the pressure gradient force in the first sub-stage of the rapid shape deformation stage was established. Such an explanation could well answer the question as to why the magnitude of the spurious velocity changed with blending factor α values and the radius length, in addition to the question of why large shape deformation corresponded to small spurious velocity but small shape deformation corresponded to large magnitude of spurious velocity. Finally, the appropriate blending factor α values for each radius length were summarized to predict the droplet with smallest deformation.

In chapter 6, we proved that the heuristic treatment, known as the cut-off magnification equation, used to realize large density ratios, was also a new source of the spurious velocity that was unique in the present model. Discontinuities in the profile around the cut-off threshold values causd the largest magnitude of the spurious velocity, which could be greatly reduced by using the scheme proposed by Tabe et al. (2009) in which the derivative of the order parameter ϕ is used to smooth the density profile. Also, with the linear cut-off magnification equation proposed by Yan and Yu (2006), we succeeded in reducing the spurious velocity coming from the difference between the ρ and ϕ profile in the interface region. Moreover, based on the scheme adopted by Tabe et al. (2009), we reduced the magnitude of the spurious velocity by increasing the interface thickness, which is believed to come from the decrease of the truncation errors in the incompatible and anisotropic discretization.

7.2 Directions for future research

As discussed in Chapters 5 and 6, in the present model and schemes, with all the treatments we have adept, the profile differences between the ρ and the ϕ in the bulk phase regions of the liquid and gas have been given little attention. Due to the cut-off effect, the ρ profile in the bulk phase regions remains constant, so as to satisfy the incompressible condition in the momentum equation recovered by the g_i

equation. However, the interface-capturing equation recovered by the f_i equation and described by the variable ϕ is slightly compressible even in the bulk phases. The existence of the spurious velocity in the two-phase system described by ϕ will break the force balance in the bulk phases; such that it will eventually affect the force balance in the interface region. A more sophisticated cut-off and magnification equation combining with a more elaborate derivative scheme is expected to be able to further remove the spurious velocity arising from the profile difference between the profiles of the density ρ and the order parameter ϕ; so that the magnitude of the spurious velocity can be further decreased; moreover, the droplet shape deformation tendency with the radius length variation can be removed.

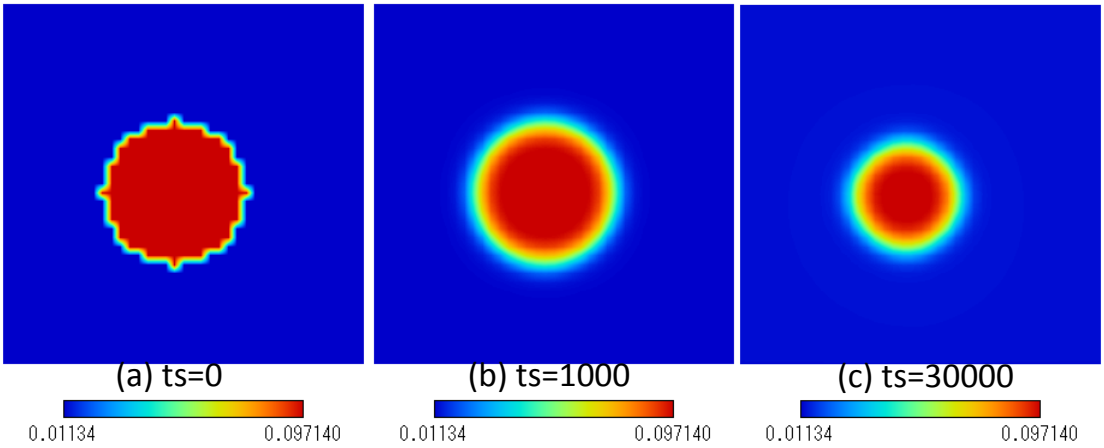

Fig. 7-1 Cross sections of computation domain along the middle of Z axis

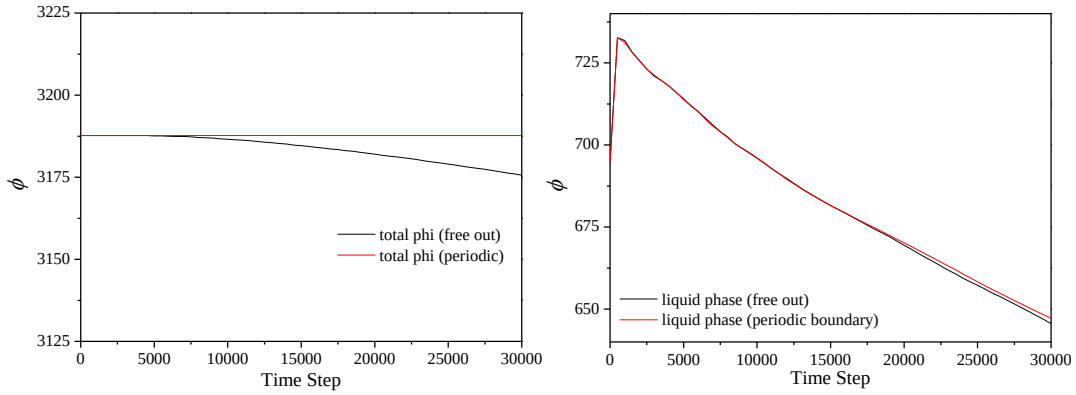

Fig. 7-2 The evolution histories of ϕ in the two types of boundary conditions

The 3D simulation shows the unphysical phenomena similar to those observed in this dissertation, but to an even greater degree. The mass conservation problem occurs even when the periodic boundary condition is used in the simulation, as shown in Fig. Fig. 7-1and Fig. 7-2; the droplet shape variations

with changes in the radius length and the blending factors are also observed, as illustrated in Fig. 7-3 and Fig. 7-4. The 3D simulation is believed to be more physically realistic and is able to take the spatial problems into consideration. Solving these problems and developing a free-energy-based two-phase flow LBM for large density ratio that is reliable for 3D simulation would be a significant contribution to the society of the academic and engineering.

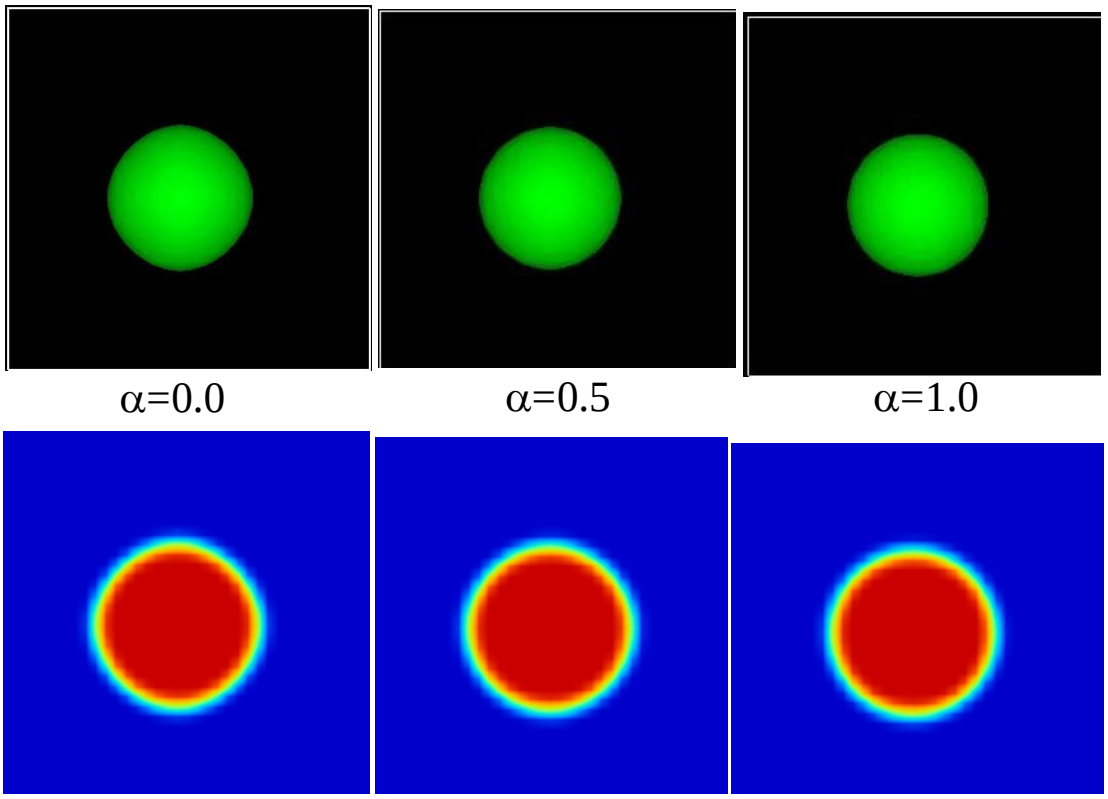

Fig. 7-3 Typical droplet shape when the initial radius is 8 *dx*

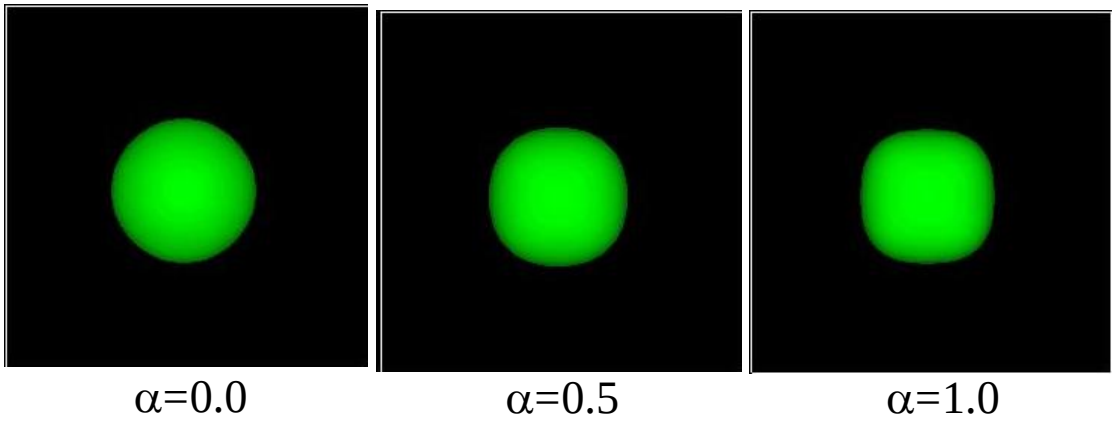

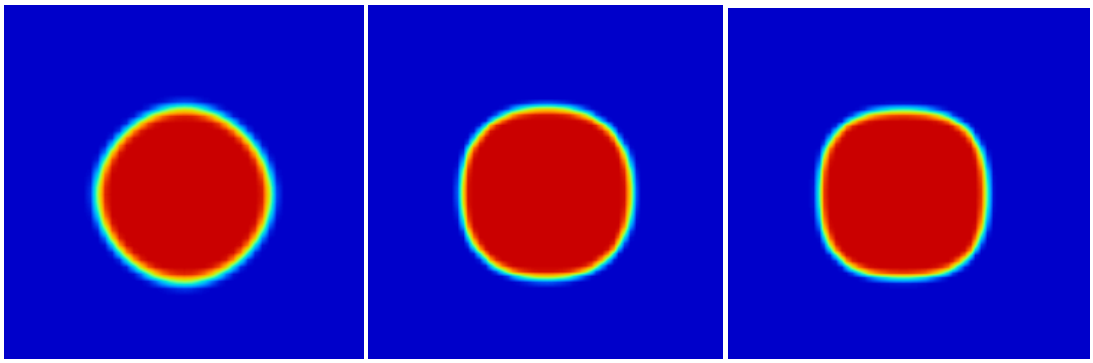

Fig. 7-4 Typical droplet shape when the initial radius is 16 *dx*

8 Reference

Chiappoini, D., Bella, G., Succi, S., Toschi, F. and Ubertini, S., Improved lattice Boltzmann without parasitic currents for Rayleigh-Taylor instability, Vol.7, No.3 (2010), pp.423–444.

Connington, K. and Lee, T., A review of spurious currents in the lattice Boltzmann method for multiphase flows, Journal of Mechanical Science and Technology, Vol.26, No.12 (2012), pp.3857–3863.

Fakhari, A. and Rahimian, M.H., Phase-field modeling by the method of lattice Boltzmann equations, Physical Review E, 81 (2010) 036707.

Gunstensen, A.K., Rothman, D.H., Zaleski, S., Zanetti, G., Lattice Boltzmann model of immiscible fluids, Physical Review A, Vol.43, No.8 (1991),pp. 4320–4327.

Gong, J., Oshima, N., Kurihara, E. and Tabe, Y., Decision of the best blend proportional factor value of two staggered grids used in LBM for PEFC simulation, Proceeding of the 9th International Conference on Nanochannels, Microchannels, and Minichannels, ASME (2011), pp.239–248.

Gong, J., Oshima, N. and Tabe, Y., The appropriate blend proportional factor value of two staggered grids used in the free energy based LBM With large density ratio, Proceeding of the 11th International Conference on Nanochannels, Microchannels, and Minichannels, ASME (2013), pp. V001T012A006.

Guo, Z.L., Zheng, C.G. and Shi, B.C., Force imbalance in lattice Boltzmann equation for two-phase flows, Physical Review E, Vol.83, No.3 (2011), pp.1–8 (036707).

Grunau, D., Chen, S., Eggert, K., A lattice Boltzmann model for multiphase fluid flows, Physics of. Fluids A, Vol.5, No.10 (1993), pp. 2557–2562.

Han, B., Yu, J. and Meng, H., Lattice Boltzmann simulations of liquid droplets development and interaction in a gas channel of a proton exchange membrane fuel cell, Journal of Power Sources, Vol. 202, No. 1 (2012), pp. 175–183.

Hao, L. and Cheng, P., Lattice Boltzmann simulations of liquid droplet dynamic behavior on a hydrophobic surface of a gas flow channel, Journal of Power Sources, Vol. 190, No. 2 (2009), pp. 435–446.

Hao, L. and Cheng, P., Lattice Boltzmann simulations of water transport in gas diffusion layer of a polymer electrolyte membrane fuel cell, Journal of Power Sources, Vol. 195, No. 12 (2010), pp. 3870–3881.

Hao, L. and Cheng, P., Capillary pressures in carbon paper gas diffusion layers having hydrophilic and hydrophobic pores, International Journal of Heat and Mass Transfer, Vol. 55, No. 1–3 (2012), pp. 133–139.

He, X., Chen, S. and Zhang, R., A lattice Boltzmann scheme for incompressible multiphase flow and its application in simulation of Rayleigh-Taylor instability, Journal of Computational Physics, Vol.152, No.2 (1999), pp.642–663.

Huang, H., Wang, L. and Lu, X., Evaluation of three lattice Boltzmann models for multiphase flows in porous media, Computers and Mathematics with Applications, Vol.61, No.12 (2011), pp.3606–3617.

Inamuro, T., Konishi, N. and Ogino, F., A Galilean invariant model of the lattice Boltzmann method for multiphase fluid flows using free-energy approach, Computer Physics Communications, Vol.129, No.1–3 (2000), pp.32–45.

Inamuro, T., Ogata, T., Tajima, S. and Konishi, N., A lattice Boltzmann method for incompressible two-phase flows with large density differences, Journal of Computational Physics, Vol.198, No.2 (2004), pp.628–644.

Jacmin, D., An energy approach to the continumm surface tension method, in: the 34th Aerospace Science Meeting and Exhibit, AIAA, Reno,Nevada, 1996, pp. 96-0858.

Jacqmin, D., Calculation of two-phase Navier–Stokes flows using phase-field modeling, Journal of Computational Physics, Vol.155, No. 1 (1999), pp.96-127.

Jamet, D., Torres, D., and Brackbill, J.U., On the Theory and Computation of Surface Tension: The Elimination of Parasitic Currents through Energy Conservation in the Second-Gradient Method, Journal of Computational Physics, Vol 182, No.1 (2002), pp. 262-276.

Kibo, K., Numerical simulation of liquid water behavior in PEM fuel cell using lattice Boltzmann method, master thesis, Hokkaido University, sapporo, 2007.

Lee, T., Effects of incompressibility on the elimination of parasitic currents in the lattice Boltzmann equation method for binary fluids, Computers & Mathematics with Application, Vol.58, No.5 (2009), pp.987-994.

Lee, T. and Fischer, P. F., Eliminating parasitic currents in the lattice Boltzmann equation method for nonideal gases, Physical Review E, Vol.74, No.4 (2006), pp.1–7 (046709).

Lee, T. and Lin, C., A stable discretization of the lattice Boltzmann equation for simulation of incompressible two-phase flows at high density ratio, Journal of Computational Physics, Vol.206, No.1 (2005), pp.16–47.

Lee, T. and Liu, L., Lattice Boltzmann simulations of micron-scale drop impact on dry surfaces, Journal of Computational Physics, Vol.229, No.20 (2010), pp.8045–8063.

Lee, Y., Numerical simulation of two-phase flow in PEM fuel cell using lattice Boltzmann method, master thesis, Hokkaido University, sapporo, 2009.

Moriyama, K. and Inamuro, T., Lattice Boltzmann simulations of water transport from the gas diffusion layer to the gas channel in PEFC, Communications in Computational Physics, Vol.9, (2011), pp.1206–1218.

Pooley, C. M. and Furtado, K., Eliminating spurious velocities in the free energy lattice Boltzmann method, Physical Review E, Vol.77, No.4 (2008), pp.1–9 (046702).

Pruppacher, H.R. and Klett, J.D., Microphysics of clouds and precipitation, 2nd edn. (2004), pp. 393-409, Springer.

Rothman, D.H.and Keller, J.M., Immiscible cellular-automaton fluids, Journal of Statistical Physics, Vol.52, Issue (3–4) (1988), pp.1119–1127.

Rowlinson, J.S. and Widom, B., Molecular Theory of Capillary, Oxford Press, Oxford, 1989.

Ryu, S. and Ko, S., A comparative study of lattice Boltzmann and volume of fluid method for two-dimensional multiphase flows, Nuclear Engineering and Technology, Vol.44, No.6 (2011), pp.623–638.

Salah, Y.B., Tabe, Y. and Chikahisa, T., Two phase flow simulation in a channel of a polymer electrolyte membrane fuel cell using the lattice Boltzmann method, Journal of Power Sources, Vol.199, No.0 (2012), pp.85–93.

Sasaki, T., Numerical simulation of liquid water behavior in gas diffusion layer in PEFC using lattice Boltzmann method, master thesis, Hokkaido University, sapporo, 2011.

Scarbolo, L., Molin, D., Perlekar, P., Sbragalia, M., Soldati, A. and Toschi, F., Unified framework for a side-by-side comparison of different multi-component algorithms: Lattice Boltzmann vs. phase field model, Journal of Computational Physics, Vol.234 (2012), pp.263–279.

Seta, T. and Okui, K., Effects of truncation error of derivative approximation for two-phase lattice Boltzmann method, Journal of Fluid Science and Technology, Vol.2, No.1 (2007), pp.139–151.

Seta, T., Takahashi, R., Numerical simulation of two-phase flows using phase-field interface-tracking method, Proceedings of the 14th Computational Engineering Conference, Sapporo, 2001, pp. 541–542 (No. 01-10).

Shan, X., Analysis and reduction of the spurious current in a class of multiphase lattice Boltzmann models, Physical Review E 73(4) (2006) 047701.

Shan, X. and Chen, H., Lattice Boltzmann model for simulating flows with multiple phases and components, Physical Review E, Vol.47, No.3 (1993), pp.1815–1819.

Sukop, M.C., Thorne, D.T. Jr., Lattice Boltzmann Modeling: An Introduction for Geoscientists and Engineers, Springer Berlin Heidelberg, Berlin, Heidelberg, 2006.

Succi, S., The Lattice Boltzmann Equation for Fluid Dynamics and Beyond (2001), pp.155–176, 179–213, Oxford University Press.

Swift, M.R., Osborn, W.R. and Yeomans, J.M., Lattice Boltzmann simulation of nonideal fluids, Physical Review Letters, Vol.75, No.5 (1995), pp.830–833.

Swift, M.R., Orlandini, E., Osborn, W.R., Yeomans, J.M., Lattice Boltzmann simulations of liquid-gas and binary fluid systems, Physical Review E 54(5) (1996) 5041-5052.

Tabe, Y., Lee, Y., Chikahisa, T. and Kozakai, M., Numerical simulation of liquid water and gas flow in a channel and a simplified gas diffusion layer model of polymer electrolyte membrane fuel cells using the lattice Boltzmann method, Journal of Power Sources, Vol.193, No.1 (2009), pp.24–31.

Wagner, A. J., The origin of spurious velocities in lattice Boltzmann, International Journal of Modern Physics B, Vol.17, No.1–2 (2003), pp.193–196.

Yan, Y. and Zu, Y., A lattice Boltzmann method for incompressible two-phase flows on partial wetting surface with large density ratio, Journal of Computational Physics, Vol.227, No.1 (2007), pp.763–775.

Yang, A.J., Fleming, P.D. and Gibbs, J.H., Molecular theory of surface tension, The Journal of Chemical Physics, Vol.64, No.9 (1976), pp.3732–3747.

Yu, Z., Fan, L.-S., Multirelaxation-time interaction-potential-based lattice Boltzmann model for two-phase flow, Physical Review E 82(4) (2010) 046708.

Yuan, P., Schaefer, L., Equations of state in a lattice Boltzmann model, Physics of Fluids, Vol. 18, No. 4(2006) 04201.

Zheng, H.W., Shu, C. and Chew, Y.T., A lattice Boltzmann model for multiphase flows with large density ratio, Journal of Computational Physics, Vol.218, No.1 (2006), pp.353–371.